AFRL-IF-RS-TR-2006-9
Final Technical Report
January 2006

DEVELOPMENT AND EXPERIMENTAL VERIFICATION OF SURFACE EFFECTS IN A FLUIDIC MODEL

Clemson University

APPROVED FOR PUBLIC RELEASE; DISTRIBUTION UNLIMITED.

The views and conclusions contained in this document are those of the authors and should not be interpreted as necessarily representing the official policies, either expressed or implied, of the Defense Advanced Research Projects Agency or the U.S. Government.

AIR FORCE RESEARCH LABORATORY
INFORMATION DIRECTORATE
ROME RESEARCH SITE
ROME, NEW YORK

STINFO FINAL REPORT

This report has been reviewed by the Air Force Research Laboratory, Information Directorate, Public Affairs Office (IFOIPA) and is releasable to the National Technical Information Service (NTIS). At NTIS it will be releasable to the general public, including foreign nations.

AFRL-IF-RS-TR-2006-9 has been reviewed and is approved for publication

APPROVED: /s/

CLARE THIEM
Project Engineer

FOR THE DIRECTOR: /s/

JAMES A. COLLINS, Deputy Chief
Advanced Computing Division
Information Directorate

REPORT DOCUMENTATION PAGE

Form Approved
OMB No. 074-0188

Public reporting burden for this collection of information is estimated to average 1 hour per response, including the time for reviewing instructions, searching existing data sources, gathering and maintaining the data needed, and completing and reviewing this collection of information. Send comments regarding this burden estimate or any other aspect of this collection of information, including suggestions for reducing this burden to Washington Headquarters Services, Directorate for Information Operations and Reports, 1215 Jefferson Davis Highway, Suite 1204, Arlington, VA 22202-4302, and to the Office of Management and Budget, Paperwork Reduction Project (0704-0188), Washington, DC 20503

1. AGENCY USE ONLY (Leave blank)	2. REPORT DATE JANUARY 2006	3. REPORT TYPE AND DATES COVERED Final Jun 2001 – Jun 2004

4. TITLE AND SUBTITLE
DEVELOPMENT AND EXPERIMENTAL VERIFICATION OF SURFACE EFFECTS IN A FLUIDICS MODEL

5. FUNDING NUMBERS
C   - F30602-01-2-0541
PE - E1
PR - 17
TA - 00
WU - 70

6. AUTHOR(S)

Professor James Hickman and Dr Shankar Sundaram

7. PERFORMING ORGANIZATION NAME(S) AND ADDRESS(ES)

Prime	Sub
Clemson University	CFD Research Corporation
Department of Nanoengineering	215 Wynn Drive
300 Brackett Hall, Box 34502	Huntsville Alabama 35805
Clemson South Carolina 29634-5702	

8. PERFORMING ORGANIZATION REPORT NUMBER

N/A

9. SPONSORING / MONITORING AGENCY NAME(S) AND ADDRESS(ES)

Defense Advanced Research Projects Agency	AFRL/IFTC
3701 North Fairfax Drive	525 Brooks Road
Arlington Virginia 22203-1714	Rome New York 13441-4505

10. SPONSORING / MONITORING AGENCY REPORT NUMBER

AFRL-IF-RS-TR-2006-9

11. SUPPLEMENTARY NOTES

AFRL Project Engineer: Clare Thiem/IFTC/(315) 330-4893/ Clare.Thiem @rl.af.mil

12a. DISTRIBUTION / AVAILABILITY STATEMENT
APPROVED FOR PUBLIC RELEASE; DISTRIBUTION UNLIMITED.

12b. DISTRIBUTION CODE

13. ABSTRACT *(Maximum 200 Words)*
Sensor and diagnostic systems based on microfluidic devices have already achieved very low total detection limits which are projected to approach the single molecule level. Under such conditions adverse wall/sample interactions, such as adsorption, could significantly or completely deplete the analyte stream of the material of interest, at total coverage much smaller than a monolayer. Careful understanding of the interaction of flow surface availability and adsorption is required. The research team on this effort carried out experimental determination and verification of flow effects on wall/biomaterial interactions. Results were incorporated into an existing software suite to generate an advanced model of adsorption under flow conditions. The knowledge gained from this effort represents a step forward in providing the proper tools and techniques to successfully simulate microfluidic device and system concepts prior to prototyping.

14. SUBJECT TERMS
Electro-osmotic Flow, Protein Adsorption, Microfluidic Systems, Computational Fluidics

15. NUMBER OF PAGES
135

16. PRICE CODE

17. SECURITY CLASSIFICATION OF REPORT	18. SECURITY CLASSIFICATION OF THIS PAGE	19. SECURITY CLASSIFICATION OF ABSTRACT	20. LIMITATION OF ABSTRACT
UNCLASSIFIED	UNCLASSIFIED	UNCLASSIFIED	UL

TABLE OF CONTENTS

TABLE OF FIGURES

LIST OF TABLES

LIST OF SYMBOLS

$g(e)$ Energy distribution probability function of surface binding sites

e Energy level of a specific binding site

e_μ Mean energy level of the surface binding sites

e_σ^2 Variance of energy level of the surface binding sites

$f(\tau)$ Interaction time distribution probability function

τ Interaction time of one specific successful binding attempt

τ_μ Mean interaction time of the binding attempts over the surface

τ_σ^2 Interaction time variance of the binding attempts over the surface

E_i See e .

A_μ Coefficient for the exponential dependence of τ_μ on E_i

A_σ Coefficient for the exponential dependence of τ_σ n E_i

R The gas constant, R=8.316 J/mol·K

T Temperature

$V_{z,\max}$ Maximum axial flow rate of the microfluidics system

V_z General axial flow rate of the microfluidics system

$\overline{V_z}$ Average axial flow rate of the microfluidics system

p_0 Hydrodynamic pressure at the inlet of the microfluidics system

p_L Hydrodynamic pressure at the outlet of the microfluidics system

μ Viscosity of the material

L Length of the microfluidics system

φ	Dimension of protein molecule
r	Radius position of protein molecule
Φ	Diameter of the microfluidics system
τ	Proximity time – the time a protein spends near a binding site
τ_c	Characteristic proximity time
β	Scaling factor
Q	Flowrate
$\boldsymbol{Q}$	Bounded function of Q
K_a or k_a	Rate of adsorption
K_d or k_d	Rate of desorption
P_{max}	Limiting surface coverage
μ_{eof}	Electro-osmotic mobility
$f(E_i)$	Fraction of binding sites with energy E_i, constrained by $\Sigma_I f(E_i) = 1$
$P(E_i)$	Probability of protein binding to a site of energy E_i
$R(\tau,t)$	Residence time distribution function
$P(\tau)$	Probability of protein binding as a function of proximity time
f_m	Total surface concentration of protein
γ	The coverage ratio of adsorbed protein
ζ	Zeta potential
K_a^{ABM}	The intrinsic static rate of adsorption
K_d^{ABM}	The intrinsic static rate of desorption
$C_{complex}(t)$	Concentration of protein on the wall.
$C_{Protein}^{Near\ Wall}(t)$	Concentration of protein very close to the wall.

$C_{sites}(t)$ Concentration of binding sites on the wall

$f(\tau,t)$ Distribution of proximity times in the vicinity of a binding site.

$f(E,t)$ Distribution of available binding sites of energy E.

$P_d(E,\gamma')$ Probability of protein debinding from an occupied site of energy E.

γ' The local hydrodynamic shear factor

$P_a(\tau,E)$ Probability of a protein with proximity time τ binding to an open

            site of energy E.

θ Fractional site coverage

Summary

Protein adsorption under flow and static conditions

Protein adsorption behaviour under flow conditions, with 1% monolayer coverage resolution, was probed with alkaline phophatase, glucose oxidase and horseradish peroxidase. We found that the rate of adsorption increased substantially as the flowrate increased, often by >3 orders of magnitude, but that the limiting surface coverage was reduced. Thus, fewer sites were involved in the adsorption process as the flowrate was increased, but these sites were those best suited to adsorbing the protein, giving the higher rate of adsorption. Consequently, adsorption parameters obtained under static conditions cannot necessarily be extrapolated to cover protein adsorption under flow, and interactions measured under flow conditions have to be considered as being a function of the flow-field itself.

Surface modification

A wide variety of surface modification strategies were developed and used to prepare surfaces with different protein interaction properties. These included modification using self-assembled monolayer derivitization of silicon microchannels, atmospheric pressure Direct Current (DC) plasmas and laser ablation under a controlled atmosphere. Surface analysis techniques showed that different chemical functionalities could be introduced into the surface, and in the case of laser ablation this occurred during the formation of the microchannel itself. The effect of protein adsorption on electro-osmotic flow in microchannels was assessed using dynamic current monitoring.

It was also shown that changes in electro-osmotic flow with protein adsorption could be observed as the adsorption process was occurring. This allowed us to show that there was a substantial difference in the adsorption behaviour of bovine serum albumin to silica, depending on whether it was at physiological pH (pH 7.4) or the isoelectric point of Bovine Serum Albumin (BSA) (pH 5). The rate of adsorption was greater at pH 5, and it was found that while protein adsorption at pH 7.4 was mostly reversible, at pH 5 it was not, and remained irreversible even if the buffer pH was returned to pH 7.4. It was also shown that the changes in Electro-osmotic Flow (EOF) with protein adsorption could not be readily explained in terms of charge shielding. Studies with a range of ionic strength buffers strongly suggested that it is the physical presence of adsorbed protein with interferes with the flow, a consequence of the mechanism of EOF.

Computational fluidics and protein adsorption

The results from the protein adsorption studies showed that protein/surface interaction parameters, such as the rate of adsorption and limiting surface coverage, were strong functions of flowrate. It was also shown that this was most likely due to a range of adsorption sites being present on the surface, with different affinities for protein binding. An advanced binding model (ABM) of protein adsorption which could be incorporated into a computational fluidics framework based on finite element analysis was developed to address this, allowing the simulated surface to include a range of adsorption sites with different protein affinities, and also allowed the rate of adsorption to be a function of flowrate.

Introduction

Sensor and diagnostic systems based on microfluidic devices have already achieved very low total detection limits, and projections indicate even smaller quantities of detectable material, approaching the single molecule level [Kovacs]. Under such conditions adverse wall/sample interactions, such as adsorption, could significantly or completely deplete the analyte stream of the material of interest, at total coverages much smaller than a monolayer. This is shown in Figure 1, where the intersection of detection limits and sensor area are shown in terms of the amount of surface required to deplete the sample.
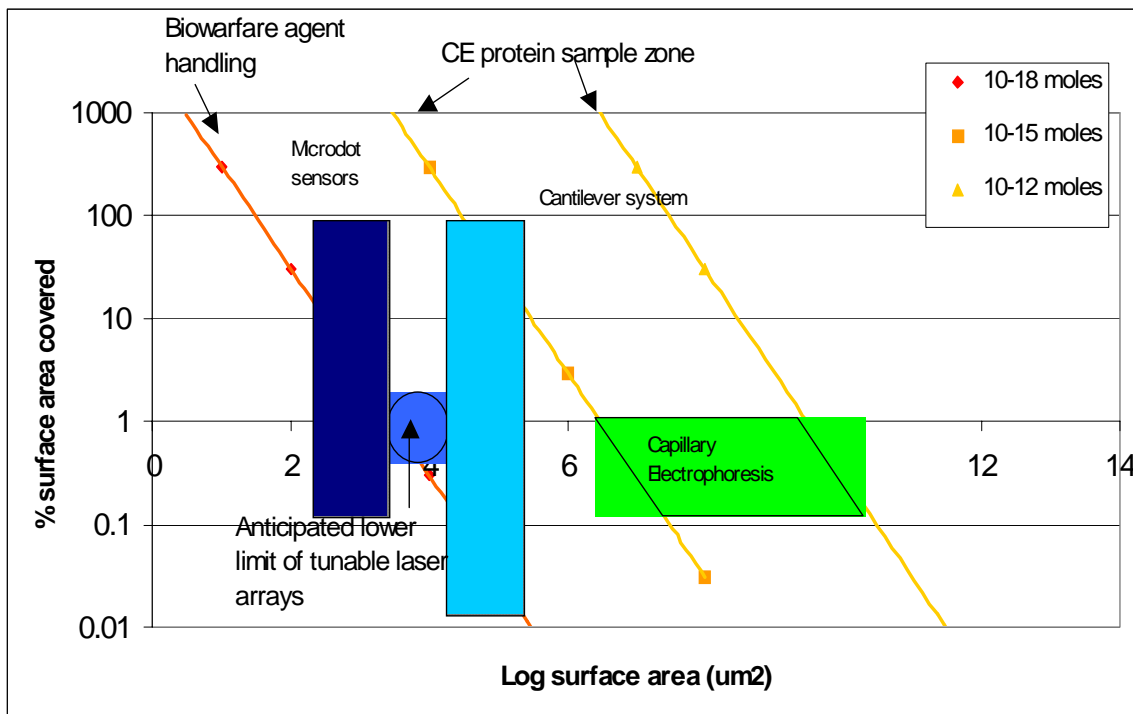
Figure 1: Detection limits, surface area and depletion.

There is a further complication caused by lack of information the effect of flow at such small scales has on the interaction between a molecule in solution and a static receptor site on a surface. The receptor site could be an antibody, or some other recognition agent

and form part of the sensing system, or it could be a non-specific adsorption site which contributes to sample attenuation. In either case, it would be important to understand, for proper simulation of the device's performance characteristics, exactly what role flowrate would play in the behaviour of standard interaction parameters including the rates of adsorption, rates of desorption and the limiting surface coverage.

It is also the case that design and development of microfluidic devices would greatly benefit if the behaviour of that device, when handling fluids, could be successfully simulated in software, prior to prototyping. Such a software product could form part of a larger design package, eventually enabling the rapid optimization of microfluidic device layout automatically, as is seen in the contemporary design of computer chips and printed circuit boards; a large part of the decisions made on layout of components are derived from software driven optimizations, based on the initial design decisions.

We therefore proposed and carried out:

1) the experimental determination and verification of flow effects on wall/biomaterial interactions, and

2) the incorporation of these results into an existing, baseline, software suite (CFD-ACE+) to generate an advanced model of adsorption under flow conditions.

About CFD-ACE+

Traditionally, two different methods have been used to extract kinetics from adsorption data. The simplest approach involves neglecting non-ideal (convective-diffusive) effects

by assuming well-mixed protein in contact with an idealized surface. Coupled with pseudo-second order kinetics, this leads to the classical analytical expression for the Langmuir adsorption isotherm [Gregg et al.], which is regression-fitted to experimental data to calculate the kinetic constants. However, this can lead to large errors in situations where transport is the rate-limiting step. In an incrementally better approach (favored by many today), the convective-diffusive transport of the protein to the surface under fully developed laminar flow conditions, coupled with surface adsorption are described using a lumped-parameter (so-called two compartment) model (Figure 2a). While this is better than the well-mixed approach, this still introduces several drawbacks. The most significant of these are: (a) introduction of an additional fitting parameter k_m (transport coefficient) which can introduce errors in the extracted values (b) non-applicability to flow situations other than fully developed (idealized situations). In summary, neither method yields the true or intrinsic kinetics but rather a value that is influenced partly by the conditions of the experiment.

In contrast, the approach we have chosen is to use Computational Fluid Dynamics (CFD) to analyze the protein/surface interactions. CFD provides a convenient methodology for simultaneously characterizing and studying convective-diffusive transport and adsorption kinetics within a single framework. The model explicitly considers fluidic (convective-diffusive) transport of protein to the surface coupled with a model of protein adsorption on a substrate (Figure 2b). It considers a monolayer formed by a reversible adsorption process, which yields a Langmuir type adsorption isotherm. The salient features of this approach are:

5

a) capable of *ab-initio* accounting for convection, diffusion and electromigration of multiple protein species towards a biomaterial surface in any arbitrary three-dimensional volume;

b) accounts for finite-rate binding kinetics, with the reversible adsorption process modeled as a second-order reaction and the desorption process modeled as a first-order reaction;

c) allows for simulation of localized variations in surface composition through variations in the density of binding sites and/or variations in the binding rate constants at different locations along the surface.

Figure 2: The two compartment model (a) and the convective/diffusive transport and adsorption model (b).

METHODS, ASSUMPTIONS, AND PROCEDURES

Proteins are large biomolecules, regarded as highly surface active, and readily adhering to improperly prepared and protected surfaces [Butler et al. 1997; Norde et al. 1998; Norde et al. 1999]. A study of protein adsorption under flow conditions was therefore

concluded to be an effective means of determining what effect flow might have on the interactions between large biomolecules and microfluidic systems.

We investigated protein adsorption under pressure driven and electro-osmotic flow conditions, both of which are in use in existing and proposed microfluidic systems. A variety of surfaces and surface modification strategies were also investigated, including commercially available capillaries, silane modified silicon and glass surfaces, plasma modified surfaces and microfluidic channels prepared by laser ablation under a controlled atmosphere. Several different protein detection and quantitation methods were also applied, including enzyme assay, the micro bicinchoninic acid assay (μ-BCA assay), X-ray photoelectron spectroscopy (XPS), silver staining and Sodium Dodecyl (lauryl) Sulfate-Polyacrylamide Gel Electrophoresis (SDS-PAGE) followed by staining and densitometry.

NSF Grant ECS-0003227

Many of the *methods* described within this report were developed based on funding received from the National Science Foundation (NSF) Grant number ECS-0003227 "Biocompatible MEMS', and this report is principally concerned with demonstrating the *application* of these methods to solving problems relating to, or providing data on protein surface interactions in model MEMS system.

Choice of proteins

To determine the amount of protein adsorbed in the capillary systems, we initially decided to use a mass balance approach. The introduction of a protein solution with a known concentration, followed by the measurement of the protein concentration exiting

the capillary, would allow us to complete a mass balance and determine the amount of material adsorbed to the capillary wall. We were especially interested in measuring the earliest, sub-monolayer adsorption kinetics, since this region probably involved the most active adsorption sites, and hence those of particular interest to us [Lenghaus et al. 2003]. Thus very high sensitivity assays were required. The literature indicated that total protein assays are relatively insensitive, while enzyme assays rival radioactive isotope labeling as a means of protein detection and quantitation, without the associated hazards [Butler 1981]. In order to maximize the resolution of the adsorption isotherms, down to as small a fraction of monolayer coverage as possible, three enzymatic proteins were chosen for detailed study. Alkaline phosphatase, glucose oxidase and horseradish peroxidase are readily available in high purity, proven in use in Enzyme-linked Immunosorbent Assay (ELISA) protocols or, in the case of glucose oxidase, as a key component in blood sugar sensor systems, and we were able to show could be successfully detected by enzymatic assay at vanishingly low amounts – in the ng/mL range. These proteins were used in the majority of our studies. Acid phosphatase and bovine serum albumin were also employed at various times.

Choice of surfaces

One of our goals was to show that a readily accessible benchtop system could be used to study protein adsorption at very low total protein concentrations (ng/mL), without requiring a large capital outlay. For this reason, our initial studies focused on using commercially available capillary tubing; bare silica, silica coated with poly(acrylamide)

and poly(ethyleneglycol) were obtained from MicrosolvTech. Polyetheretherketone (PEEK) and Teflon were obtained from Zeus industries.

The capillaries were cut to length (150 mm for the fused silica based capillaries, and 100 mm for the Teflon and PEEK capillaries) and glued into a luer lock needle with epoxy. The different lengths were due to the significant back pressure observed with the hydrophobic capillaries creating flow problems at the 150 mm length. The capillaries were equilibrated with flowing buffer (500 µL/hr) for at least 2 hours and preferably overnight prior to use.

Model microfluidic system

A literature survey led to a design which incorporated features commonly encountered in both existing and proposed systems (Figure 3), and it included straight and serpentine channels of varying widths and lengths, as well as chambers with multiple inlets/outlets. The Auto-CAD design file was sent to the MEMS-Exchange, and the testbed was fabricated using deep reactive ion etching (DRIE), required to achieve the large aspect ratio of the channels.
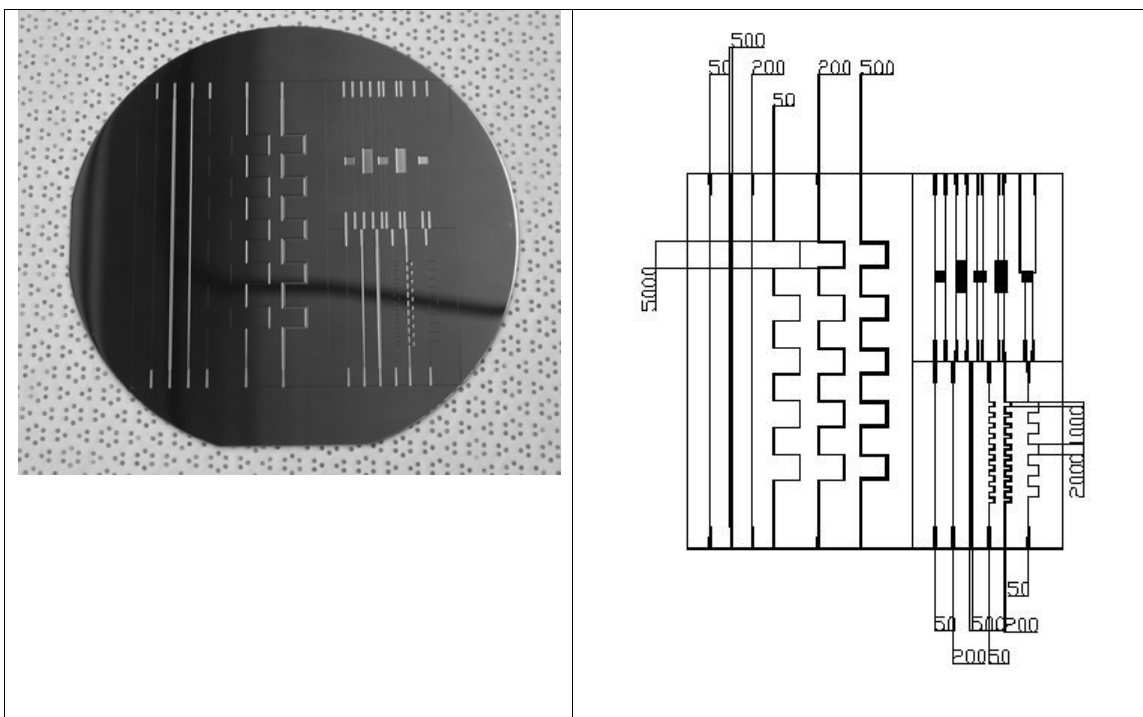
Figure 3: Etched silicon wafer and diagram for model microfluidics system.

Silane modification of surfaces

Controlled surface modification of the testbeds with silanes allowed different types of surfaces to be generated, and tested for protein adsorption. The preparation of a silane self assembled monolayer (SAM) on the silicon wafers, and also on glass coverslips, was carried out in one of two ways.

Method 1: The silicon wafer was immersed in a 50% v/v mixture of conc. HCl (40%)/methanol for 1 hour. The wafer was then rinsed four times with deionized water before being immersed in conc. sulfuric acid (97%) overnight. The wafer was then rinsed

again (4x) with deionized water, and then boiled in water for at least one hour. Following this, the wafers had a contact angle with water of < 5º.

The wafer was then allowed to dry in air. To prepare surfaces from a chlorosilane, a 0.1% solution of the silane (1H, 1H, 2H, 2H tridecafluorotrichlorosilane: 13F) was prepared in distilled toluene in a controlled N_2 atmosphere glovebox. This solution was then removed from the glovebox, and the wafer immersed in the solution for 5 minutes. After this, the wafer was then removed from the silane solution, rinsed 3 times with dry toluene, and then allowed to dry. The contact angle with water following this was typically 110º.

To prepare surfaces from a methoxysilane, a 0.1% silane (diethylpropyltriamine trimethoxysilane: DETA) solution was prepared in toluene and the cleaned surfaces were immersed in it. The solution was then placed on a hot plate, and the silane solution heated to just below its boiling point for 1 hour. The surfaces were then removed, rinsed with toluene and placed in an oven at 80ºC for 1 hour.

Method 2: The wafer was placed in a plasma cleaner, and the plasma chamber evacuated using a scroll pump. High purity oxygen was then introduced with the vacuum pump still running, and a flowing pressure of 100 milliTorr established in the plasma chamber. The plasma generator was then turned on, and the wafer was left exposed to the oxygen plasma for 15 minutes. Following this, the wafer was removed from the plasma chamber and treated with silane solution as per method 1.

Adsorption studies

Alkaline phosphatase (AP), horseradish peroxidase (HRP), and glucose oxidase (GO) were obtained from Pierce. GO and HRP were diluted to the working concentration with phosphate buffered saline (PBS, Fisher). The PBS was purchased from Fisher at 10x concentration and diluted with Milli-Q water as required. Since phosphate is a listed interfering agent for alkaline phosphatase [Coburn et al.1998], AP was diluted with tris(hydroxymethyl)amine hydrochloride (Tris) buffer (50 mM Tris, 138 mM NaCl, 30 mM KCl) prepared with ACS grade or better salts in Milli-Q water. All solutions which contacted AP also contained 50 mM $MgCl_2$ and 0.1 mM $ZnCl_2$ to preserve AP activity [Fernley 1971]. The surface activity of Tris was considered to be insignificant, since there was not a substantial reduction in the surface energy (measured with a KSV goniometer by the pendant drop method) of the Tris solution (69.5 mN/m) compared with water (72.8 mN/m).

The enzyme activity assay was determined using a simple mass balance; the ratio of the eluant activity to the control activity was taken to be proportional to the enzyme remaining in solution. Thus, the change in activity between the inlet and the outlet was proportional to the enzyme lost on passage of the solution through the capillary. Working enzyme solutions were prepared immediately prior to use. The syringe was hooked up to a syringe pump (KDS 100), the capillary/luer lock combination was attached and the syringe pump started at a flow of 100 µL/hr at RT. After being drawn into the syringe (10 mL, polypropylene, Becton-Dickson), a sample of the enzyme solution was pushed through the capillary into a polypropylene centrifuge tube (1.5 mL,

VWR). The enzyme solution was eluted into polypropylene centrifuge tubes (1.5 mL, VWR) containing a 50/50 wt% buffer/glycerine mixture to preserve the eluted enzyme, and appropriate corrections were subsequently made for dilution effects on the apparent enzyme activity. For each experiment, samples were taken every 15 minutes for the first 2 hours, and every hour after that for 3 additional hours. A fresh control was taken from the syringe stock solution each hour and the activity of the eluant was measured and compared with the control. Enzymes were incubated for 30 minutes at 37°C, with alkaline phosphatase being assayed via *para*-nitrophenol phosphate substrate, glucose oxidase being assayed via a coupled reaction with glucose, horseradish peroxidase and *o*-dianisidine, as described by the vendor (Pierce) and horseradish peroxidase was assayed using hydrogen peroxide solution and 3,3′,5,5′ tetramethylbenzidine (TMB) as the indicator, again as described by the vendor.

Surface coverage of the capillary is expressed as monolayer equivalents. Since it is not known exactly in what form the protein adsorbs on the surface, it is necessary to assume a size for calculation of the surface coverage. For alkaline phosphatase, the protein was treated as a sphere with a diameter of 7 nm, based on its specific volume of 0.756 mL/g, and a molecular weight of 140,000 g/mol [Fosset et al.]. Glucose oxidase was treated as a cylinder with dimensions 6 nm x 7 nm x 8 nm and a molecular weight of 160,000 g/mol [Schomburg et al.]. The area occupied by alkaline phosphatase on a surface is then assumed to be ~ 40 nm^2 and for glucose oxidase ~ 56 nm^2, however these dimensions are considered to be approximations only. Horseradish peroxidase is assumed to be 25 nm^2.

The micro bicinchoninic acid (μ-BCA) assay

This assay was carried out as described by the vendor (Pierce), with two modifications. The volume of protein solution and the working BCA solution was reduced to 150 μL each, and the lower detection limit of the assay was reduced from 5 μg/mL to 500 ng/mL by extending the incubation time to 12 hours.

The assay is carried out by first preparing working BCA solution from 25 parts of reagent A (Sodium carbonate, sodium bicarbonate, and sodium tartarate in 0.2 N NaOH), 24 parts of reagent B (4% BCA in water) and 1 part reagent C (4% cupric sulfate pentahydrate in water) and then mixing equal volumes of working solution and protein solution in polypropylene microcentrifuge tubes and incubating at 60ºC for one hour. The solution was then read colourimetrically at 562 nm by placing 200 μL of solution into a well of a 96-well plate and read using a μ-Quant spectrophotometer.

Silver Assay

Specific and non-specific adsorption of proteins to self assembled monolayer (SAM) modified glass surfaces were studied using a kinetic silver staining method. Four surface modified glass (Thomas Scientific, 22mm x 22mm) coverslips were immersed in a staining jar containing 8 ml protein solution, for 2 hours, at room temperature, while under agitation. The coverslips were then removed, rinsed three times with phosphate buffered saline (PBS), once with water and then dried under a stream of nitrogen. Coverslips with adsorbed proteins were then placed into a 6-well plate, containing 3 ml of silver reagent/well. Stain development was monitored in an automated μQuant

microtiter plate reader (from BioTek Instruments Inc). Incubation time was measured from the time the coverslip was added to the well. A standard μ-BCA assay was also performed as a control, with proteins being desorbed from the same surfaces, using a 0.2% sodium dodecyl sulphate (SDS) solution and the amount of protein present in solution determined as described in the previous section.

The kinetic silver staining method for quantification of protein adsorbed to microtiter plates is based on the method described previously [Root et al.]. In our version, the final composition was: silver nitrate 0.5%, ammonium nitrate 0.5%, tungstosilicic acid 0.5% and 0.75% formaldehyde and 12.5% sodium carbonate, pH 10.4. The reaction lag time for stain development was consistently correlated with the amount of protein adsorbed to the surfaces. The kinetics of the reaction were monitored spectrophotometrically at 405 nm. The concentration of the protein solutions was 50 μg/ml in PBS, pH 7.4.

X-Ray Photoelectron Spectroscopy

Analysis of silane modified surfaces were made using a Kratos AXIS165 XPS system equipped with an Al Kα incident photon beam and were operated at a takeoff angle of 90°. Survey scans and high-resolution scans for fluorine (1s), oxygen (1s), nitrogen (1s), carbon (1s) and silicon (2p) were performed for each sample. Based on the high-resolution scans, elemental composition percentages were calculated for each element using the following equations:

$$I_I = \Sigma I_{Ii} \qquad\qquad (1)$$

$$I_I S = I_I / ASF \qquad\qquad (2)$$

$$IS_T = \Sigma I_I S_I \hspace{3cm} (3)$$

$$At_I = (I_I S / \Sigma I_I S_i) * 100\% \hspace{2cm} (4)$$

where I_I is the total area under one high-resolution scan curve and ΣI_{Ii} is the area under an individual curve fitted to the high-resolution scan. ASF is the atomic sensitivity factor, where 1.000, 0.780, 0.477, 0.278 and 0.328 are the factors for fluorine (1s), oxygen (1s), nitrogen (1s), carbon (1s) and silicon (2p) respectively. IS_T is the summation of all of the high-resolution areas divided by their respective ASF and At_I is the elemental composition percentage.

Plasma modification of surfaces

The ability to generate plasmas in microchannels at atmospheric pressure was demonstrated at NIST, where a DC potential of ~2kV readily generated a plasma in a 0.5 mm long microchannel (width 200 μm), while longer distances could be spanned with the application of greater voltages. Different atmospheres during the plasma were shown to confer different surface functionalities, described in the results section.

Dynamic current monitoring of electro-osmotic flow (EOF)

The method has been described in the literature [Locascio et al.]; at NIST a Keithley 2410 was used as the voltage source and current monitor. A variety of microchannels and surface treatments were evaluated using this method; a specific case is described in detail below, but for all the experiments the overall method followed was very similar, with only minor changes to the specific buffer solutions, proteins used or the material used for the reservoirs and capillary channels.

16

Real time measurements of EOF

Lyophilised bovine serum albumin, monobasic sodium phosphate monohydrate and dibasic sodium phosphate were purchased from Sigma-Aldrich and used without further purification. A 0.2 M buffer stock solution (pH 7.4) was prepared by mixing 1.041g of $NaH_2PO_4.H_2O$ with 4.616g of Na_2HPO_4 in 200 mL of water. The stock was then diluted as needed. A 0.2 M buffer at pH 5 was prepared by mixing 2.72g of monobasic and 0.039 g of dibasic in 100 mL of water. Fused silica capillary (i.d. = 50 μm) was purchased from Microsolv and poly ether ether ketone (PEEK) capillary (i.d. = 75 μm) was purchased from Zeus.

Dynamic current monitoring was carried out using a Keithley 2410 as the voltage source and current monitor. The buffer reservoirs were drilled into a piece of polypropylene, and were 20 mm in diameter by 15 mm deep. Buffer concentrations were 10 mM and 8 mM, diluted from stock solution. A lid was prepared for the two reservoirs, and drawn platinum electrodes were inserted into the buffer solutions through it. Bovine serum albumin (12.7 mg/mL) was dissolved in a 10 mM solution of the appropriate buffer, and added as required to the 10 mM reservoir. This operation required that the electrodes be briefly withdrawn from the reservoirs, creating a convenient period of zero current in the data which could be used as a marker for the cycle in which the protein addition occurred.

Two types of EOF measurement were made. For the first, the capillary was first allowed to reach a steady EOF, and then 100 μL of the protein solution was added to the 10 mM

reservoir during the negative (8 mM to 10 mM flow direction) half of the cycle. The

capillary was then allowed to reach a new steady state EOF over subsequent cycles. For

the other (transient) experiment the BSA solution was added to the 10 mM reservoir as

before, but during the next negative cycle the 10 mM buffer solution was withdrawn from

the reservoir and replaced with fresh, protein free, buffer. The system was generally run

with an applied voltage of 1000V, except where otherwise noted in the text.

The electro-osmotic mobility (μ_{eof}) was determined from:

$$\mu_{eof} = L^2/t.V \qquad\qquad \text{Equation 1}$$

where L = length of the capillary, V = the applied voltage and t = is the time measured

for the buffer front to cross the capillary. This was related to the surface charge of the

capillary [Thormann et al.] by:

$$\mu_{eof} = L^2/t.V \qquad\qquad \text{Equation 2}$$

$$\sigma = \mu_{eof}.\kappa.\eta \qquad\qquad \text{Equation 3}$$

where σ = the surface charge, κ is the reciprocal of the Debye length and η is the

viscosity of the solution. The Debye length was estimated using the IUPAC

recommended rationalized four quantity system.

RESULTS AND DISCUSSION

Early results with different capillaries and alkaline phosphatase showed that results were

reproducible, and that coverage down to 0.5% of a monolayer could be successfully

resolved (Figure 4). This gave us confidence that the mass balance method based on enzyme assay could be used to obtain the information we sought [Lenghaus et al. 2003].
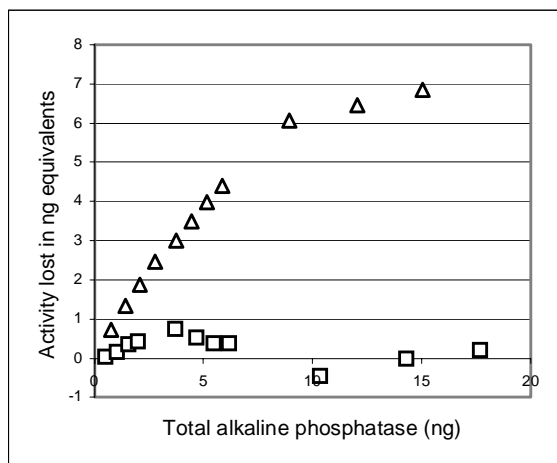
Figure 4:   Loss of alkaline phosphatase activity expressed as equivalent ng of enzyme vs ng of enzyme passed through the PEEK ($\triangle$) and PEG ($\square$) capillaries.

Protein Assay Limits

In addition to the enzyme assays, several other complementary methods (Figure 5) were evaluated for protein detection, especially surface confined proteins. This allowed our results to be cross compared.
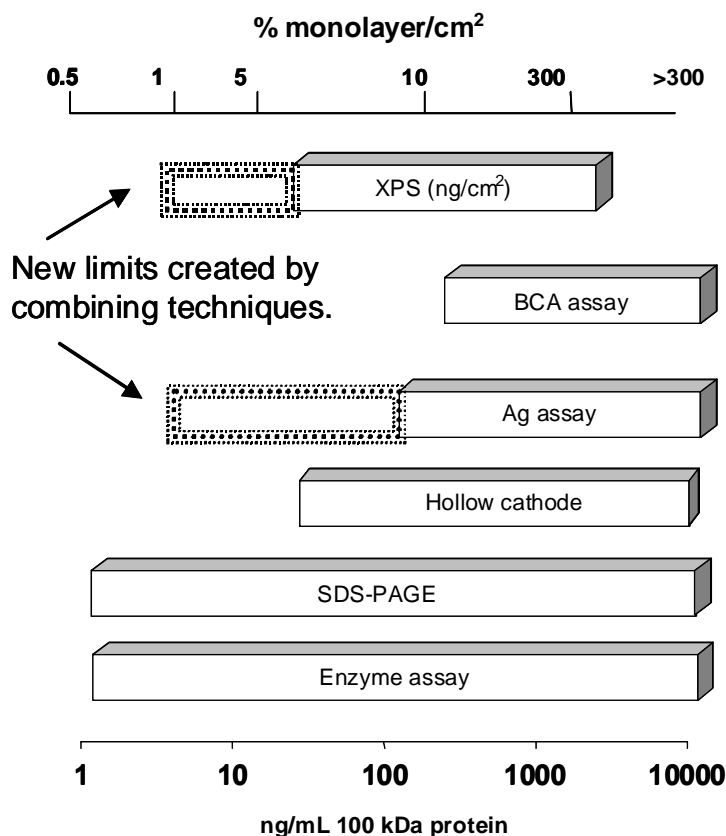
Figure 5: Upper and lower detection limits for several protein detection methods evaluated as part of this project.

Enzyme Assay

The enzyme detection limits depend on the enzyme being considered; the lower end of the range is an estimate based on a readily assayable enzyme such as alkaline phosphatase or horseradish peroxidase. Standard curves with these enzymes show that their presence is resolvable against background at a concentration of 1 ng/mL with a sample volume of 40 μL. The substrate assay for glucose oxidase is roughly an order of magnitude less sensitive.

The upper bound of the enzyme assay is essentially unlimited, as it is possible to serially dilute the enzyme until it reaches a concentration where the assay response is linear. This

is the case with all three chemical detection mechanisms considered (enzyme, Ag assay and BCA assay).

Ag Assay

The most sensitive version of the silver assay which has been demonstrated can produce a detectable response above baseline with 100 µL of a 5 ng/mL solution. Since the silver assay requires that the protein be dried onto the surface, larger volumes of lower concentration can theoretically be addressed by this method as well, giving increased concentration sensitivity.

BCA Assay

The micro-BCA assay from Pierce responds to protein concentrations of approximately 1 µg/mL, with an assay volume of 200 µL. Increased sensitivity is achievable with longer incubation times (24 hours), and a discernible response down to 500 ng/mL has been produced.

XPS

The lower XPS response limit is an approximation. A nitrogen peak can be detected on glass slides at protein concentrations estimated to be an order of magnitude lower than that observable with the BCA assay. The upper limit depends on the thickness of the deposited protein layer, but a 100 fold detectable concentration range seems to be typical of our XPS arrangement.

SDS-PAGE

Sodium dodecyl sulfate – poly(acrylamide) gel electrophoresis (SDS-PAGE) was found to have excellent detection limits, with the added advantage of providing protein

separation as well, allowing the assessment of competitive protein adsorption with protein mixtures.

Model system for microfluidics
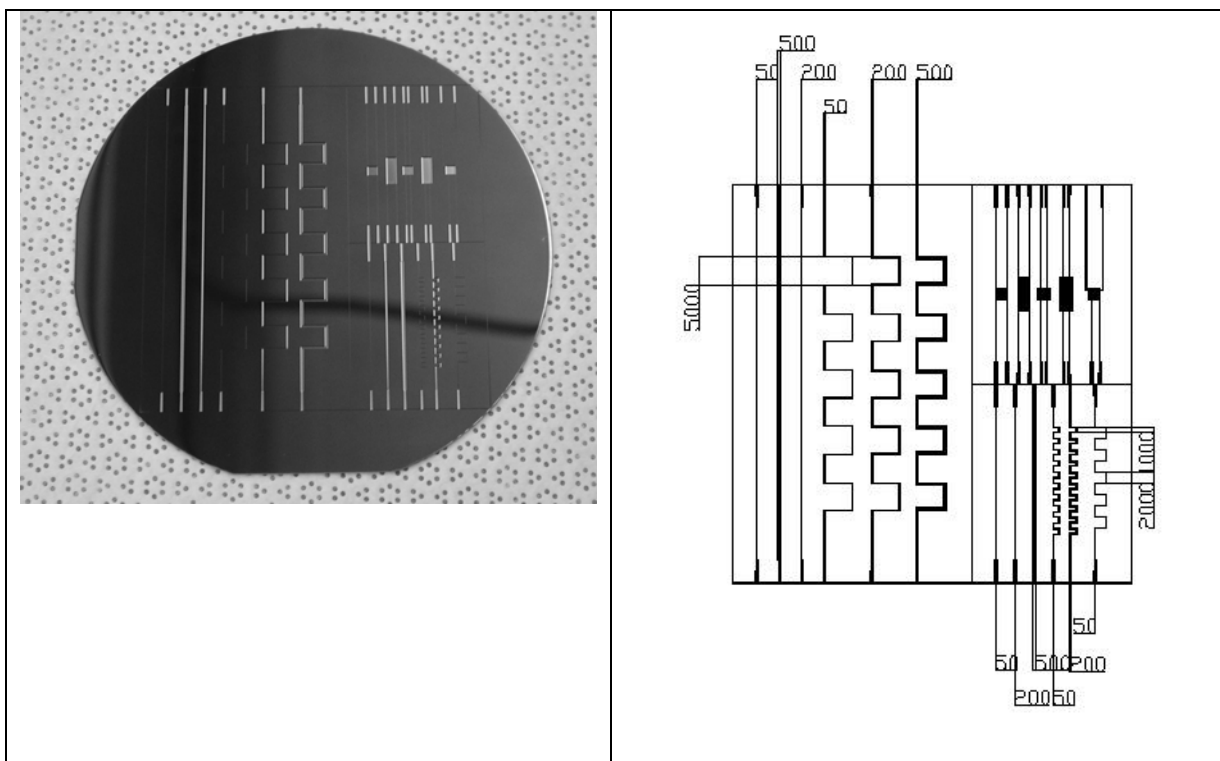
Figure 6: The etched wafer is shown on the left, with the design of the wafer shown on the right, with channel diameters indicated in microns.

The etched silicon wafer (Figure 6) was designed with three separate sections, giving channels of different lengths. Matching unetched but cut wafers were also obtained, and these were placed on top of the etched sections to provide the fourth channel wall, and seal the system. A clamping system was used to press the two halves together. The development of this model wafer system was funded by NSF Grant ECS-0003227.

It was found that it was not possible to apply sufficient pressure to the two halves to confine fluid flow within the bare channels. The bare silicon is so hydrophilic that water or protein solution could readily enter between the two pieces of Si due to capillary

22

action (Figure 7). However, leaking could be prevented via surface modification of the

wafer base and top with the highly hydrophobic silane 13F (Figure 7). Dye studies

clearly showed the change in performance
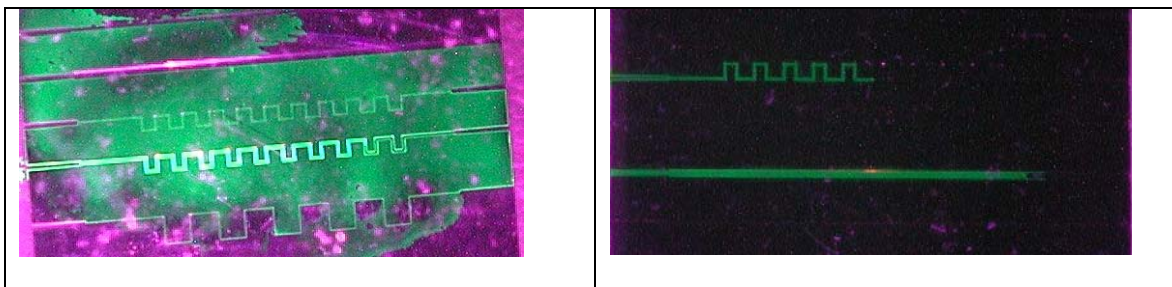
Figure 7:   Performance comparison with dye solution between untreated (LHS) and hydrophobic monolayer modified silicon wafer.

That this was not a singular property of 13F, but rather due to its high hydrophobicity,

was confirmed by further, successful, surface derivitisation experiments with the

hydrophobic surface created by N-octadecyl trichlorosilane (OTS)**.**

Protein adsorption under static conditions:

Early results with the capillary models showed that PEEK and Teflon had the highest

protein affinity, and were judged to be the easiest to study, if flow effects on adsorption

were to be observed. Protein adsorption studies under static conditions (no flow) were

carried out on samples of these two materials to provide a baseline for further comparison

with the flow case.

Four different proteins, alkaline phosphatase (AP), acid phosphatase (ACP), glucose

oxidase (GO) and horseradish peroxidase (HRP) were used to study the adsorption

behaviour with hydrophobic surfaces like PEEK and TEFLON. The experiments have

been done for a wide range of concentrations, from 2 mg/ml to 3 μg/ml.

Figures 8 through 11 below show the results of the static experiments performed on the PEEK and Teflon surfaces. Also shown in the figures is the analysis of the data via a Lineweaver-Burke plot. The proteins analyzed are (in order of increasing molecular weight) horseradish peroxidase (HRP), acid phosphatase (ACP), alkaline phosphatase (AP), and glucose oxidase (GO).

(a)   (b)
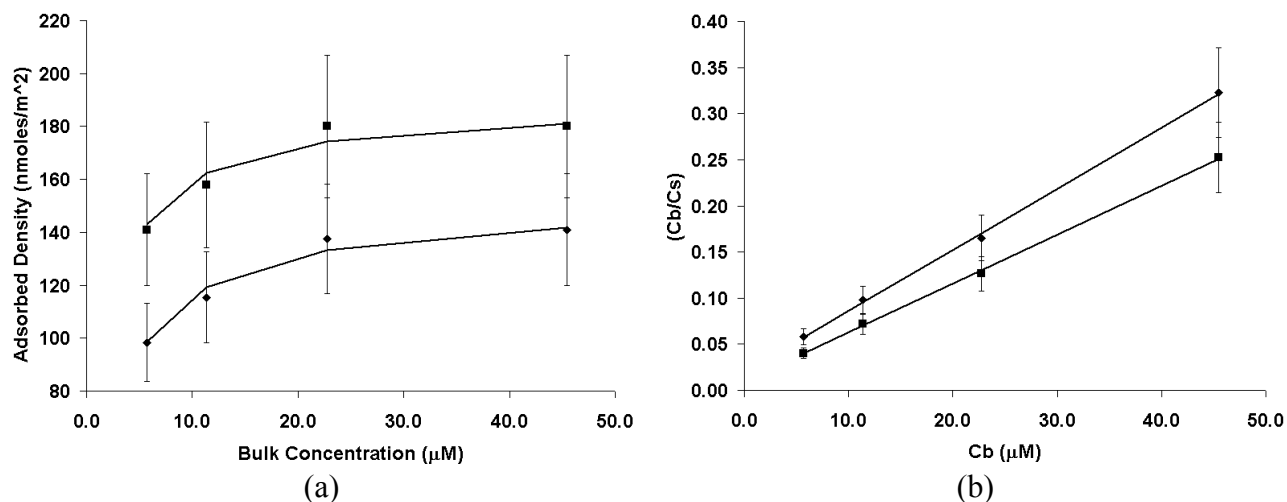
Figure 8: Static data for horseradish peroxidase (HRP). Diamonds represent data for PEEK and squares represent data for Teflon. Plots contain data as points with error bars and statistical fit shown as a solid curve. (a) Langmuir plot and (b) Lineweaver-Burke plot.

(a)   (b)
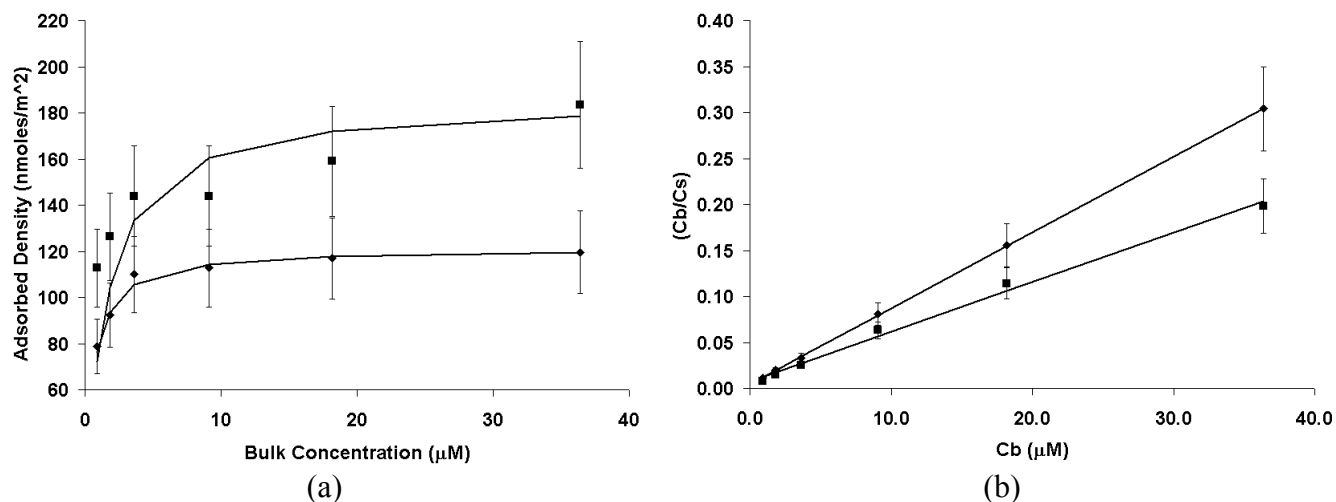
Figure 9: Static data for acid phosphatase (ACP). Diamonds represent data for PEEK and squares represent data for Teflon. Plots contain data as points with error bars and statistical fit shown as a solid curve. (a) Langmuir plot and (b) Lineweaver-Burke plot.

(a)   (b)
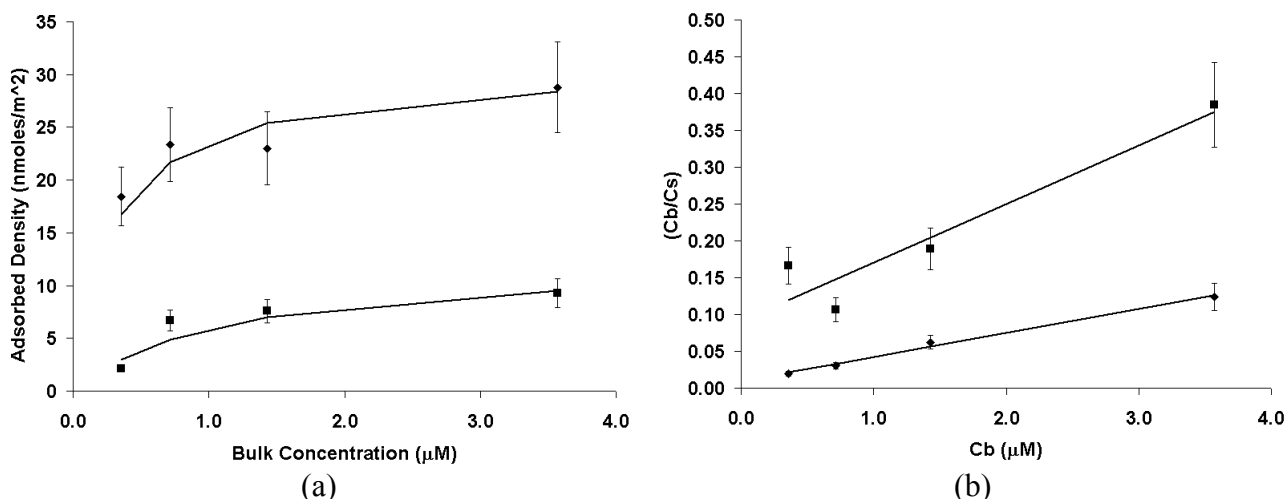
Figure 10: Static data for alkaline phosphatase (AP). Diamonds represent data for PEEK and squares represent data for Teflon. Plots contain data as points with error bars and statistical fit shown as a solid curve. (a) Langmuir plot and (b) Lineweaver-Burke plot.

(a)   (b)
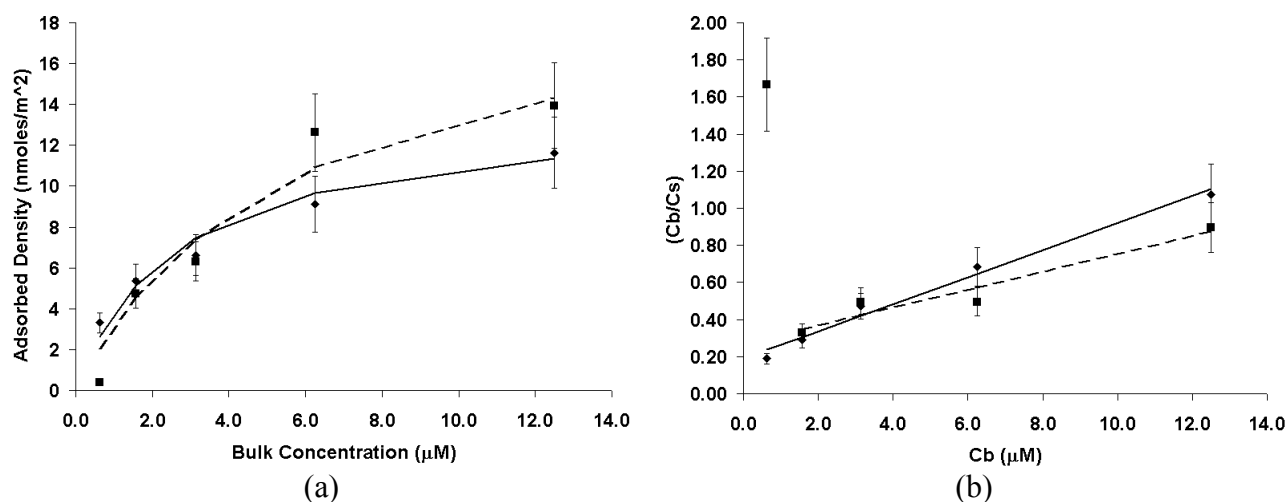
Figure 11: Static data for glucose oxidase (GO). Diamonds represent data for PEEK and squares represent data for Teflon. Plots contain data as points with error bars and statistical fit for PEEK shown as a solid line, and for Teflon as a dotted line. (a) Langmuir plot and (b) Lineweaver-Burke plot.

It was found that the amount of protein adsorbed on the surface increased with the concentration of the initial protein solution. In the case of Teflon, the adsorbed amount of protein usually reaches saturation at relatively low protein concentrations, whereas for PEEK saturation is seen at much higher concentrations. The μBCA assay was used to

quantitate the total amount of protein binding to the surface. Alkaline phosphatase and HRP are binding preferentially to PEEK surface whereas ACP and GO bind more to Teflon than PEEK. Acid Phosphatase binds aggressively to Teflon even at low concentration (50 μg/ml). Alkaline phosphatase takes 15 minutes to adsorb to PEEK and reaches saturation after 2 hours, whereas HRP binds within 5 minutes even at very low concentration (100 μg/ml). HRP activity can be detected on the surface even at very low concentrations (in picograms) with the enzyme assay technique.

Effect of flow on adsorption behaviour

CFDRC was able to extract rates of adsorption, rates of desorption and limiting surface coverage (P_{max}) (from the modeling system described later) and in all cases tested, where direct comparison between adsorption behaviour under static conditions (no flow) and flow conditions could be made, the presence of flow was shown to have a significant effect on adsorption behaviour.

The adsorption behaviour and curves of best fit of alkaline phosphatase (90 ng/mL) on PEEK at different flowrates is shown in Figure 12.
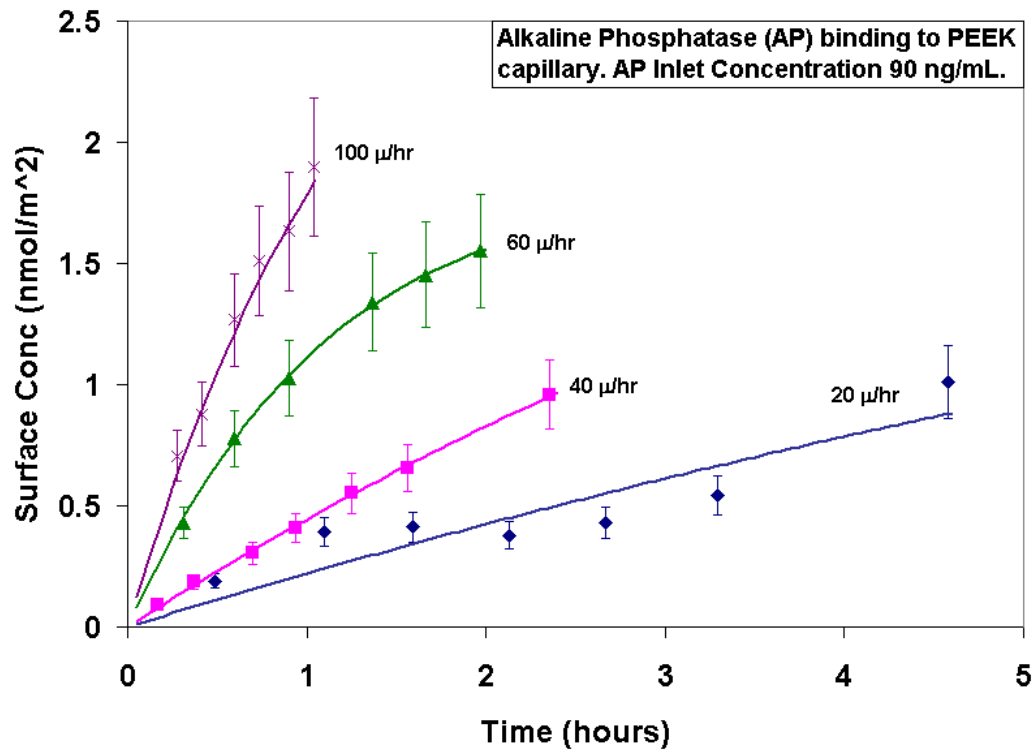
Figure 12: Adsorption behaviour and curves of best fit for alkaline phosphatase binding to PEEK capillary across a range of flowrates.

The best fit rate of adsorption (k_a) and limiting surface coverage (P_{max}) obtained at 90 ng/mL and 300 ng/mL are summarized in Figures 13 and 14.
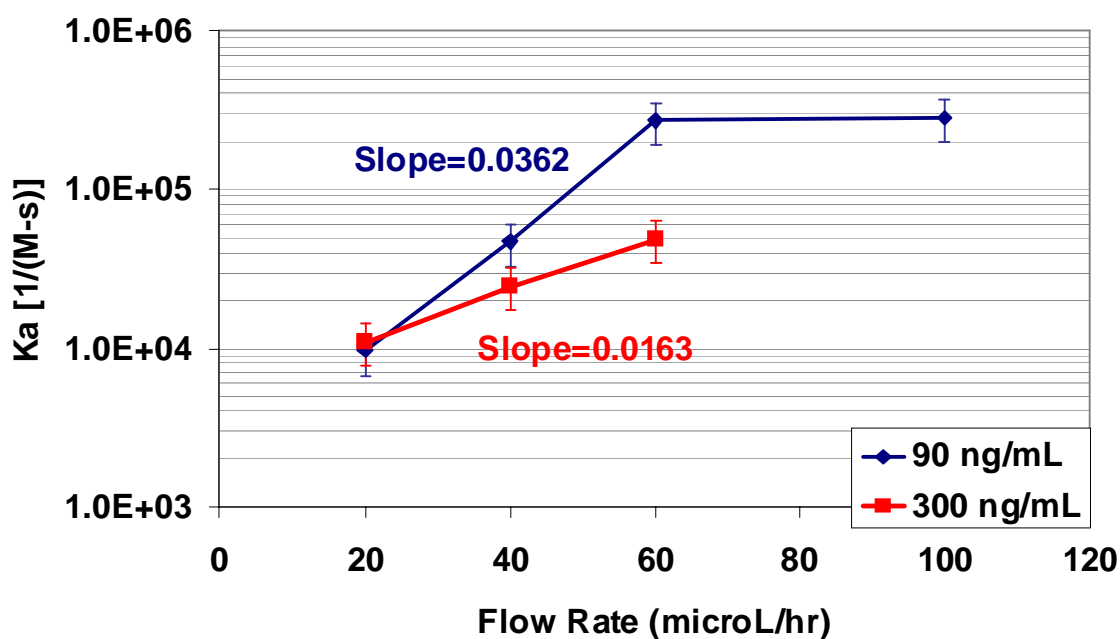
Figure 13: Rate of adsorption (k_a) as a function of flowrate for binding of alkaline phosphatase (90 ng/mL and 300 ng/mL) to PEEK capillary.
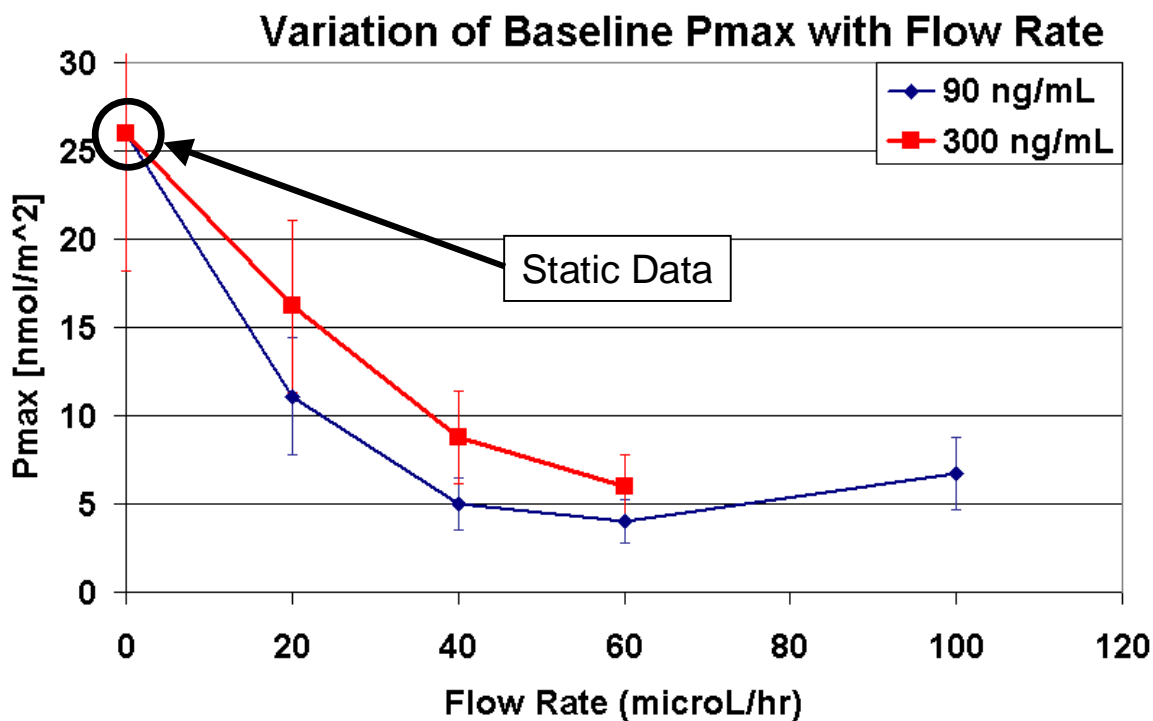
Figure 14: Limiting surface coverage (P_{max}) as a function of flowrate for 90 ng/mL and 300 ng/mL solutions of alkaline phosphatase binding to PEEK capillary.

It was found that k_d was exceedingly small, of order $5 \times 10^{-5} s^{-1}$. As the timescale of the adsorption experiment was much less than this, k_d was difficult to obtain with the same degree of precision as the other parameters, but further experiments (described below) were able to show that the rate of desorption could not be significantly faster than this. Fortunately, the solutions for P_{max} and k_a only weakly couple to k_d, and the confidence in these values is much higher.

The apparent concentration effect on k_a and P_{max} (Figures 13 and 14), seems to be principally due to the distortion resulting from fitting multi-site, flow dependent adsorption to a single site model. This was shown by constructing artificial adsorption isotherms for a surface with two adsorption site types (one with a flow dependent adsorption rate, the other independent) exposed to two different adsorbent concentrations at multiple flow rates. When these model isotherms were analyzed with the single site CFD model to extract the apparent P_{max} and k_a, the same trend was observed, with P_{max} larger and k_a smaller at the higher concentration, just as with the experimental data.

Calculating the adsorption isotherms (Figure 15) for this system at 90 ng/mL and 300 ng/mL, and then back extracting the apparent rates of adsorption and P_{max} with the baseline model correctly reproduced a higher P_{max} for 300 ng/mL and a lower k_a for 300 ng/mL (Figure 16).
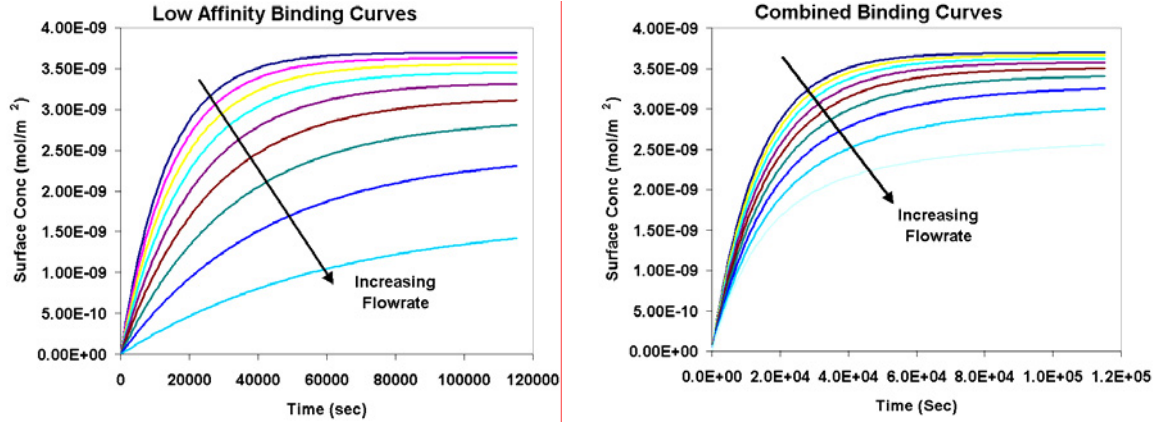
Figure 15: Two site binding model isotherms for 90 ng/mL. The model assumes that one site's ka is independent of flow (not shown) while the other site type has a decreasing ka with flow (left). The combined binding behaviour is shown on the right.
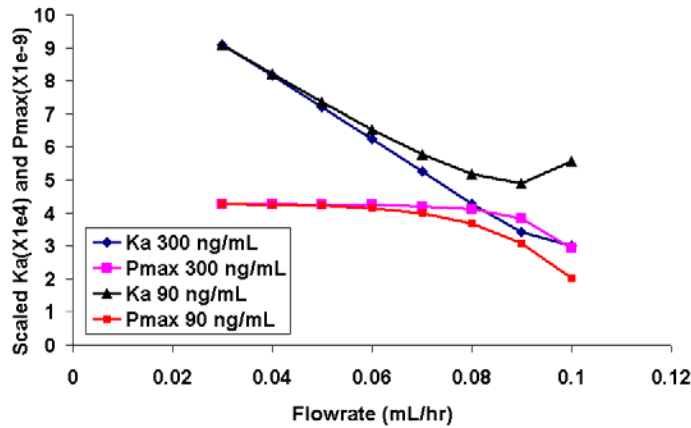
Figure 16: Simulated results for the k_a and P_{max} the baseline model generates given data from two site adsorption, one site flow dependent (80% of sites) and one site not (20%).

However, it was observed that the slope of k_a was negative with flow, rather than positive as observed experimentally. Further simulations showed that a linear flow dependence in k_a did not appear to be able to give the observed increase in k_a with flow, but that an exponential dependence did. That is, having the rate of adsorption depend on flow in the following form

$k_a(Q) = (k_{a0}/\beta)exp(\boldsymbol{Q})$

30

where β is a scaling factor, Q is the flowrate and $\underline{Q}$ is a bounded function of Q (to prevent k_a(Q) from tending towards zero) allowed the observed increase in the extracted k_a to be reproduced. This shows us that the apparent concentration dependence of P_{max} and k_a is actually a distortion induced by attempting to fit multi-site, flow dependent adsorption with a single site, fixed adsorption model. It also suggests an exponential form for the k_a dependence in an advanced model of protein adsorption might be appropriate.

An independent estimate for k_d was obtained by analyzing the desorption behaviour of the various enzymes on PEEK. In this case, the rate of desorption obtained from a total protein analysis of material washed off the PEEK surface can be compared with the loss of activity due to denaturation of the enzyme on the surface. These results were obtained under static conditions, and required much higher protein concentrations (for the total protein assay) than the capillary flow experiments. Fitting the desorption curve with a first order equation yielded a rate of desorption of $3 \times 10^{-6} s^{-1}$ for alkaline phosphatase, $2 \times 10^{-4} s^{-1}$ with horseradish peroxidase and $1 \times 10^{-4} s^{-1}$ for glucose oxidase. This compares with the flow extracted parameters of $5 \times 10^{-5} s^{-1}$, $1 \times 10^{-8} s^{-1}$ and $1 \times 10^{-6} s^{-1}$ respectively. Clearly the rates of desorption of the tested proteins are very small, regardless of the conditions used.

We also measured adsorption data under static and flow conditions for several other protein/surface combinations (Table 1). The same overall trend was consistently observed. In this case, for comparison with data obtained under static conditions, it is the ratio $K = k_a/k_d$ which is shown.

Table 1: A comparison of adsorption data obtained under static and flow conditions for alkaline phosphatase, glucose oxidase and horseradish peroxidase on PEEK and Teflon capillary surfaces.

		Alkaline phosphatase		Glucose oxidase		Horseradish peroxidase	
		flow	static	flow	static	flow	static
PEEK	K	$6x10^9$	$1.3x10^6$	$1x10^{13}$	$4x10^5$	$1x10^{11}$	$3x10^5$
	P_{max}	7.0	26	9	13	4	162
Teflon	K	$1x10^{14}$	$1.3x10^6$	$4x10^{13}$	$1.1x10^6$	$1.5x10^{10}$	$2.6x10^5$
	P_{max}	2	13	3	33	2	92

The manner in which k_a and P_{max} varied with flowrate suggested that flow limits the amount of time a protein molecule can spend near a given adsorption site, prior to adsorption occurring. As the flowrate increases, there are fewer and fewer adsorption sites involved in the adsorption process and P_{max} drops (Figure 17 and 18) but these sites are the most aggressive adsorption sites on the surface of the PEEK (k_a increases); flow results in much less of the surface being available for protein adsorption to occur (at least initially, since protein adsorption can incorporate cooperative effects at longer time periods) but these sites bind the protein strongly and efficiently, in line with the adsorption behaviour of heterogeneous surfaces.
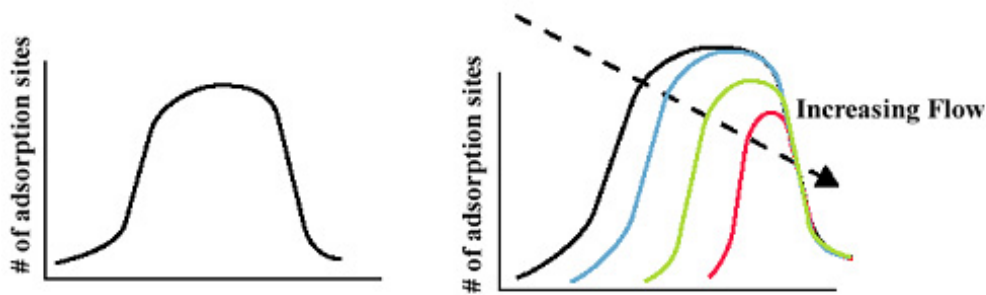
Figure 17:   Changes in the apparent rate of adsorption and surface coverage can be understood in terms of a range of adsorption behaviour being displayed by the surface. As flow is increased, fewer sites on the surface are able to adsorb protein due to kinetic limitations.

The adsorption (and possibly desorption) of proteins in microfluidic systems (and by extension the adsorption process for any surface active material being handled by a microfluidic system) is not going to be well described by a single rate constant, particularly if this data is obtained in a static or stagnant experiment, as such data often is.
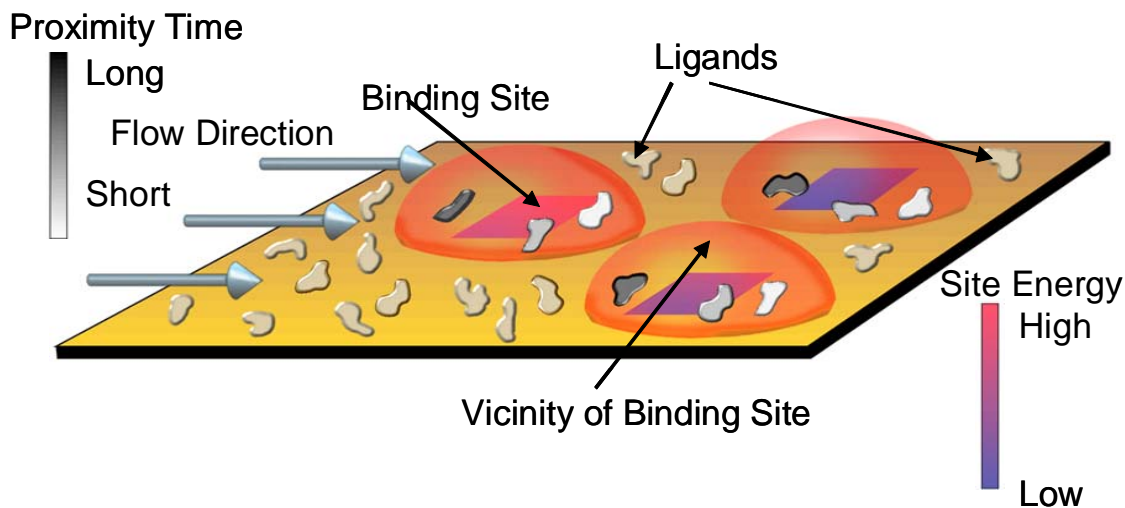
Figure 18: A range of binding sites and binding efficiencies contribute to the overall response of the surface to protein adsorption under flow conditions.

Ag assay for analysis of protein deposition patterns

We were able to show that the silver assay (method development funded by NSF Grant ECS-0003227) could resolve *spatial* differences in protein deposition with excellent resolution. In this case, protein solution was passed through a 200 μm wide serpentine channel from the model system, and the flat lid exposed to the silver staining solution (Figure 19). The inlet concentration of protein was set to 300 ng/mL at a flowrate of 0.10 mL/hr. The binding behaviour was then simulated. The adsorption parameters were taken from the earlier fitting of alkaline phosphatase binding to Teflon (which highlights

the utility of having a general purpose adsorption model with a validated database of parameters). A comparison of the silver staining assay and the predicted protein binding (Figure 20) shows good qualitative agreement. Specifically, we note the correspondence in the location of dead zones where little protein is being deposited, and in the overall shape of the deposited regions. Observing that the darkness of the silver stain is related to the amount of protein deposited, the modeling is seen to be in good semi-quantitative agreement with experiments. These images clearly show the presence of the protein, and further comparison with the predictions obtained from finite element analysis provided by CFDRC showed many of the same features.
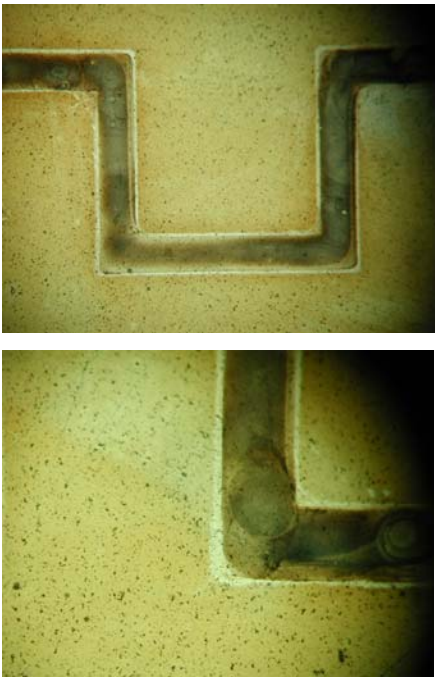
Figure 19: Silver deposited on the surface of the flat wafer used to seal the microfluidic system clearly shows that the protein has been successfully retained within the channels. These are 200 μm features, showing that the resolution of the test allows it to be applied to microfluidic systems.

Our goal is to develop the silver assay to the point where high spatial resolution XPS (or some other technique sensitive to silver) can be used to determine the adsorbed protein concentration profile in microfluidics channels, for comparison with the predictions made by the CFDRC code (Figure 20). This aspect of the work could not be fully explored within the lifetime of this project.

Silver Staining

Expt

Model

Dead Zones
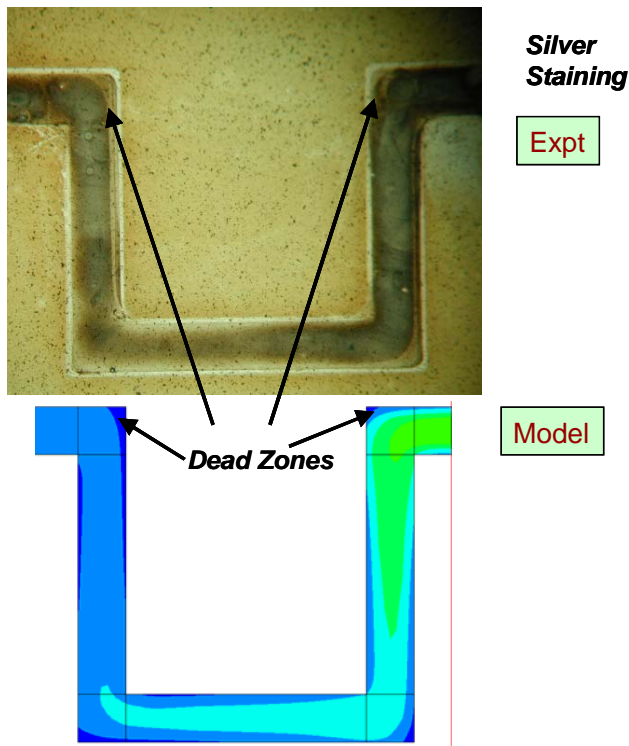
Figure 20: Comparison between the features observed using the silver staining technique with those predicted by the CFDRC simulation shows qualitative agreement. Different methods for obtaining a quantitative measurement are being investigated.

Protein adsorption isotherms from SAM coated channels

Experiments to investigate protein adsorption in the etched silicon wafers channels (Figure 20) allowed comparison between 13F modified channels and adsorption data obtained from Teflon capillaries (Figure 21). The overall protein adsorption behaviour obtained with the 13F modified silicon microchannels is very similar to that obtained with Teflon. However, it would seem that the 13F surface consistently shows much less protein adsorption at the same protein concentration than the Teflon surface.
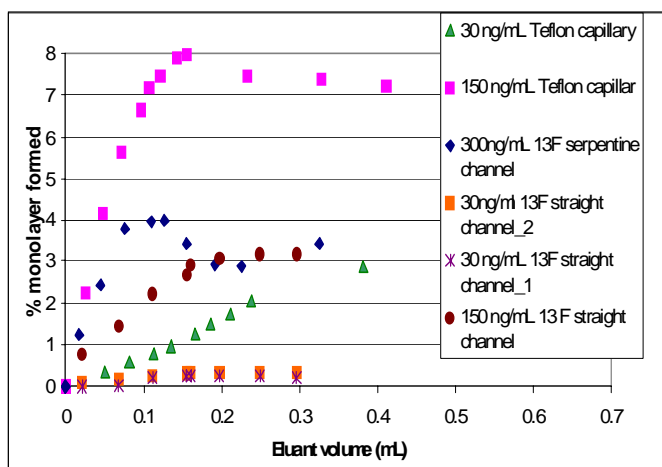
Figure 21: Comparison of the protein coverage obtained in the 13F modified wafer channels with that obtained from a Teflon capillary.

Protein adsorption analysis by SDS-PAGE

SDS-PAGE was investigated as a tool for measuring protein adsorption. Calibration curves for bovine serum albumin (BSA) demonstrated excellent detection limits (Figure 22). This allowed comparison with results obtained by XPS with those obtained by SDS-PAGE densitometry (Figure 23).

Lane	1	2	3	4	5	6	7	8	9	10
ug/ml	1.0	2.0	3.0	4.0	5.0	6.0	7.0	8.0	9.0	10.0
ng/lane	0.03	0.06	0.09	0.12	0.15	0.18	0.21	0.24	0.27	0.30

$y = 0.9224x + 2.1867$
$R^2 = 0.9925$
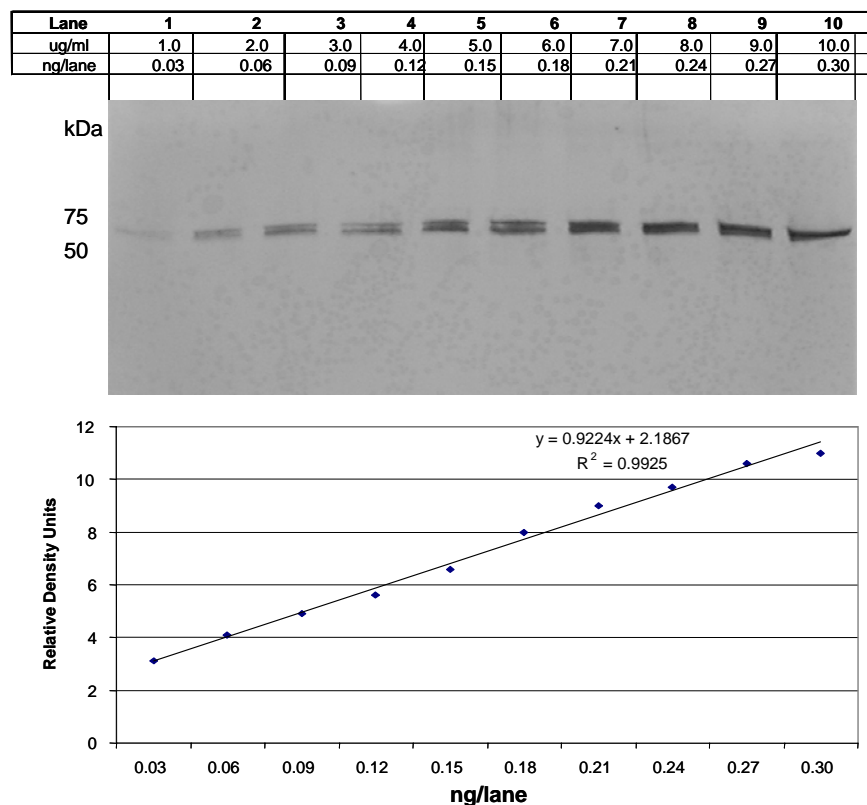
Figure 22: SDS-PAGE shows excellent linearity over a wide range of concentrations.
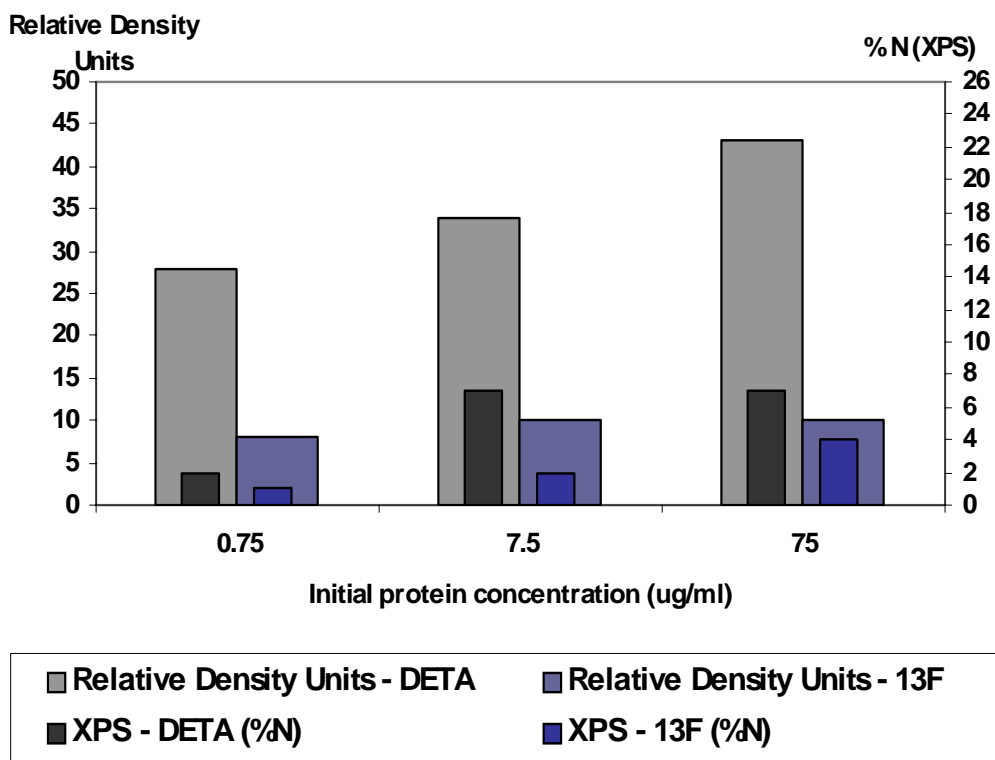
Figure 23: Comparison of results from XPS analysis of adsorbed proteins with those from SDS-PAGE.

37

Since SDS-PAGE allows different proteins to be separated by molecular weights, it will be a valuable technique for testing the adsorption behaviour of protein mixtures. Experiments with serum on DETA and 13F (Figure 24) surfaces showed that 13F adsorbs a very small amount of protein, in line with earlier results (Figure 21), obtained via the enzyme assay. It was also found that DETA adsorbs significantly more protein than 13F.
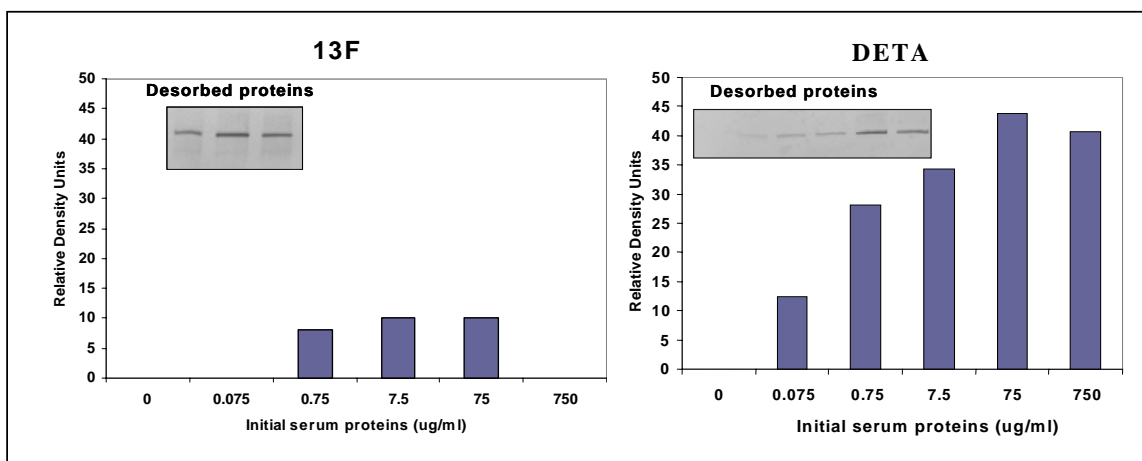
Figure 24: Comparison of protein adsorption to 13F and DETA.

Competitive protein adsorption

The adsorption behaviour of AP and BSA in competition with each other (Figure 25) was compared. It seemed that the presence of BSA had very little effect on the adsorption of AP. Traditionally, BSA is regarded as a passivating protein, able to adsorb to surfaces in preference to other proteins, and prevent any further adsorption from occurring. What we found was that this behaviour was not being followed at relatively low protein concentrations. This may be due to there being insufficient BSA present to occupy all the available adsorption sites, but that is contradicted by finding that the adsorption behaviour of AP is almost unchanged when the surface is pre-exposed overnight to BSA.

If AP was much smaller than BSA then it could be adsorbing in the interstices between adsorbed BSA, but as AP and BSA are of a similar size this doesn't seem likely. It could also be that BSA and AP adsorb preferentially to different types of sites. If this is the case, then the differences in the surface of AP vs BSA could hold important clues as to the mechanism of protein adsorption.

Influence of Albumin on Alkaline Phosphatase (AP) Adsorption
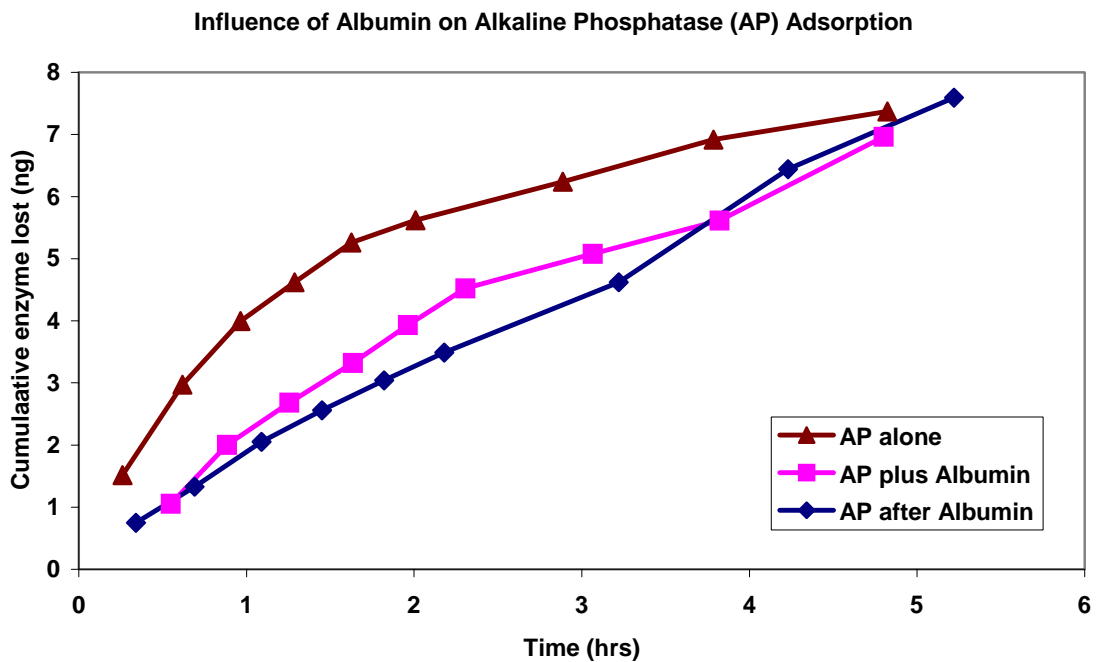
Figure 25: Comparison of the adsorption behaviour of alkaline phosphatase with and without the presence of bovine serum albumin.

Protein desorption vs denaturation

The combination of μ-BCA and enzyme analysis allowed enzyme activity due to desorption vs that due to denaturation to be distinguished. Protein denaturation to date has been principally probed by circular dichroism (CD), which although a powerful

method for showing changes in protein conformation, is limited to samples which transmit light in the UV. The approach used here does not have this drawback.

With this method, an enzyme could be adsorbed to a surface, and then immersed in the enzyme substrate solution, giving an indication of the activity of the enzyme on the surface. Removing the enzyme from the surface with 0.2% SDS solution allowed the total protein present on the surface to be measured with the μ-BCA assay, and compared with the results from the enzyme activity test (Figure 26). The change in protein amount measured by the μ-BCA method is compared with that measured by enzyme activity. It is immediately apparent that most of the loss of activity is due to denaturation of the AP rather than desorption. Further tests, using HRP on PEEK, showed that in that case loss of detectable active enzyme was principally due to desorption.   These results will allow the advanced model to start to split the currently monolithic rate of desorption into multiple terms covering both the rate of desorption and the rate of denaturation, which is an objective of future research.
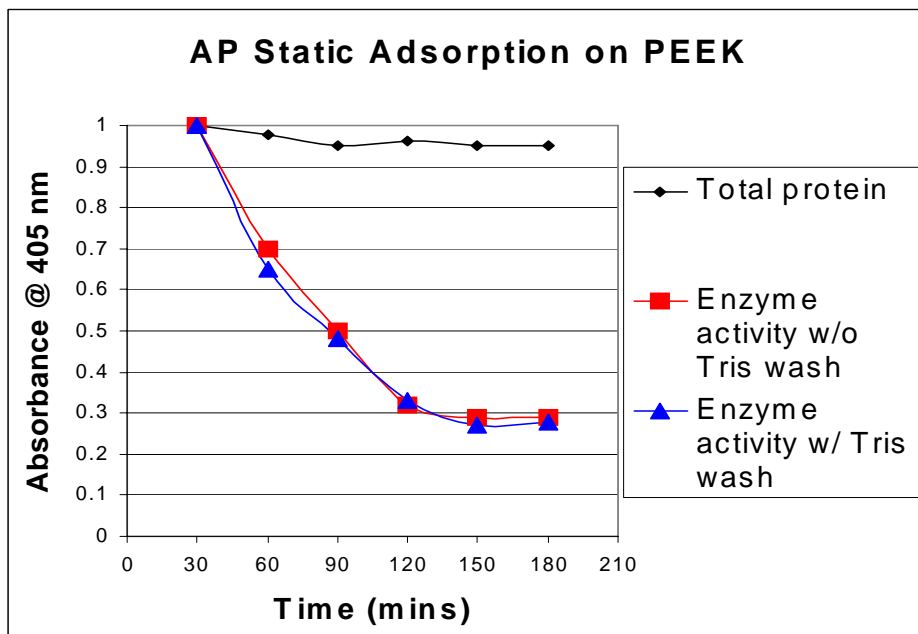
Figure 26: Change in measured amount of alkaline phosphatase (AP) on PEEK by μ-BCA and enzyme assay. The μ-BCA clearly shows that the total protein amount decreases only slowly, while the activity of the AP drops sharply. This allows us to distinguish the rate of desorption from the rate of denaturation.

In situ spectroscopy during plasma modification

The high pressure DC plasma (Figure 27) was shown to alter the surface morphology of the channel (Figure 28), and further work investigated what chemical changes occur in the channel (method development funded by NSF Grant ECS-0003227). The successful creation of a high pressure plasma [Evju et al. 2004] opens up the possibility of selectively modifying parts of a microfluidic system in real time, in response to changing surface requirements.
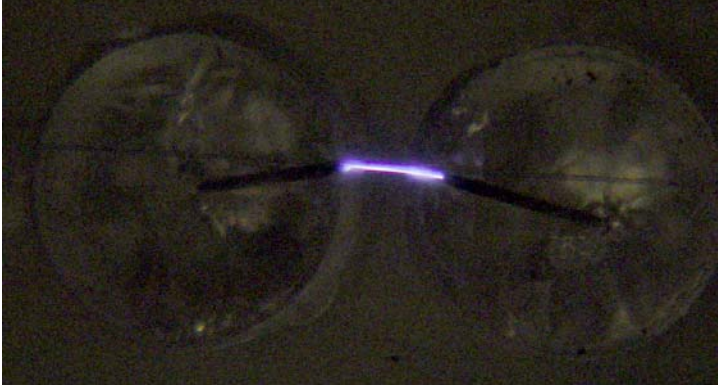
Figure 27: 1.9 mm Long Air Plasma in PMMA μ−channel. 1 atmosphere pressure, ~5 kV.
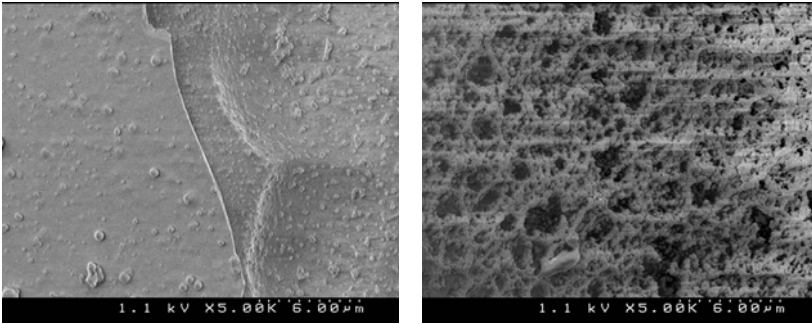
Figure 28: Different structures found in the PMMA surface after the application of the plasma. The sheet and dimple surface (LHS) was found at the anode while the highly porous surface (RHS) was found at the cathode.

It was also shown that emission spectra could be obtained from within the channel during the plasma treatment. Figure 29 shows the emission spectra obtained during the He plasma treatment of polystyrene channels; the channel dimensions are 200 μm wide by 6mm long.
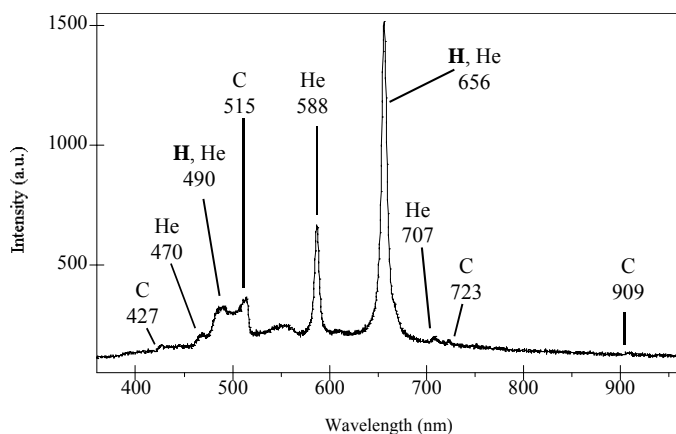
Figure 29:   The emission spectra from a He plasma inside a polystyrene microchannel.

Different gases have been used in the plasma as a means of functionalizing the polymer surface. Figure 30 indicates the emission spectra of the plasma from a mixture of helium and hexafluoroethylene in a polystyrene channel. This gas mixture was tested to see if it could be used to fluorinate the channel walls.
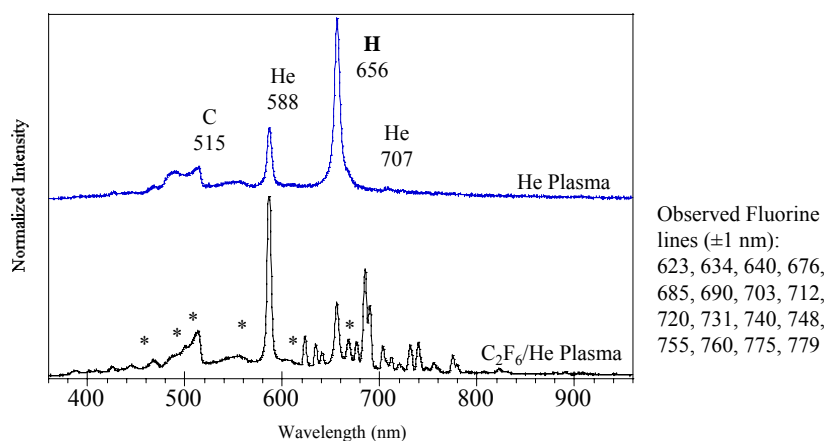
Figure 30:   The emission spectra from a mixed hexafluoroethylene/He plasma inside the polystyrene channel.

43

Surface analysis of plasma modified polymer

XPS of the polystyrene was used to compare treated with untreated; as is shown in Figure 31 both the anode and the cathode end of the polystyrene channel shows the presence of fluorine, and this is further confirmed via imaging XPS (Figure 32).
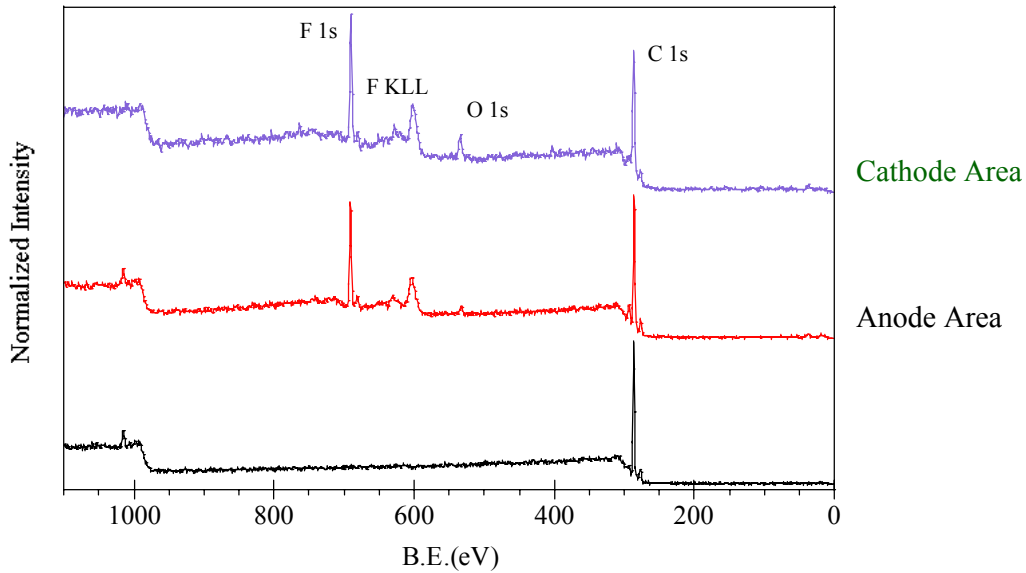
Figure 31: XPS of the polystyrene channel in its pretreated state (bottom trace) and treated (top and middle trace) shows the clear addition of a peak due to the presence of fluorine.
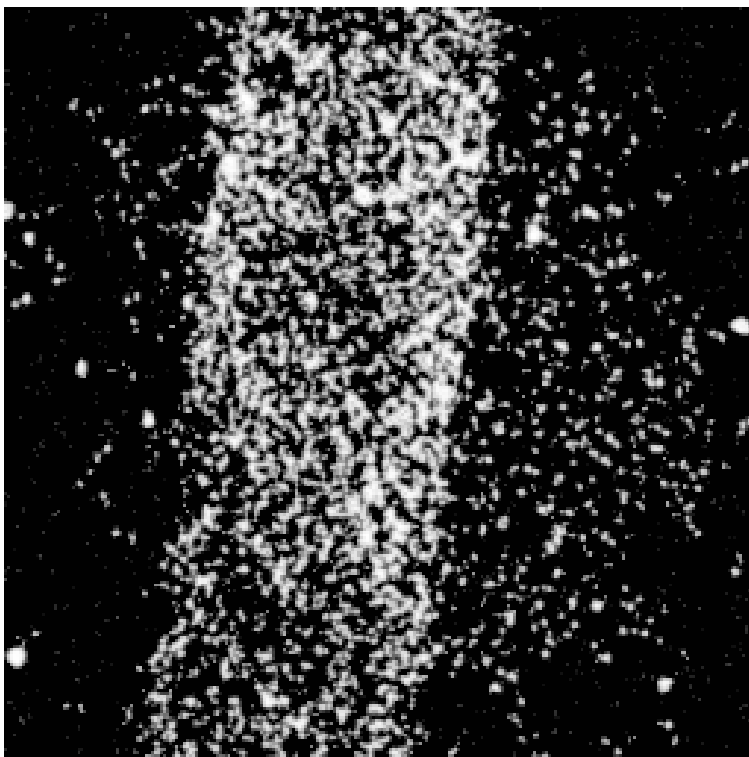
Figure 32: Imaging XPS for the presence of F shows an outline of the channel.

Secondary ion mass spectroscopy (ToF-SIMS) was also able to confirm the presence of fluorinated products inside the channel. At the conclusion of this phase of the work it was unknown if the polystyrene was being fluorinated or if a new polymer surface was formed over the top of the substrate. Evidence from SEM images, however, suggests that a new polymeric layer was being formed, rather than the direct incorporation of fluorine into the polystyrene.

Determination of the extent of Protein Adsorption on Polymeric Microfluidic Channels

NIST has developed and performed several analytical techniques to determine the extent of protein adsorption on polymeric microchannels both during fluid flow through the microchannel as well as in a static environment. Current monitoring techniques were utilized for the determination of the electroosmotic flow (EOF) of a number of plastic microchannels. The proteins were added to the microfluidic channel and the channel was allowed to incubate, at room temperature, for two hours. In all of the cases studied, the EOF mobility of the channel incubated with the protein solution was much lower than that of the pristine microchannel (Figure 33). These trends were also noted while using other proteins such as glucose oxidase, myoglobin, trypsinogen, and alkaline phosphatase.
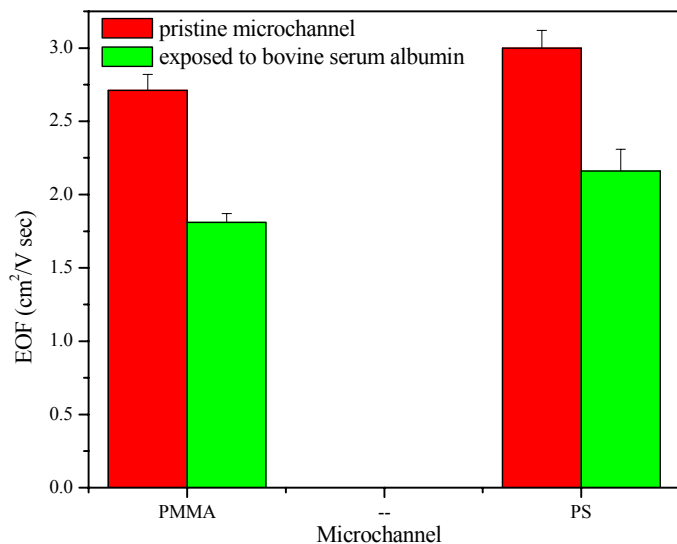
Figure 33: EOF values of pristine poly(methyl methacrylate) (PMMA), PMMA exposed to bovine serum albumin, pristine poly(styrene) (PS), and PS exposed to bovine serum albumin.

Proof-of-concept dynamic EOF studies were also performed using fluorescence monitoring. These experiments employ a neutral fluorescent dye marker, rhodamine B; the dye was introduced into one of the two buffer wells on a straight poly(styrene) microchannel. Because there is no electrophoretic mobility associated with a neutral species, the dye flowed through the channel at the electroosmotic flow rate. Displayed in Figure 34 is a graph of the flow profile of rhodamine B at various times. Current studies involve the addition of a protein solution into the microchannel and discerning the flow profiles of the rhodamine B adsorbed as it flows through the protein-covered microchannel.
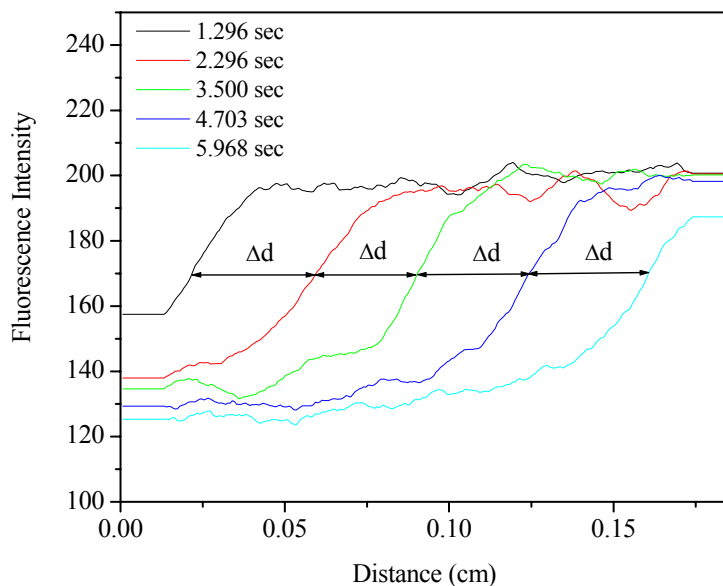
Figure 34: Fluorescence intensity of a rhodamine B front versus distance moved within microchannel.

Protein adsorption and EOF

Initial experiments into monitoring the real time adsorption of BSA to silica capillary were quite promising. It was found that the interaction of BSA with the silica surface could be readily detected as a change in the EOF flow (Figure 36). During cycle 8, the

47
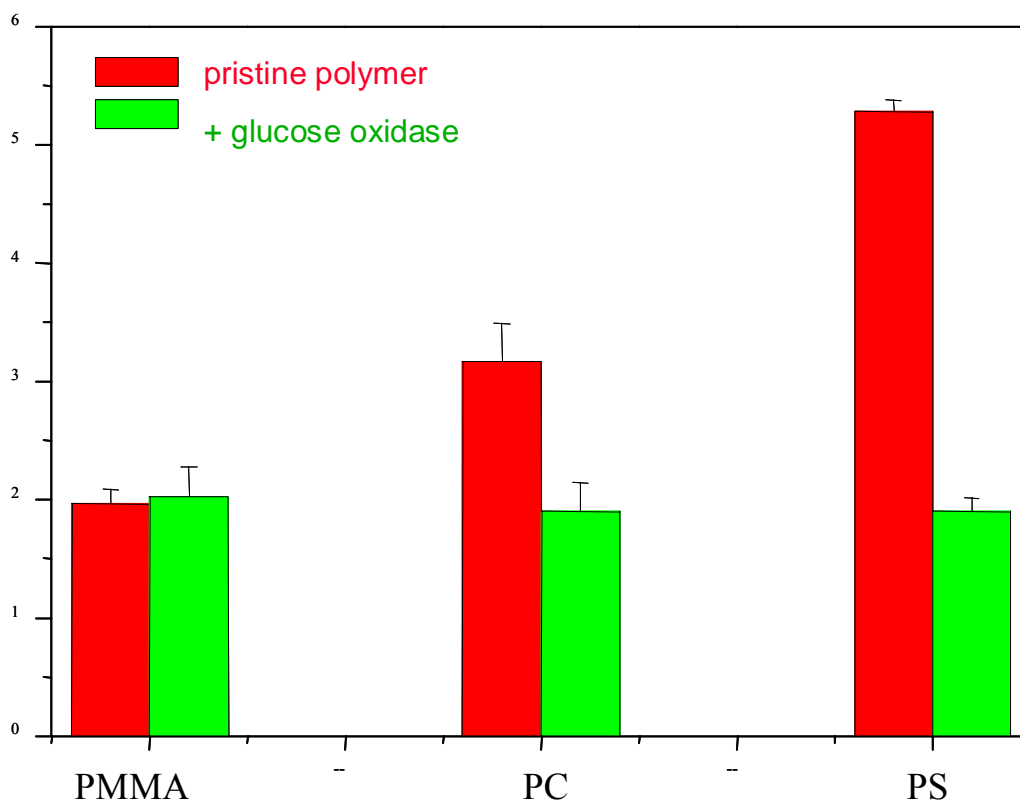
Figure 35: The adsorption of glucose oxidase to different polymer surfaces was shown to have a significant effect on electroosmotic flow. Since the change in EOF can be monitored dynamically, this could allow protein adsorption to be followed in real time by its effect on EOF. PMMA: polymethylmethacrylate PC: polycarbonate PS: polystyrene

capillary is being exposed to BSA for the first time, and no effect on EOF was noted during either the forward or reverse cycles. At cycle 9 the electro-osmotic mobility (μ_{eof}) starts to decrease, first rapidly and then slower, and by cycle 25 the final electro-osmotic behaviour has been more or less established.
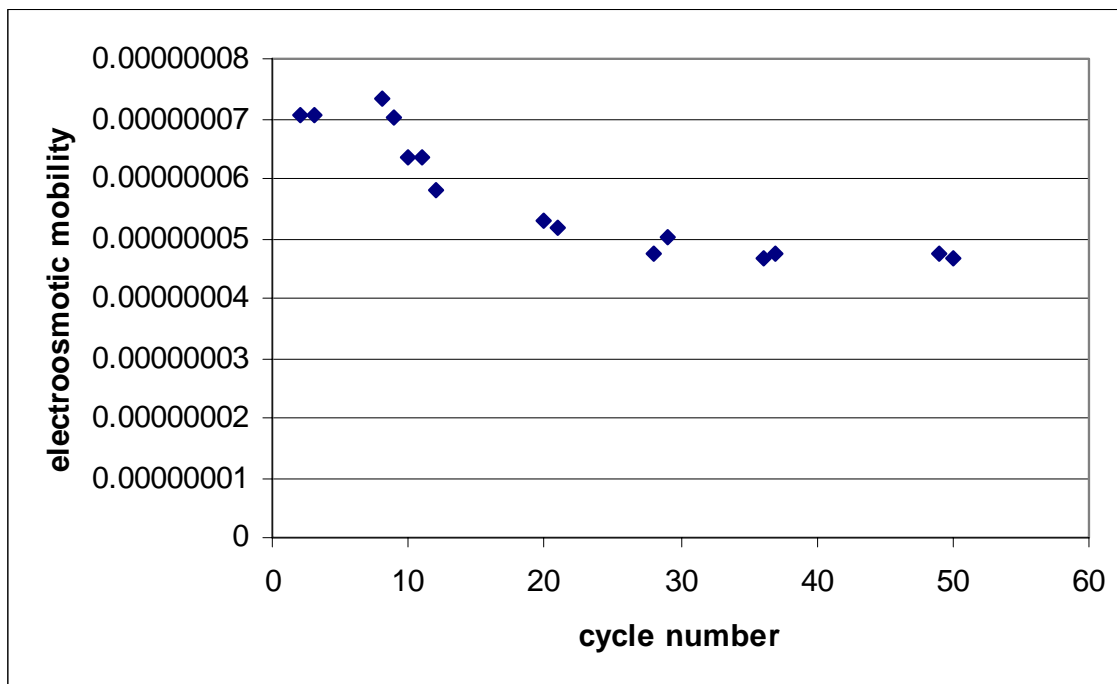
Figure 36: The effect on EOF of adding BSA to the buffer. 300 ug/mL in 10mM phosphate solution, pH= 7.4.

Figure 37 was obtained by replacing the protein bearing solution with fresh buffer. There is an immediate (too fast to be resolved) return to an electro-osmotic mobility which is approximately 85% of the initial reading, followed by a rapid leveling off at a mobility which is only just smaller than that measured for the clean silica capillary. Under these conditions, it would appear that the BSA can be mostly desorbed from the surface. It is generally found that the change in EOF with protein adsorption is linear with respect to the amount of material on the surface; in this case, it would appear that ~90% of the BSA is removed upon replacement with fresh buffer. These results were obtained with an applied voltage of 1000V. Interestingly, repeating the desorption experiment with a much lower applied voltage (400V, not shown) resulted in almost no recovery of electro-osmotic mobility. Clearly, a major component in the desorption behaviour of BSA is the electrophoretic force being applied by virtue of BSA's overall charge of -17 at pH 7.4.
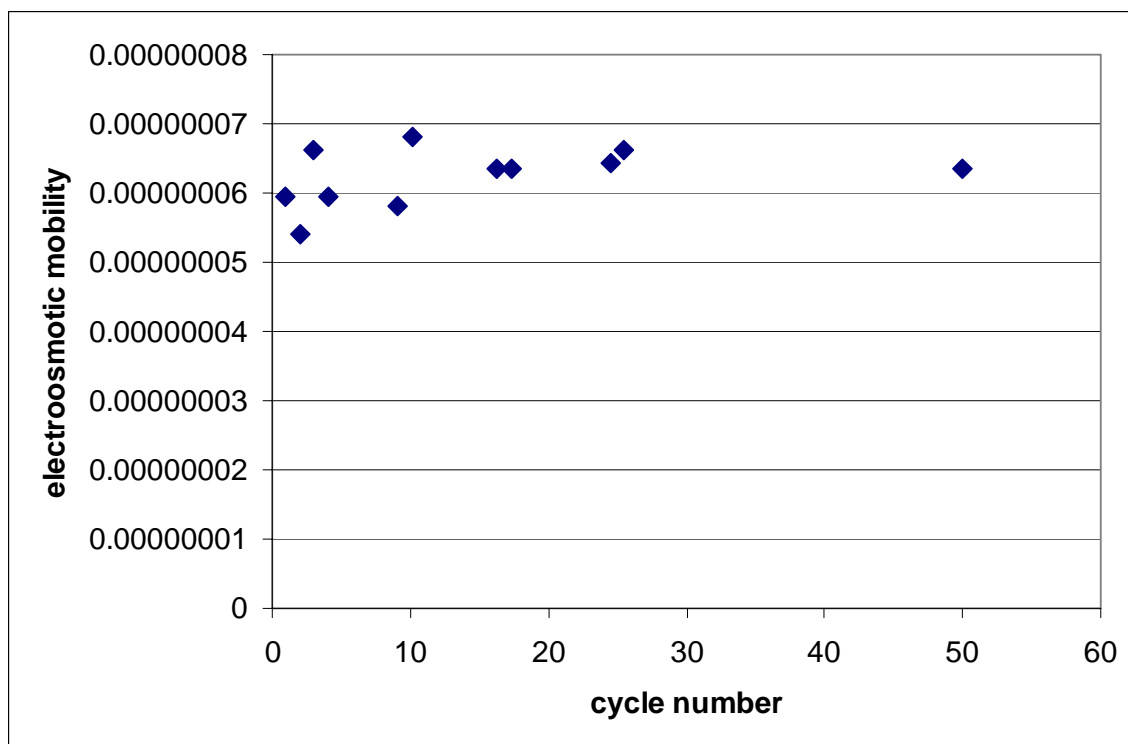
Figure 37: The effect on EOF of replacing the BSA solution with fresh buffer.

Carrying out the same experiment with BSA adsorption then desorption but at the protein's isoelectric point of pH 5 had a quite different result. In this case, it was possible to achieve a rapid drop in the electro-osmotic mobility, much faster than was found at pH 7.4. In the instance shown (Figure 38) BSA was added to the system for one cycle only, then removed and replaced with fresh buffer. No significant recovery of electro-osmotic mobility was observed. If, as in this case, the pH 5 buffer was then replaced with buffer at pH 7.4, there was a rapid increase in electro-osmotic mobility to a value close to that observed in the adsorption part of the experiment at pH 7.4, but without any further increase. Thus, it is most likely that the BSA is still present on the silica surface, but at pH 7.4 it is supplying extra surface charge to help drive EOF.

It would appear that BSA adsorbed to the surface at pH 5 is much harder to remove from the surface, even with the added effect of electrophoresis with the change in pH. Clearly, this behaviour is very important in cases, such as isoelectric focusing where the protein/s are deliberately concentrated at their isoelectric point/s in the capillary.
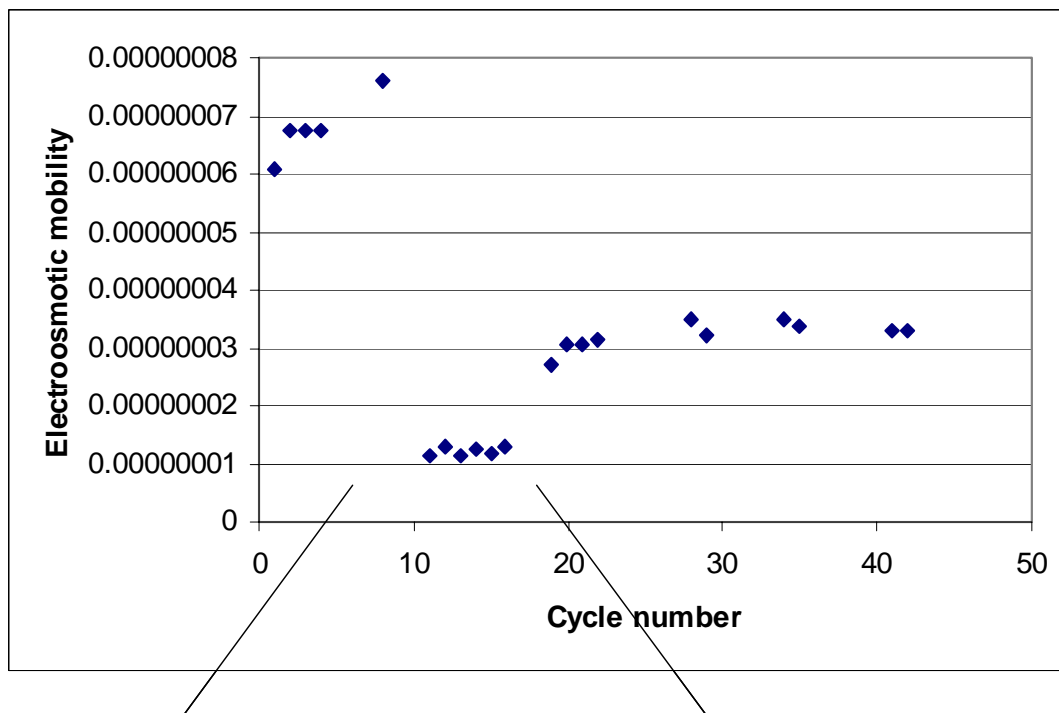
Figure 38: Exposure of silica capillary to BSA at pH 5 shows an immediate drop in EOF. Changing the buffer to pH 7.4 brings some increase in EOF, but comparison with the results obtained in Figure 36 suggests that it is more likely that this recovery is due to the additional charges on the BSA at pH 7.4, than desorption.

Although there was a clear change in electro-osmotic flow with protein adsorption, the reasons why were not immediately obvious. The silica surface has a negative charge at pH 7.4, as does the BSA. So the adsorbed BSA, with the same charge sign as the surface,

51

should be increasing the electro-osmotic flow, not reducing it as was observed. Further experiments, at a range of buffer ionic strengths, showed that as the buffer solution is reduced in concentration from 10 mM to 1 mM there is a decrease in the effect protein exposure has on the EOF (Figure 39) – this can be seen by the upward trend in the electro-osmotic mobility as the buffer concentration is reduced, as well as the convergence of the mobility of the clean silica surface and the system post protein exposure, shown by the decrease in the ratio of μ_{eof}(silica)/ μ_{eof}(silica + protein).
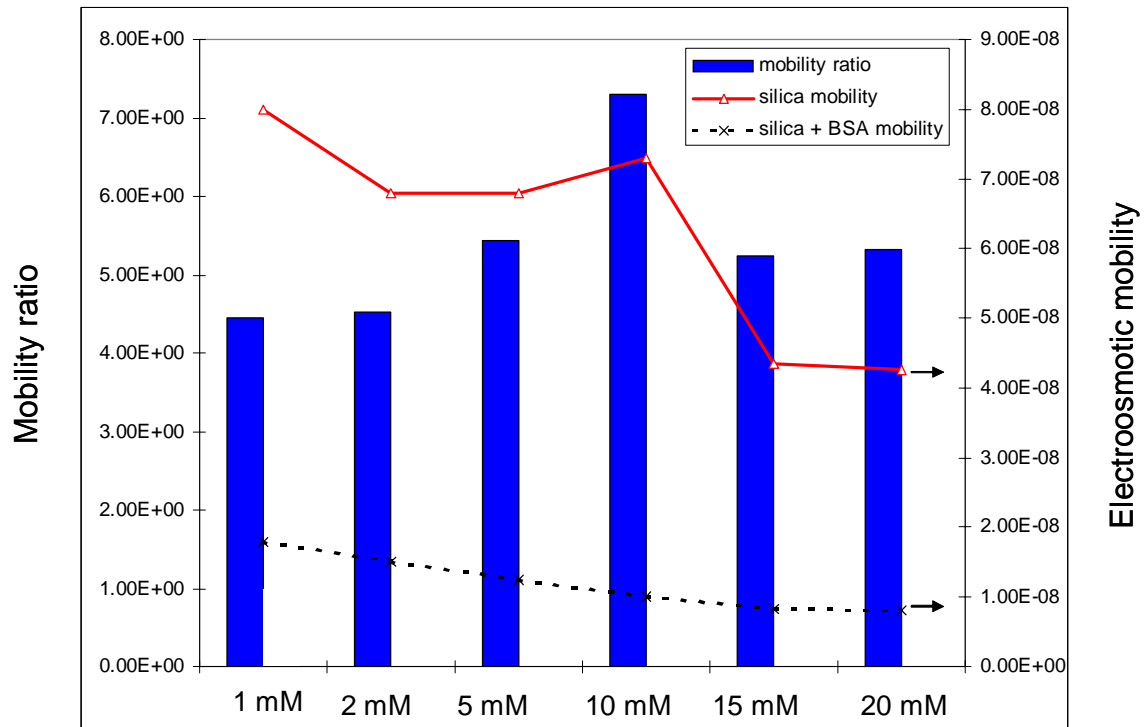
Figure 39:   Change in EOF with buffer concentration.

Based on this series of experiments, it was concluded that the most consistent reason for the decrease in EOF with protein adsorption was that the physical presence of protein at the wall hindered the fluid, making it harder to flow past the surface. EOF is established

52

very close to the wall, a consequence of the ion double layer formed near a charged surface, and thus adsorbed species could readily act to make flow more difficult. If the ionic strength is reduced, the Debye length is increased, and extends out past the adsorbed layer of protein, reducing the impact on electro-osmotic flow, exactly as observed. This has important consequences for choice of conditions in EOF based systems, if the effect of adsorption on EOF behaviour is to be minimized.

Laser ablation for the formation of polymeric microchannels

NIST developed laser ablation as a technique for modifying the surface of a microchannel *as the microchannel was fabricated*, and to characterize the surface modifications and ascertain the EOF characteristics of the modified microchannels. It was determined that the EOF can be substantially increased or reduced depending on the conditions under which the microchannel was fabricated.

Control of the organic chemical moieties present on the surface of the microchannels was achieved by ablating the microchannels under a variety of different atmospheres. Displayed in Figure 40 is a schematic of the laser ablation process. The laser emits light at 193 nm, and this is passed through a series of mirrors and apertures, finally focusing on a polymeric substrate. The polymeric substrate is housed in
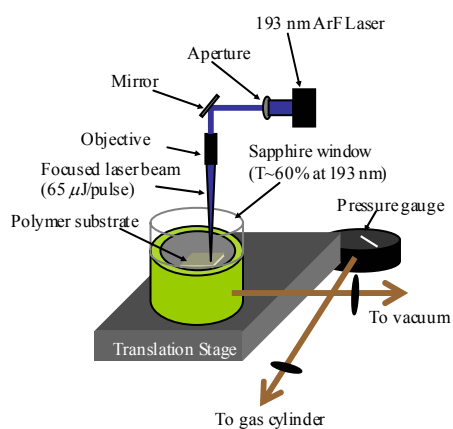
Figure 40: Schematic of laser ablation process.

53

a stainless steel chamber and covered with a transparent (60% transparent) sapphire window. The chamber can be evacuated and subsequently flooded with a variety of different atmospheres, namely, air, N_2, He, O_2, NH_3, and H_2SO_4 (gas). As the ablation process occurs, a plasma is formed at the tip of the laser beam, and the characteristics of the plasma are dependent on the atmosphere under which the ablation occurs. The surfaces of microchannels ablated under a variety of different atmospheres were probed using several different surface analytical techniques, including X-ray photoelectron spectroscopy and transmission infrared spectroscopy at Brewster's angle. Significant differences in the composition of surface organic groups with respect to the atmosphere under which the substrate is ablated were found.
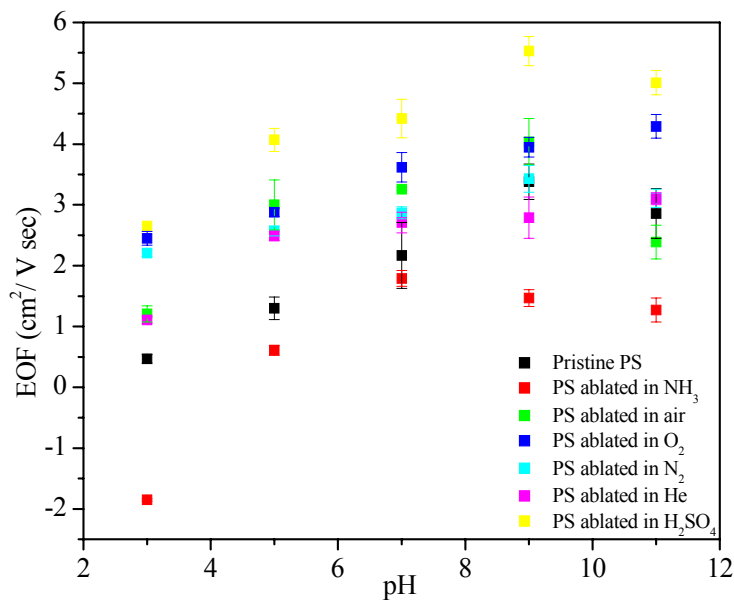
Figure 41: Change in EOF as a function of pH and laser ablation under different atmospheres.

The change in EOF rates with respect to pH of microchannels that have been fabricated using laser ablation under a number of different atmospheres was measured (Figure 41). The control in this experiment is a microchannel that is fabricated using embossing, such that the surface of the microchannel is pristine PS. As can be noted, the EOF rates of the pristine PS are fairly constant throughout the pH range studied. In the case of microchannels ablated under air, however, it is noted that the EOF rates are higher than the pristine PS at all pH values studied. The differences in the EOF rates are due to the presence of negative charges on the surface of the microchannels ablated in air that have been incorporated into the surfaces by the ablation process. Further, the EOF rate of the channels ablated in air increases substantially at pH 5 due to the presence of an organic chemical moiety that deprotonates at pH 3-5. Other analytical studies have pointed to the fact that carboxylic acids populate the surface of the microchannels ablated under air, consistent with the EOF studies.

In addition to the EOF characteristics of microchannels ablated in air, we have studied the characteristics of those channels ablated in inert atmospheres such as He and N_2. As can be seen in Figure 41, the EOF rates of microchannels ablated under each of these two inert atmospheres is very similar for all of the pH values studied. The pH values for microchannels ablated under N_2 and He are slightly higher than the EOF rates of pristine PS, which could be due to air contamination of the stainless steel chamber before or during the ablation process.

Microchannels ablated under an atmosphere of O_2 display an increased EOF rate for all pH values studied compared to pristine PS microchannels or microchannels ablated under inert atmospheres. In addition, the EOF rates are fairly consistent, yet increase slightly, as the pH is increased. Microchannels ablated under H_2SO_4 atmospheres display EOF rates that are much higher than those for any other microchannel studied, indicating that there are more negative charges present on the microchannels ablated in H_2SO_4. This may be due to the plasma created during the ablation process. In addition, it could be due to the inherent oxidative properties of H_2SO_4 with respect to PS which ultimately leads to chemical moieties possessing negative charges.

Polystyrene microchannels were also ablated under an NH_3 atmosphere and further characterized. As shown (Figure 41), we observed a negative EOF for pH 3, indicating that there are some positive moieties on the surface of the microchannel. At pH 5, the EOF is almost zero but reversed such that negative charges are predominant on the surface. At pH 7, the EOF is decreased compared to all of the other ablated surfaces but it is still present. This indicates that the microchannels display organic moieties with positive charges but that negative charges are also still present. As previously, this could potentially be due to air contamination of the stainless steel chamber during ablation.

As is noted, the surface characteristics of microchannels vary depending on the atmospheres under which the microchannels are fabricated. Studies underway include the determination of the EOF characteristics of ablated microchannels exposed to solution of various proteins to determine the extent of protein adsorption as well as the

study of such microchannels in a dynamic protein adsorption environment. We are also initiating experiments to use ellipsometry to evaluate dynamic protein adsorption on various polymer surfaces. This second technique will be used to validate the dynamic protein adsorption experiments made by EOF measurements.

Infra-red measurements have confirmed the incorporation of different, atmosphere controlled, functional groups into the ablated polymer surfaces (Figure 42).

Figure 42: Transmission infra-red spectroscopy shows how the presence of different atmospheres results in the incorporation of particular functional groups into the channel surface. Clockwise from top left: pristine spin coated polystyrene, NH₃, H₂SO₄ and N₂ atmospheres.

Low level enzyme interaction with PEG-ylated surfaces.

Low levels of protein adsorption to PEG with both horseradish peroxidase (Figure 43) and alkaline phosphatase (Figure 44) have been demonstrated at a variety of flowrates. It was found that the rate of adsorption is similar to that seen with other surfaces; it is the limiting coverage (P_{max}) which is reduced by PEG in this situation.
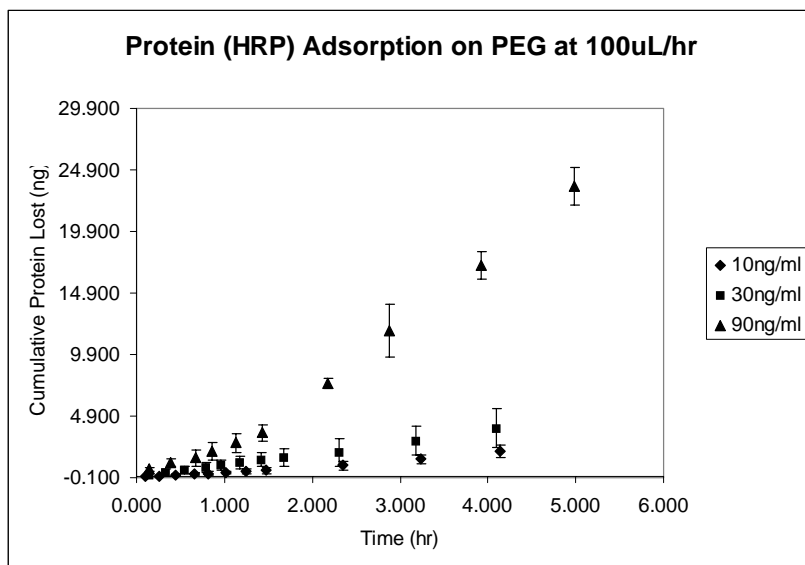
Figure 43: Horseradish peroxidase interaction with PEG at 100 μL/hr and a variety of concentrations.
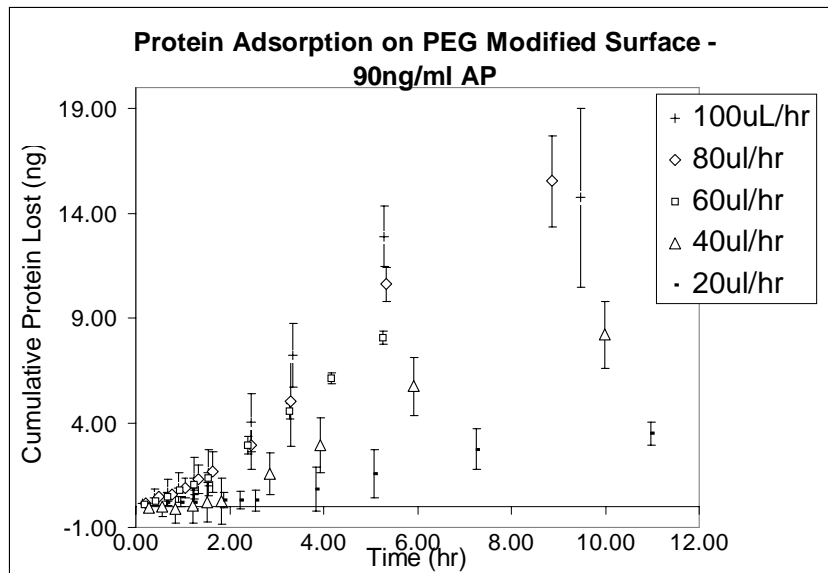
Figure 44: Alkaline phosphatase adsorption on PEG-modified silica surface at different flow rates.

Concept development for the advanced model of protein adsorption

The BioMEMS modeling work at Clemson University consisted of the theoretical development and implementation of a new mathematical model describing protein adsorption to functionalized surfaces for incorporation within a larger computational fluid dynamics software program.

The advanced model significantly advances the theoretical construct of protein adsorption, and provides a means to deal with the following issues:

1) non-Langmuir behaviour,

2) flow dependence of kinetic parameters, and

3) flow dependence of available number of binding sites.

59

To meet these requirements, it was necessary to incorporate three types of parametrically defined relationships into the developed model: i) surface energy and its distribution, ii) protein-surface interaction time and its distribution, and iii) characteristic proximity time of proteins within the flowing system.

The first relationship describes how the energy levels of the binding sites on a heterogeneous surface are distributed, which can be mathematically represented as linear combination of normally distributed functions. Different binding sites are assumed to have different energy levels and the probability for a protein molecule to encounter a binding site with a specific energy level can be readily derived from this assumption. The initial setup of the model employed a normal distribution for the reaction time, which has the disadvantage that the reaction time was distributed over a range of $-\infty < t < +\infty$, while a real reaction time must always be bounded as $0 < t < +\infty$. A chi-square distribution of the reaction time was therefore adopted and implemented in the model to provide this type of behaviour. The chi-square distribution is appropriate for this type of behaviour because it always provides a positive value for the reaction time, and when the chi parameter (υ) is large enough, the chi-square distribution is very similar to a normal distribution.
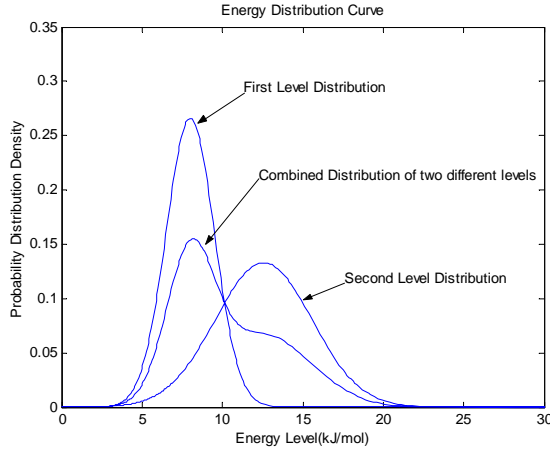
$$\gamma_s = (\delta G / \delta A)_{T,P,n}$$

$$g(e) = \frac{1}{e_\sigma} \exp\left[-\frac{1}{2}\left(\frac{e - e_\mu}{e_\sigma}\right)^2 \right] \quad in \quad which \quad e > 0$$

Figure 45: Site affinity distributions.

The second relationship represents the "interaction time distribution". Interaction time denotes the time span that a molecule spends over a binding site from its initial approach to being finally attached. This distribution arises from the fact that interaction time varies with the conformation and orientation with which the molecule approaches the binding sites. It is also a function of the binding potential of the binding site, which is assumed to exponentially influence the mean and variance of the interaction time distribution.
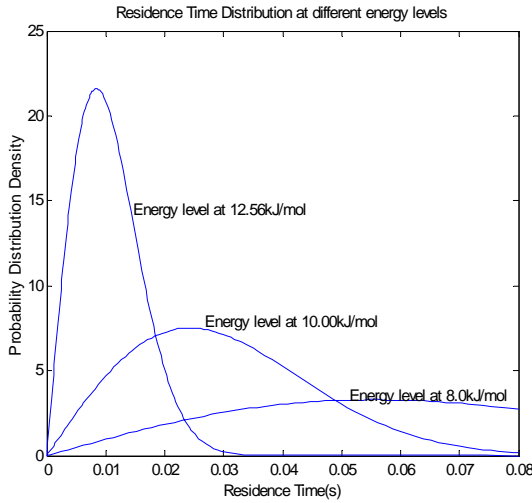
$$f(\tau) = \frac{1}{\tau_\sigma} \exp\left[-\frac{1}{2}\left(\frac{\tau - \tau_\mu}{\tau_\sigma}\right)^2 \right] \quad in \quad which \quad \tau > 0$$

$$\tau_\mu = A_\mu \cdot \exp(-E_i / RT)$$

$$\tau_\sigma = A_\sigma \cdot \exp(-E_i / RT)$$

$$f(\tau, E_i) = \frac{1}{A_\sigma \cdot \exp(-E_i / RT)} \exp\left[-\frac{1}{2}\left(\frac{\tau - A_\mu \cdot \exp(-E_i / RT)}{A_\sigma \cdot \exp(-E_i / RT)}\right)^2 \right]$$

Figure 46: The probability of adsorption as a function of residence time for different surface affinities.

With the above described probability density functions, the probability that one molecule, and hence the percentage of all molecules, becomes bound during a given time interval in a specific flowing system can be evaluated as a double integral, which we designate as the ITBE integral (Equation 4).

ITBE Integral:
$$P = \int_{E_{min}}^{E_{max}} \left[\int_{0}^{\tau_c} f(\tau, E_i) d\tau \right] g(E_i) dE_i \qquad \text{Equation 4}$$

The time interval that serves as the upper limit of the ITBE integral is a characteristic property of a specified system, which we designate as the characteristic proximity time; this represents the third relationship incorporated in the new model. This time interval is defined as the length of time for a molecule to approach and then leave a binding site without binding, which is dependent on the size of the molecule and the local flow velocity.

$$V_{z,max} = 2\overline{V_z} = \frac{(p_0 - p_L)R^2}{4\mu L} \qquad \tau_c = \frac{\varphi}{V_z} = \frac{\varphi}{2\overline{V_z}[1 - (\frac{r}{R})^2]} = \frac{\varphi}{2\overline{V_z}[1 - (\frac{R - \varphi/2}{R})^2]}$$

$$V_z = \frac{(p_0 - p_l)R^2}{4\mu L}[1 - (\frac{r}{R})^2] \qquad = \frac{\varphi}{2\overline{V_z}\frac{\varphi(4R - \varphi)}{4R^2}} = \frac{2R^2}{\overline{V_z}(4R - \varphi)} \approx \frac{R}{2\overline{V_z}}$$

This relationship provides an essential component for the new model in that it enables the flow rate dependence of the kinetic parameters and the available binding sites to be accounted for.

From the developed analytical model, the adsorption kinetics of protein molecules in a microfluidics system under flow conditions can be calculated as the quotient of the ITBE integral over the characteristic proximity time of the system. The parameter values of the analytical model can then be solved by comparison with experimental data for protein adsorption from microfluidics flow experiments, and these values used for the characterization and optimization of a given protein solution-microfluidic flow system.

Model Calibration Using Automated Intrinsic Parameter Extraction

Approaches to Extracting Kinetic Constants From Binding Data
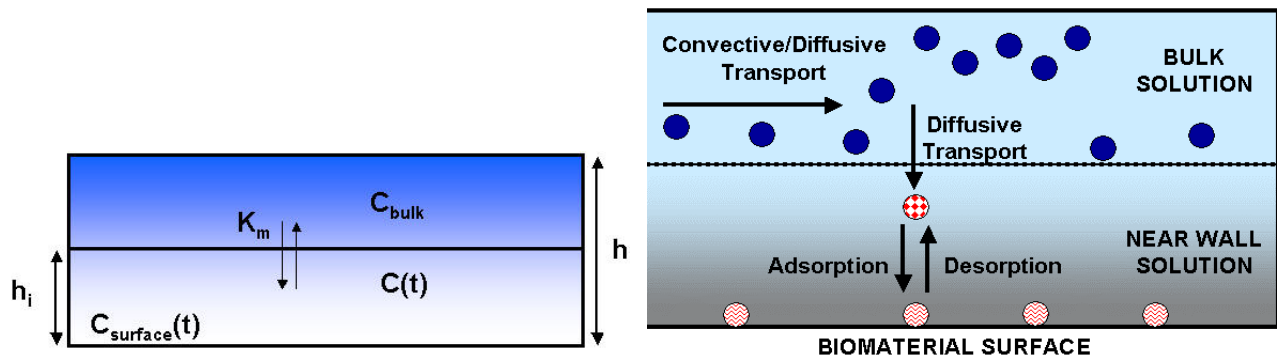
Figure 47:   (a) Simplified 2-compartment model (b) Fluidics/Transport resolved adsorption model.

Traditionally, two different methods have been used to extract kinetics from adsorption data. The simplest approach involves neglecting non-ideal (convective-diffusive) effects by assuming well-mixed protein in contact with an idealized surface. Coupled with psuedo-second order kinetics, this leads to the classical analytical expression for the Langmuir adsorption isotherm. This expression can be regression-fitted to experimental data to calculate the kinetic constants. However, this can lead to large errors in situations where transport is the rate-limiting step. In an incrementally better approach (favored by

many today), the convective-diffusive transport of the protein to the surface under fully developed laminar flow conditions, coupled with surface adsorption are described using a lumped-parameter (so-called two compartment) model (Figure 47a). While this is better than the well-mixed approach, this still introduces several drawbacks. The most significant of these are: (a) introduction of an additional fitting parameter k_m (transport coefficient) which can introduce errors in the extracted values (b) non-applicability to flow situations other than fully developed (idealized situations). *In summary both methods do not yield the true or intrinsic kinetics but rather a value that is influenced partly by the conditions of the experiment.*

In contrast, the approach we have chosen is to use Computational Fluid Dynamics (CFD) to analyze the protein/surface interactions. CFD provides a convenient methodology for characterizing and studying convective-diffusive transport and adsorption kinetics, simultaneously within a single framework (Figure 47b). The model explicitly considers fluidic (convective-diffusive) transport of protein to the surface coupled with a model of protein adsorption on a substrate. It considers a monolayer formed by a reversible adsorption process, which yields a Langmuir type adsorption isotherm. The salient features of this approach are:

(a) capable of ab-initio accounting for convection, diffusion and electromigration of multiple protein species towards a biomaterial surface in any arbitrary three-dimensional volume;

(b) accounts for finite-rate binding kinetics, with the reversible adsorption process modeled as a second-order reaction and the desorption process modeled as a first-order reaction; and

(c) allows for simulation of localized variations in surface composition through variations in the density of binding sites and/or variations in the binding rate constants at different locations along the surface.

Dependence of Extracted Kinetic Constants on Mass Transport

Mass transport limitations are characterized in the system by comparing the rates of diffusive transport to the rate of reactive uptake. This is usually described by a dimensionless number known as the Damkohler number, which is a ratio of the reaction rate to the diffusion rate expressed mathematically below (Equation 5).

$$Da = \frac{k_a P_{\mathbf{max}}}{(D / \delta)}$$
Equation 5

where k_a is the forward reaction rate coefficient, P_{max} is the concentration of receptors in the system, D is the diffusion coefficient of the reactant in solution, and δ is a characteristic length scale over which the surface reaction is taking place. This can be termed a static Damkohler number. This type of a formulation of the Damkohler number does not take into account convective transport effects that may serve to change the mass transport conditions, thereby altering the Damkohler number.

Another formulation of the Damkohler number is given by Edwards (1999) and accounts for the added influence of convection in the system (Equation 6),

$$Da = \left(\frac{K_a P_{\mathbf{max}}}{U} \right) \left(\frac{UL}{D} \right)^{\frac{2}{3}} \left(\frac{d}{L} \right)^{\frac{1}{3}}$$

Equation 6

where, in addition to the parameters described earlier, U is a characteristic velocity of the liquid phase, L is the length of the reaction patch, and d is the height of the column of fluid above the reactive patch. This formulation has been used to analyze how mass transport limitations can affect the output from common biosensors. The analysis below is given for the system of alkaline phosphatase binding to PEEK. The diffusion coefficient of alkaline phosphatase for this system is 2.0×10^{-11} m^2/sec. The values for k_a and P_{max} are taken as the fitted values. The characteristic length scale is taken to be 1 micron, and the value of U is taken as the centerline velocity of the fluid in the 65 micron diameter capillary used in the experiments. The values for the static and dynamic Damkohler numbers, as well as the Reynolds number for the system, are given below in Table 2.

Table 2: Static and Dynamic Damkohler numbers, and the Reynolds number for alkaline phosphatase binding to PEEK data.

Q (μL/hr)	Da$_{static}$	Da$_{dynamic}$	Re
20	0.01	0.144	0.109
40	0.022	0.248	0.218
60	0.102	1.01	0.326
100	0.18	1.50	0.544

Damkohler numbers much greater than one indicate a mass transport limitation. The values in Table 1 above are on the order of 1, which indicates that, at worst, the system is mass transport influenced but not mass transport limited. An analysis of the characteristic time scales for diffusion and reaction shows that the characteristic times for diffusion are on the order of seconds, while the characteristic time for the reaction is on

the order of minutes. This means that the reaction is occurring slower than the diffusion can occur.

The objective of this section is to demonstrate that the current method of extracting kinetic coefficients using the output of CFD simulations is independent of the transport situation. Indeed, this fluidics-resolved method can extract the intrinsic kinetics from experimental data under variable mass transport limitation conditions. Figure 48 shows three sets of experimental data for the system of acetazolamide binding to Carbonic Anhydrase-II in a BIACORE biosensor (Data courtesy of David Myszka of the University of Utah, Stanford SIMBIOSYS Project). The experiments were performed under three types of mass transport conditions: kinetically limited, mass transport influenced, and mass transport limited. The binding curves for acetazolamide were taken at five inlet concentrations for each mass transport condition, and the flowrate for the system was set at 100 μL/min. Fitting was performed on each data set, and the results are also shown in Figure 48. The different mass transport conditions were obtained by varying the surface concentration of the Carbonic Anhydrase-II immobilized on the sensor surface. This is the equivalent of varying P_{max} in equations 5 and 6. It is not practically feasible to generate very high Da in this system by this means, hence we substituted model generated data for this case.
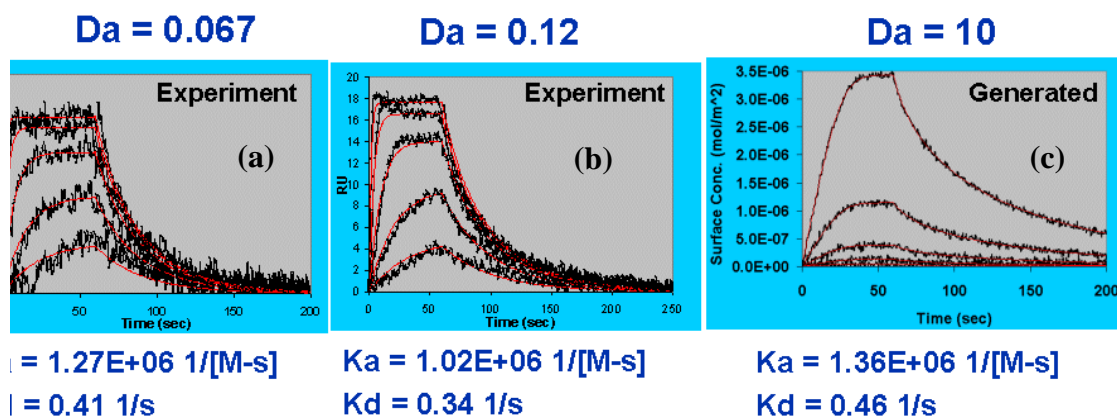
Figure 48: Illustration of the fitting of kinetic data under variable mass transport conditions. Shown are the cases for (a) Kinetically limited, (b) Mass transport influenced, and (c) Mass transport limited. Below each image are the fitted values of the binding and debinding constant.

The fluidics-resolved extraction procedure, as practiced in this instance, is able to deconvolve the transport effects from the kinetics and minimal variation is seen in the calculated coefficients. In contrast, simpler (two-compartment type) models will use an extra adjustable parameter km and this can introduce errors in the extracted coefficient values. Thus, true intrinsic kinetic coefficients can be extracted accurately over a wide range of transport conditions.

Dependence of Fitting on Flowrate for Standard Data Sets

The objective of this section is to demonstrate that the current method of extracting kinetic coefficients using the output of CFD simulations can extract the intrinsic kinetics from experimental data under variable flowrate conditions. Figure 49 shows four sets of experimental data for the system of acetazolamide binding to Carbonic Anhydrase-II in a BIACORE biosensor (Data courtesy of David Myszka of the University of Utah). The experiments were performed at four flowrates of 12, 25, 50, and 100 μL/min. The

binding curves for acetazolamide were taken at six inlet concentrations for each flow rate, with the mass transport conditions being held constant at a Damkohler number of 0.12. Fitting was performed on each data set, and the results are indicated in Figure 49. Figure 50 shows how the fitted values of k_a, k_d, and P_{max} vary with flowrate. This figure shows that under variable flowrate conditions the fitted values of the kinetic coefficients are constant to within a few percent.
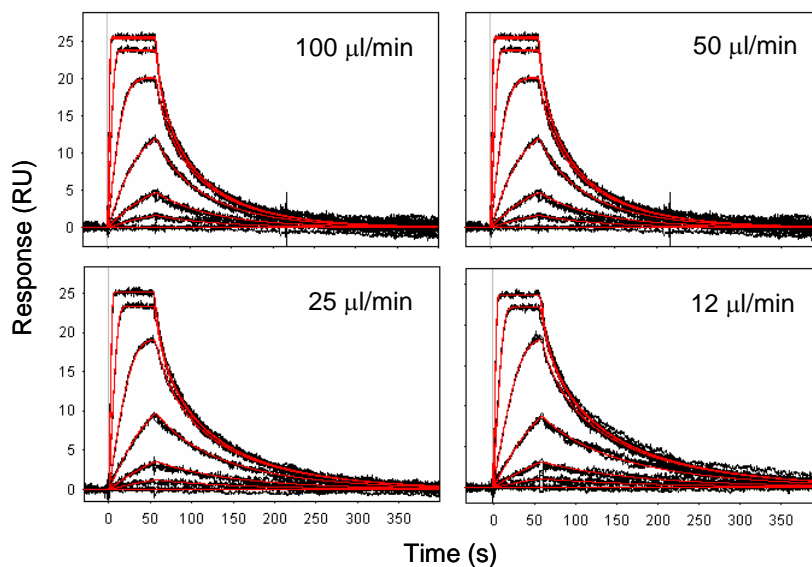
Figure 49: Experimental data for the system of acetazolamide binding to Carbonic Anhydrase-II at varying flowrates.
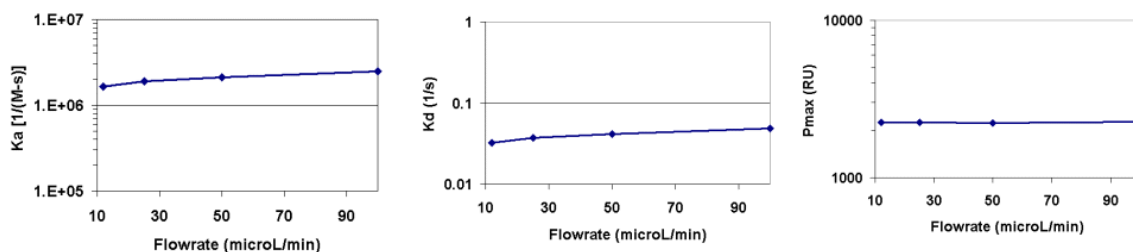
Figure 50: Variation of the fitting parameters with flowrate. (a) Variation of k_a with flowrate, (b) Variation of k_d with flowrate, and (c) Variation of P_{max} with flowrate.

Least Squares Fitting Procedure

Extraction of kinetic constants from data was performed using the biochemistry module in CFD-ACE+. This module was updated to include a more general biochemistry solver, allowing the user to simultaneously simulate multiple complex biochemical mechanisms. The second upgrade was the addition of a biochemical database, giving the user the ability to store chemical species data and reaction mechanisms for use in other simulations or to be shared in a library of compounds and reactions.

The least squares fitting procedure was rewritten during the grant period as well to take advantage of the updates to the biochemistry module. There are three main updates to the least squares fitting procedure used previously. The first enhancement was the added flexibility that comes with a tight integration with the biochemistry database. This flexibility is first manifest in the graphical user interface (GUI), which is created dynamically from the information contained in the property and reaction database (Figure 51). The GUI gives the user the choice of which kinetic constants will be used as fitting parameters and which will be held constant. Another important feature of the GUI is the ability to control which species concentrations will be used in comparison with the experimental data. This is an important feature especially in a complex system where only a few species are being sensed to generate the experimental signal.
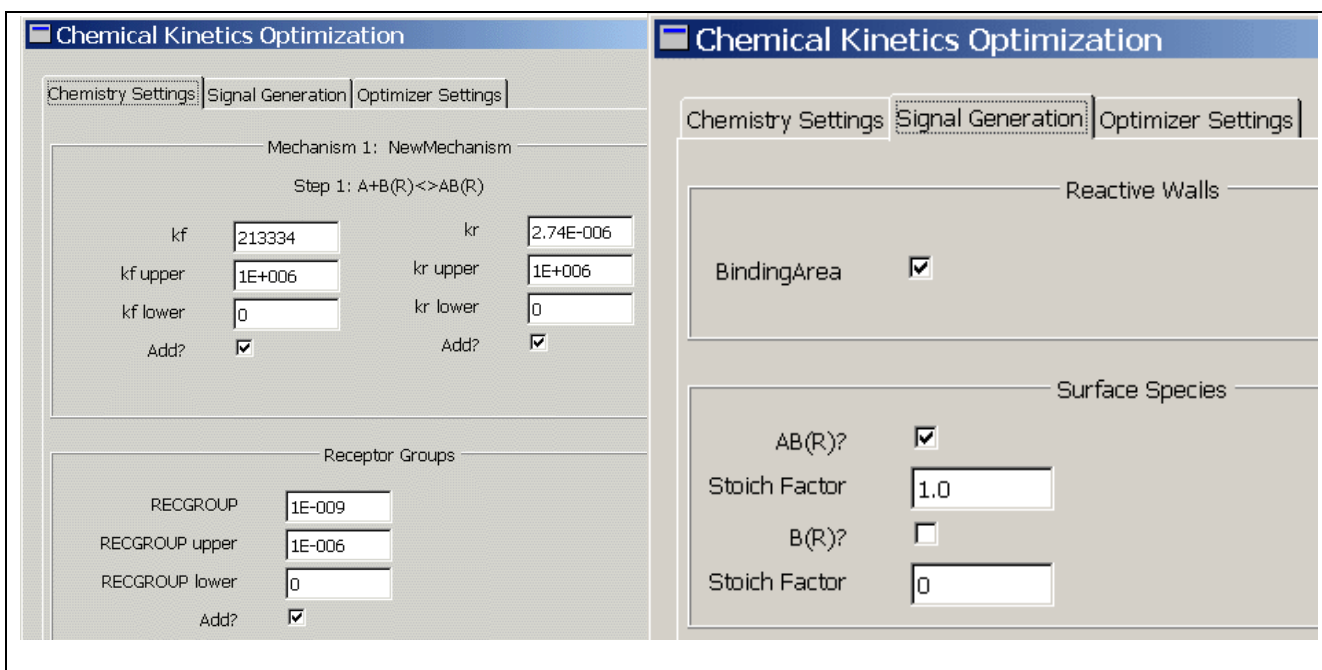
Figure 51: Illustration of the GUI for the improved least squares fitting script. The figures illustrate how the fitting in this report was performed using Langmuir type binding chemistry.

The second enhancement was the ability to simultaneously fit multiple inlet concentrations in the same simulation. All of the manipulations of the simulation output and the database entries are handled by the fitting script, allowing for a painless method of fitting multiple concentration data in one simulation. The third and final enhancement was the automatic generation of "goodness of fit" information as well as an assessment of fitted parameter uniqueness. The goodness of fit assessments output to the user contain standard information, such as the confidence interval of the fitted value, as well as statistical tests performed on the residuals to detect the presence of outliers and common trends in the residuals indicating a lack of fit. The uniqueness of the fitted values is determined by looking at the eigenvalues of the data correlation matrix. From statistical theory, it is known that the eigenvalues of the correlation matrix should sum to the number of degrees of freedom in the system. In a well fit system, all of the eigenvalues

should be close to a value of 1.0, indicating that each fitted parameter is contributing equally to the fit. If an eigenvalue falls below a cutoff value, then it is not contributing to the overall fit indicating that the system is over parameterized.

Parameterization of the Baseline Model

The automated data extraction methodology was applied to data on protein adsorption, specifically alkaline phosphatase (AP) binding to a PEEK capillary system. The PEEK capillary has an inner diameter of 65 μm with an overall length of 10 cm. Flowrate for the experiments was set at 100 μL/hr, and the inlet concentration of AP was varied between 30, 60, and 90 ng/mL. Binding constants were extracted from the data using a least squares parameter fitting procedure that compares output from a transient CFD/Biochemistry simulation using ACE+ with experimental data to produce the best fit. This procedure uses a variant of the Gauss-Newton method to minimize the squared error between the experimental data and the simulated output. A Langmuir adsorption model is assumed in the ACE+ biochemistry module, and the binding (k_a) and debinding (k_d) constants are used as fitting parameters.

Each of the three different inlet concentrations were fit individually, and the plots are shown below in Figures 52 through 54. The density of available binding sites is held constant at the experimental value of 2.67 nanomoles/m^2 in these figures. The fitted values of k_a and k_d are similar in magnitude, however their values change for the individual fits. The k_a values range from 5.5×10^5 (M-s)$^{-1}$ to 5.9×10^5 (M-s)$^{-1}$, while the values of k_d range from 1.0×10^{-7} 1/s to 9.52×10^{-6} 1/s. A more robust approach uses all

three data sets simultaneously. Furthermore, surface receptor density is a very difficult variable to experimentally isolate and is often treated as another unknown. Indeed this is the approach followed by exponents of the SPR-based, biokinetics extraction method.

Figure 55 shows the results from a "global fitting": involving multiple data sets and an unknown, fittable receptor density. The fitted values are $k_a = 5.93 \times 10^5$ $(M\text{-}s)^{-1}$ and $k_d = 5.4 \times 10^{-6}$ 1/s are in good agreement with the single datasets. The fitted value of the surface receptor density was 4.27 nanomoles/m^2, which compares favorably with the experimental value, validating the method of calculation. This suggests that the observed behaviour can be well correlated with a Langmuir adsorption isotherm.

The global fitting is challenging to perform mainly due to small data set size and a general need for steady state data. The problems with the small data set size manifested themselves most strongly in the "outlier" points. Two points in particular had an impact on the convergence of the fitting algorithm in this initial fitting exercise, and they were points that lie at approximately 10,000 seconds and fall on the 30 and 60 ng/mL curves. These points did not follow the trend of the data and also did not lie on the fitted curves. If the data set were larger, the effect of the outliers would be less significant since each data point has the same statistical weighting. The second problem, lack of steady state data, manifested itself in the high k_a value. Since the fitting program did not have steady state data to anchor the computed equilibrium values, the algorithm took the "path of least resistance" and increased k_a and decreased k_d to get the best fit possible. The values of k_a and k_d reported here from the global fitting are not being reported as the

physically correct k_a and k_d due to the above problems. They did however give a better idea of what was required from the experiments in order to use the computational tools more efficiently to extract intrinsic kinetic constants.
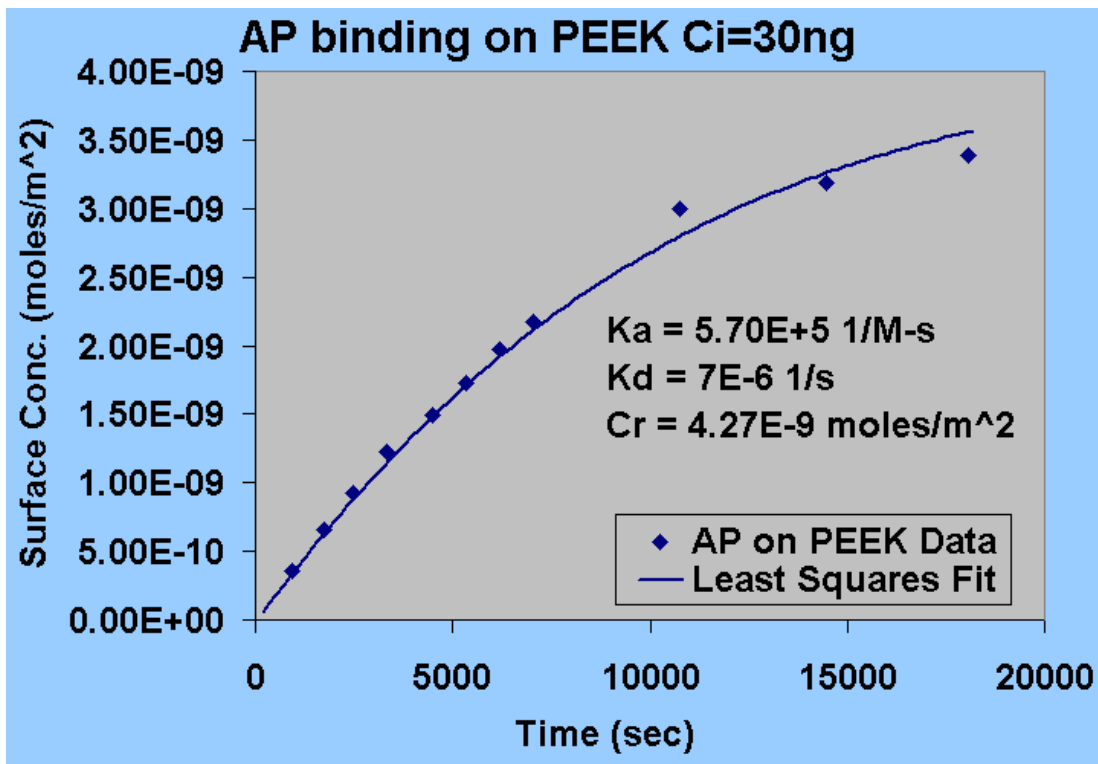
Figure 52: Least squares fit of AP binding to a PEEK capillary with an inlet concentration of 30 ng/mL.
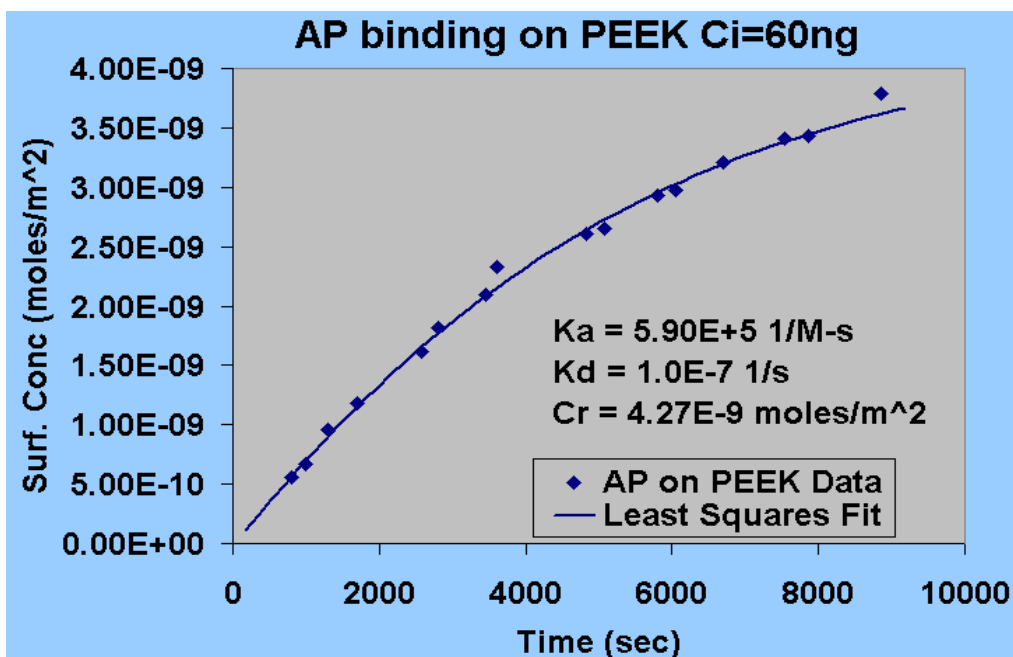
Figure 53: Least squares fit of AP binding to a PEEK capillary with an inlet concentration of 60 ng/mL.
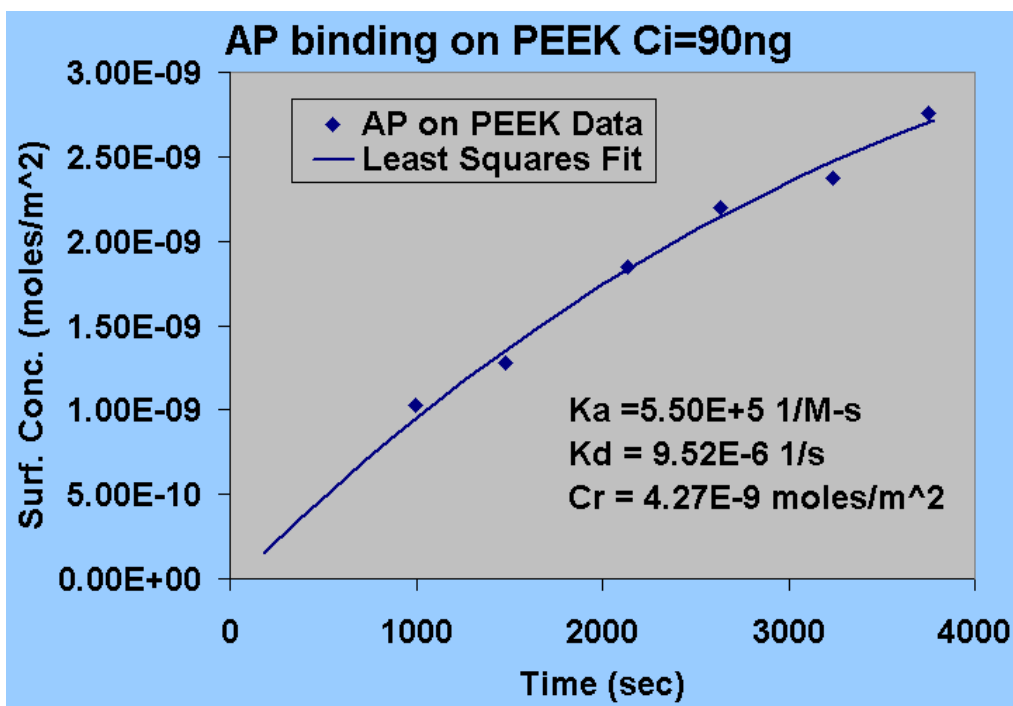
Figure 54: Least squares fit of AP binding to a PEEK capillary with an inlet concentration of 90 ng/mL.
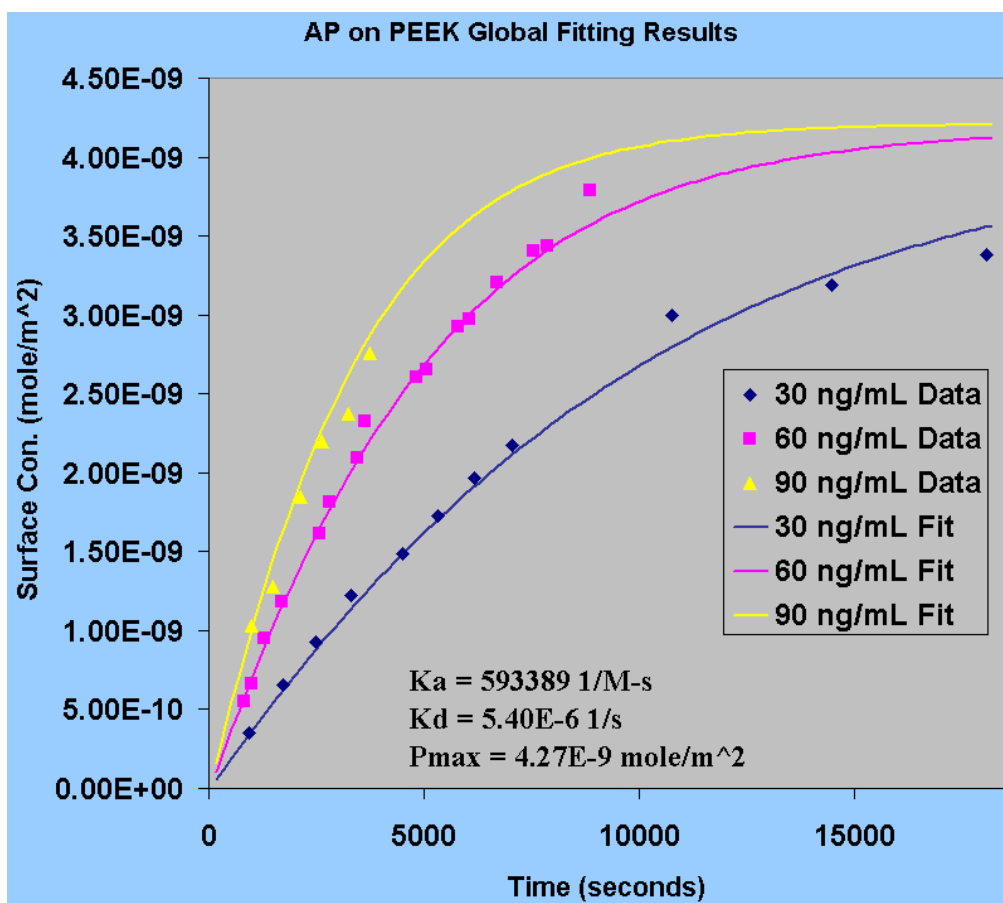
Figure 55: 3-Parameter global least squares fit of AP binding to a PEEK capillary with all three inlet concentrations.

The 3-parameter global fitting data was also validated using a system of carboxybenzyl sulfonamide binding to anhydrase measured using the BIACORE SPR instrument (Data provided courtesy of David Myzska of the University of Utah). Rates of adsorption and desorption were extracted using CLAMP with the mass transport limitation turned on. Table 3 gives the values of k_a and k_d as a comparison. These values are consistent with the values given by CLAMP (differences attributable to the differences in accounting for flow and mass transport effects – exact in the CFD-ACE+ representation).

Table 3: Comparison of ACE+ fitting with CLAMP.

	k_a (1/M-s)	k_d (1/s)
CLAMP	50603	0.0377
ACE+ Fitting	57085	0.0455

Alkaline Phosphatase (AP) on Teflon

CFD-ACE+ model predictions along with experimental data for the AP/Teflon system are shown in Figure 56. Unlike the PEEK capillary, the model is less successfully able to predict the overall binding behaviour. The forward binding constant of $3x10^5$ $[M-s]^{-1}$ is smaller than reported on PEEK. Again very low desorption rates $5x10^{-9}[s]^{-1}$ are predicted.
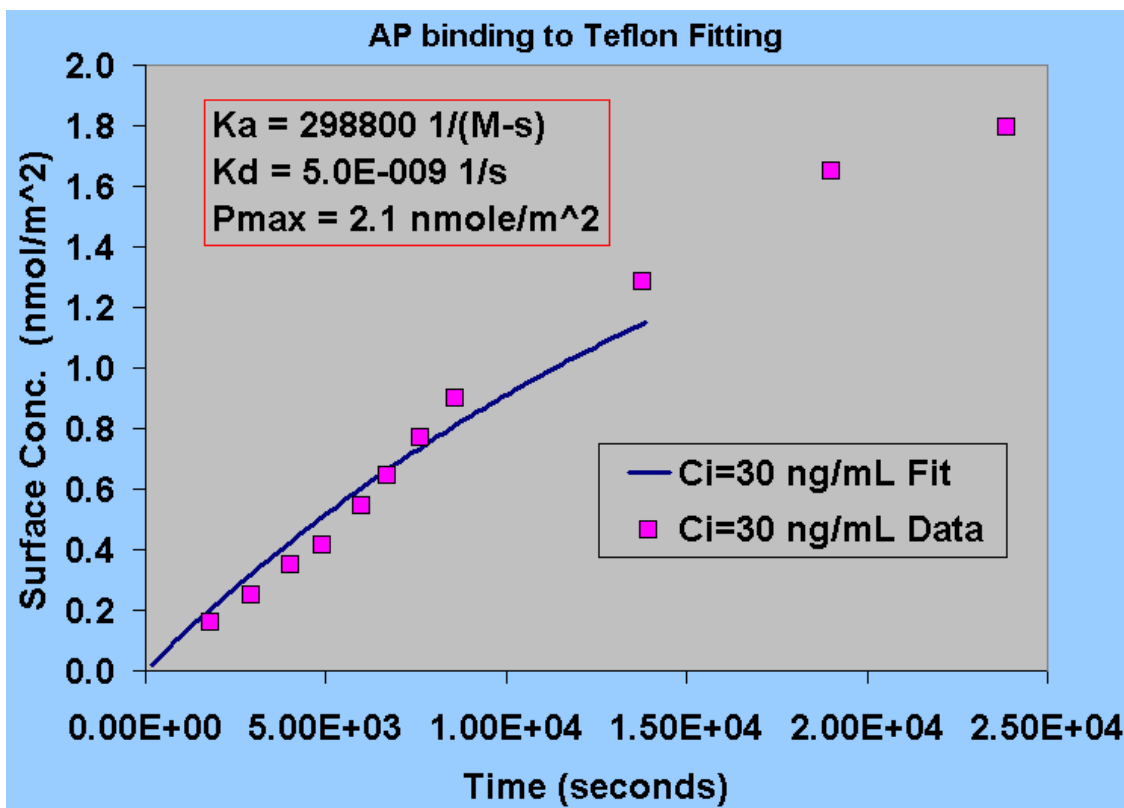
Figure 56: Alkaline Phosphatase binding to Teflon. Baseline Model vs. Experiment.

Unlike AP on PEEK, evidence of complex behaviour (sigmoidal) is readily seen, which cannot be explained by the baseline Langmuir adsorption model. One possible explanation is "autocatalytic" behaviour whereby the protein that goes down initially is able to alter favorably the energetics/affinity of nearby open sites. This results in a net increase in the adsorptive behaviour as coverage progresses. This experiment and modeling exercise clearly highlights the need for an advanced description of protein adsorption, including modeling of distribution of site energetics.

Glucose Oxidase (GO) on PEEK

Fitted adsorption curves along with experimental data for the GO/PEEK system are shown in Figure 57. Early time adsorption is predicted reasonably by the baseline model. The forward binding constant of 1.6×10^4 [M-s]$^{-1}$ is considerably lower than that of AP.
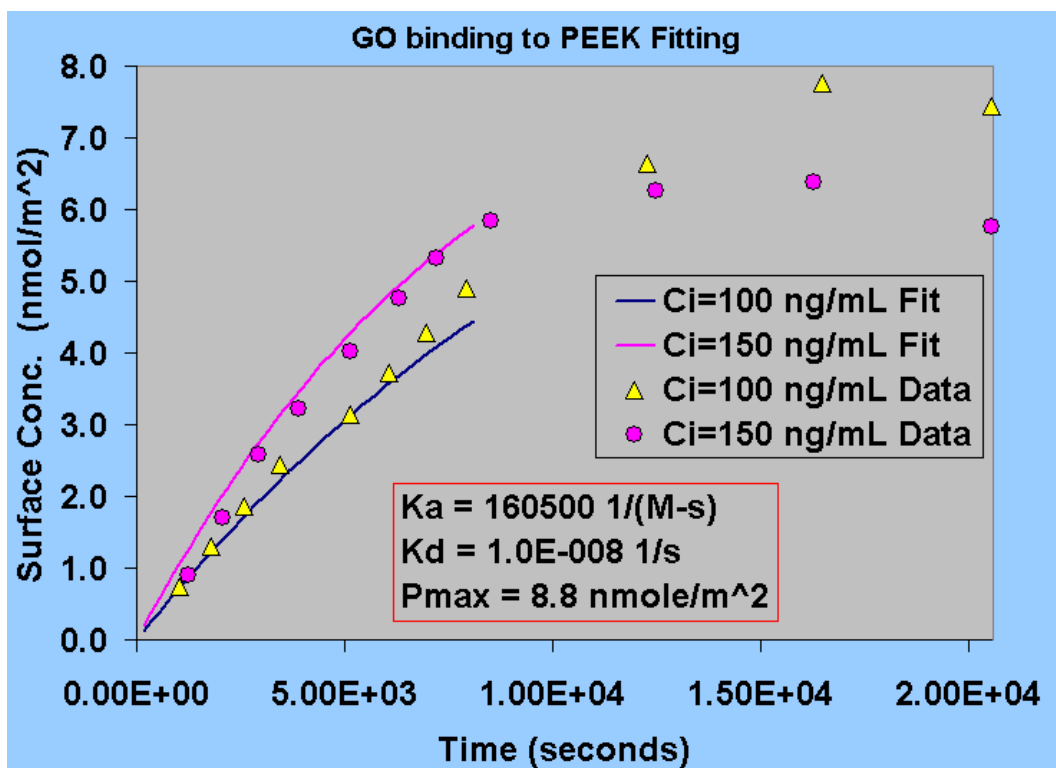
Figure 57: Glucose Oxidase binding to PEEK. Baseline Model vs. Experiment.

Again it is indicated that protein once adsorbed, desorbs very slowly. However, complex decaying behaviour is seen after a period of about 10000 seconds (3 hrs+), even in the continued presence of protein. The baseline model cannot account for this behaviour which once again underscores the need for a more complex binding model.

Glucose Oxidase (GO) on Teflon

The GO/Teflon system was analyzed and the model as well as experimental data are shown in Figure 58. In a behaviour very similar to GO adsorption on PEEK, the short range adsorptive behaviour was correlated well by the baseline model. The forward
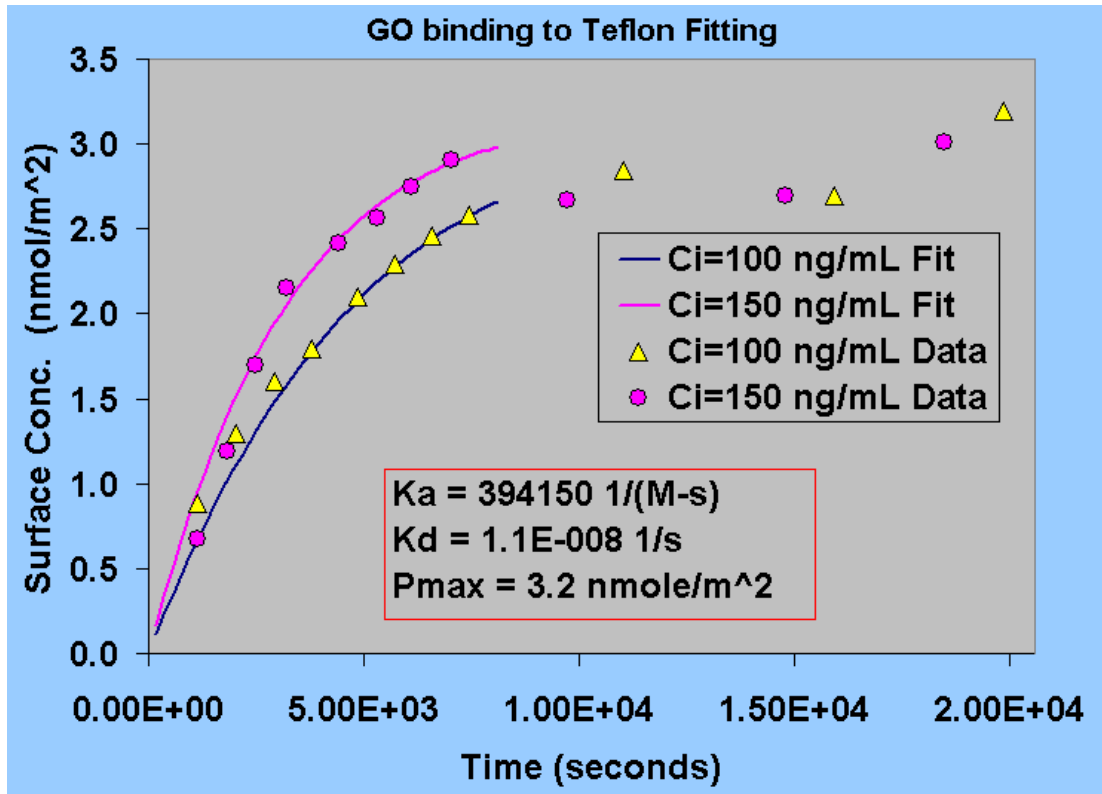
Figure 58: Glucose Oxidase binding to Teflon. Baseline Model vs. Experiment.

binding constant of 3.9×10^4 [M-s]$^{-1}$ shows larger affinity of GO to Teflon than PEEK. As before, desorption rates are very small (1.1×10^{-8} [s]$^{-1}$). Analogous to the GO/PEEK

79

system, GO binding to Teflon also displays anomalous behaviour at timescales larger than 3hrs.

Summary of Extraction Simulations

Tables 4 and 5 are summaries of the data fitting presented above. Table 4 shows that AP binds equally well to PEEK and Teflon, with low debinding rates for both materials. The modeling reveals a higher density of binding sites on PEEK surfaces relative to Teflon surfaces by a factor of 2. GO shows a higher affinity for the Teflon surface as opposed to the PEEK surface. The debinding rates are low for both materials. The density of potential GO binding sites are nearly a factor of 3 higher for PEEK than on the Teflon surface.

Table 4: Alkaline Phosphatase Fitting Summary

	PEEK	Teflon
K_a (M-s)$^{-1}$	5.9×10^5	5.0×10^5
K_d (1/s)	5.0×10^{-6}	5.0×10^{-9}
Pmax (nmole/m^2)	4.27	2.1

Table 5: Glucose Oxidase Fitting Summary

	PEEK	Teflon
K_a (M-s)$^{-1}$	1.6×10^5	3.9×10^5
K_d (1/s)	1.0×10^{-8}	1.1×10^{-8}
Pmax (nmole/m^2)	8.8	3.2

Experimental data for Glucose Oxidase (GO) (molecular weight of 160,000 Da) binding to a PEG coated surface was provided to CFDRC for least squares analysis. The experimental setup consists of a capillary of 15.0 cm in length, with an inner diameter of 50 μm. A 100 ng/mL solution of GO is pumped through the capillary at the rate of 100 μL/hr. Data are taken at regular intervals for approximately 5 hours while the GO is allowed to bind on the PEG coated surface. The experimental data along with the fit are shown below in Figure 59.
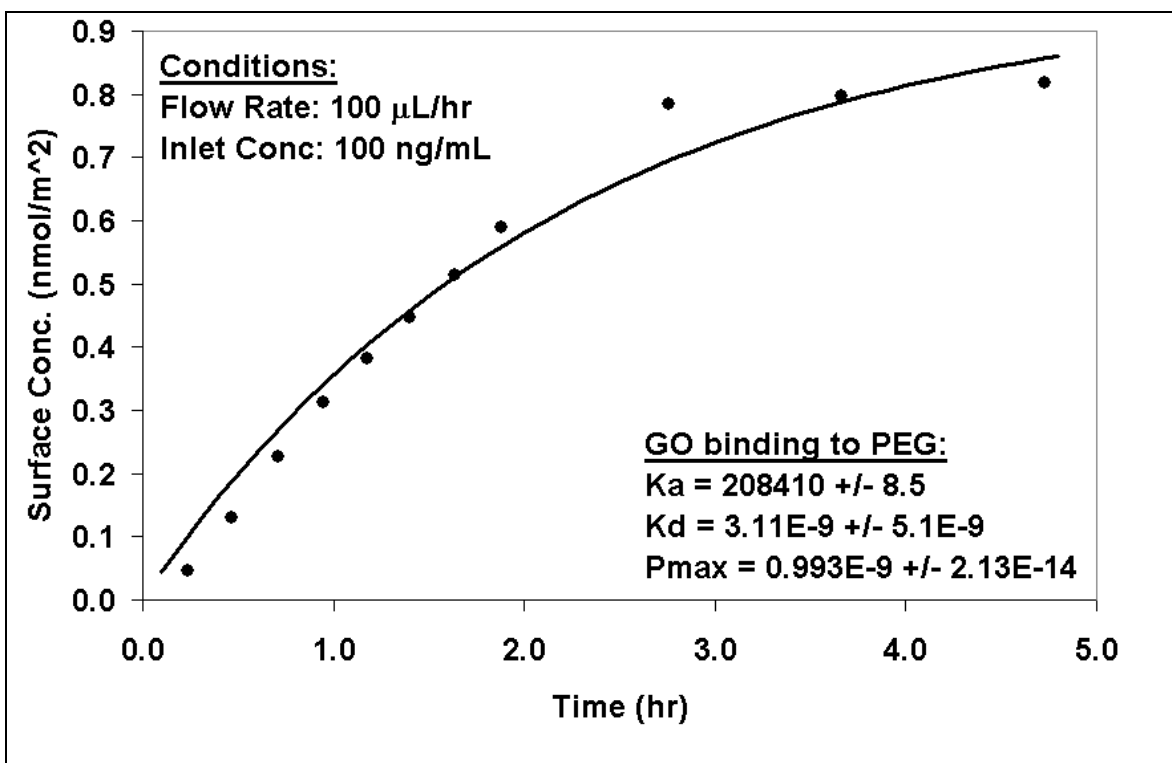
Figure 59: Glucose oxidase binding to a PEG coated capillary. The experimental data points are shown as closed circles, and the least squares fit is shown as the solid curve. The units of Ka are (M-s)$^{-1}$, Kd has the units of s^{-1}, and Pmax has the units of mol/m^2.

An analysis of the mass transport limitations of this system indicates that the system is in the kinetically limited regime with a static Damkohler number of 0.01 and a dynamic Dankohler number, computed using the method of Edwards (1999), of 0.074. Table 6 below shows a comparison of this fit with the previous fits on the PEEK and Teflon surfaces. All three data sets were collected at a flowrate of 100 µL/hr and a concentration of 100 ng/mL, however both the PEEK and Teflon data were collected using 65 µm I.D. capillaries and the polyethyleneglysol PEG data was collected using a 50 µm I.D. capillary.

Table 6: Glucose Oxidase Binding to three surfaces

	PEEK	Teflon	PEG
K_a (M-s)$^{-1}$	1.6×10^5	3.9×10^5	2.1×10^5
K_d (1/s)	1.0×10^{-8}	1.1×10^{-8}	3.1×10^{-9}
Pmax (nmole/m^2)	8.8	3.2	0.993

Table 6 shows that the binding and debinding constants are similar for all three materials, the main difference is the density of available binding sites. PEG has one third the sites of Teflon, and almost a factor of ten fewer sites when compared to PEEK. The value of K_a for GO binding to PEG seems a bit high since it is expected that a protein will not bind to PEG at the same rate as to the other two surfaces. However, a comparison of the binding curves in Figure 60 shows that the shape of the GO binding curve is essentially the same for the three surfaces, indicating that all three bind at similar rates. Therefore, while the binding and debinding rates may be similar for all three materials, significantly less protein can be absorbed by a PEG surface, in line with conventional wisdom for PEG coated surfaces.
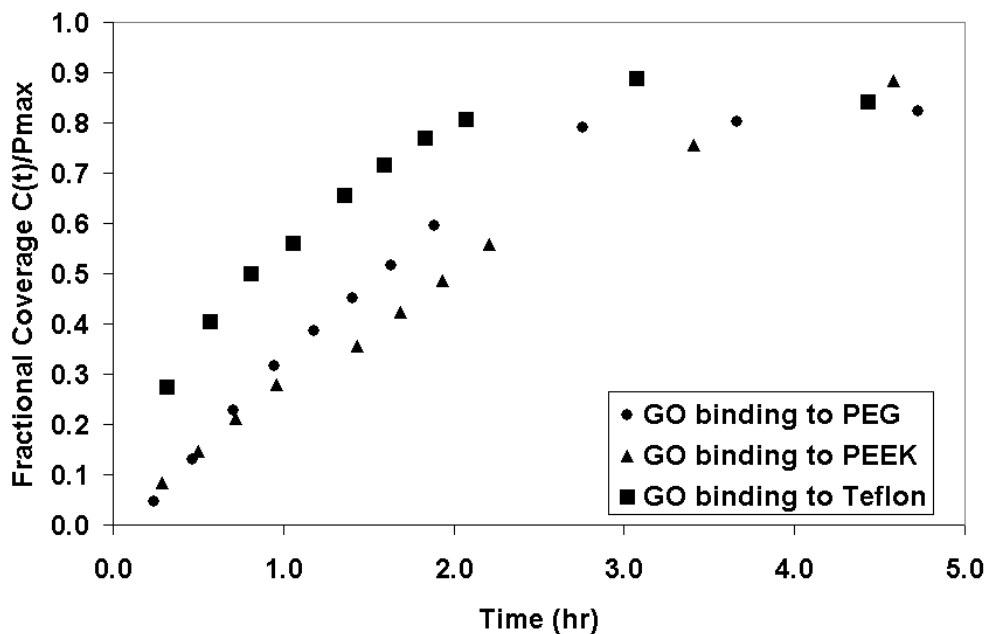
Figure 60: Plot showing GO binding to PEG, Teflon, and PEEK. The plot shows the fractional coverage $C(t)/P_{max}$ as a function of time. This allows for a comparison of the base binding rates.

A goodness of fit assessment was performed on the data in Figure 60 using the new least squares fitting script. The statistical analysis of the fit indicated that there were no outliers in the data, and that there are no significant trends in the residuals. An analysis of the uniqueness of the fitted parameters indicates that there is a possible parameter redundancy. The eigenvalues of the correlation matrix are 2.77, 0.22, and 5.0×10^{-5}. Optimally, all of the eigenvalues would be close to a value of one, since their sum is the number of degrees of freedom in the system. However in this case the eigenvalues indicate that two of the parameters are carrying the majority of the degrees of freedom (K_a and P_{max}), and one of the fitting parameters (K_d) is redundant.

Discussion of Fitting Parameter Redundancy

The fitted values for GO binding to PEG shown in Table 6 should be viewed with the understanding that they do not uniquely define the predicted curve. This means the predicted curve is not uniquely determined by the (K_a, K_d, P_{max}) set of values. So there are multiple sets of values that will give exactly the same binding curve. This means the system is over parameterized and one of the fitting parameters is redundant. The main causes of parameter redundancy when fitting a Langmuir model to binding data are:

(1) Sparse data sets: More data points help to increase the overall statistical performance of the fitting and help to reduce parameter redundancy.

(2) Lack of steady state data: This is the main contributor to parameter redundancy. The lack of steady state data for a single concentration will cause the degeneration of the Langmuir binding model to a two parameter model.

(3) No Multiple Concentration Data: Data taken at multiple inlet concentrations statistically increases the need for more degrees of freedom to fit the data, eliminating parameter redundancy. Multiple concentration data also decreases the need for steady state data, but does not eliminate it entirely.

(4) No Debinding data: The optimal situation for fitting a Langmuir binding model is to decouple the effect of binding and debinding. This is accomplished experimentally by pumping a solution containing protein for binding until steady state is reached. Immediately afterward a solution containing only buffer is pumped in and any bound protein is allowed to debind. The reason for the two step protocol is to decouple the effects of binding from debinding.

Advanced Model Development

Development and Testing of Advanced Model

The baseline protein adsorption model tested so far, postulates a simple, uniform bi-molecular reaction between the protein and the surface sites. It does not allow for the inclusion of surface variations (site energetics), flow effects etc., which have been found to be significant in determining the levels of protein adsorption. In our proposed advanced model, we seek to develop a phenomenological framework for the inclusion of both the distribution of residence times of a protein in the vicinity of a potential binding site and the distribution of binding site energy. This enables us, for example, to quantify effects of flow on adsorption and account for differences in surface energetics.

We start with the postulated form of the surface binding rate (Eq. 7), (details omitted for brevity), which explicitly represents both binding site energetics and protein residence or "proximity" times near a binding site. The different terms are explained as follows: A fraction of binding sites $f(E_i)$ carries energy E_i with the constraint that $\Sigma_I f(E_i) = 1$. The probability of a protein binding to a site of energy E_i is represented by $P(E_i)$, where $P(E_i)$ is small for small E_i and approaches a value of 1 for large E_i. The residence time distribution function $R(\tau,t)$ is the distribution of residence times for a protein near a binding site. $R(\tau,t)$ evolves with time, t, according to the local transport of proteins near a binding site. $P(\tau)$ is the probability a protein will bind as a function of residence time. Small residence times result in small $P(\tau)$, whereas for large residence times $P(\tau)$ approaches a value of 1.

Near Surface
Concentration

Receptor
Site
Density

Fraction of total
sites with energy
E

Residence time
Distribution

$$\dot{B}_i = K_a P_{\max} C_s(t) P(E_i)[f(E_i) - \theta_i]\int_0^t R(\tau,t)P(\tau)d\tau$$

Adsorption
Constant

Probability of
adsorption due
to receptor site
energy

Site Coverage

Residence time
Binding
Probability

Equation 7

The desorption rate (Eq. 7) is postulated to be dependent on site energy, with low energy sites being more likely to desorb. Conversely, high energy sites are assumed to desorb at a lower rate. No dependence on residence times is expected as this is a pure surface phenomenon.

$$\dot{D}_i = K_d P_{\max}(1 - P(E_i))\theta_i \qquad \text{Equation 8}$$

The evolution equation for the coverage of receptor sites is obtained by dividing the binding rate by the total number of surface sites $P_{\max}$:

$$\frac{d\theta_i}{dt} = K_a C_s P(E_i)[f(E_i) - \theta_i]\int_0^t R(\tau,t)P(\tau)d\tau - K_d(1 - P(E_i))\theta_i \quad \text{Equation 9}$$

It is useful to rewrite the above equations in the familiar Langmuir form.

$$K_a(\tau, E_i) = K_a P(E_i)\int_0^t R(\tau,t)P(\tau)d\tau \qquad \text{Equation 10}$$

$$K_d(E_i) = K_d(1 - P(E_i)) \qquad \text{Equation 11}$$

86

Final form of the coverage evolution equation including the alternative definitions of binding and desorption constants is given below. Equation 12 below reduces to the familiar Langmuir form of the binding rate under the assumption of constant $P(\tau)$, and constant $P(E_i)$.

$$\frac{d\theta_i}{dt} = K_a(\tau, E_i)C_s[f(E_i) - \theta_i] - K_d(E_i)\theta_i$$ Equation 12

Testing of the Advanced Model

Model testing undertaken can be divided into two subsections. Model verification begins with the results from an initial a priori parameterization of the advanced model. The second subsection illustrates the power of the advanced model in explaining the sigmoidal shape of the binding curve, unaccounted for by the baseline model.

Advanced Model Parametrics

Calculations were performed using the rate of adsorption and receptor density from the baseline model fitting to parameterize Equation 12. For the purposes of these calculations we are neglecting desorption, since the experimentally observed desorption rate in this case is much smaller than the binding rate. The resulting equation is given below as Equation 13.

$$\frac{d\theta_i}{dt} = K_a(\tau, E_i)C_s[f(E_i) - \theta_i]$$

Equation 13

In order to perform calculations using these equations, the functions $f(E,t)$, $R(\tau,t)$, $P(E)$, and $P(\tau)$ must be determined through an evolution equation, or by assuming a functional

form. For purposes of testing we assumed the binding probabilities P(E) and P(τ) to be
time invariant. An initial condition, f(E,0), is assumed and f(E,t) is directly computed at
each time step. Table 7 gives the parameters of the model used in the test calculations.

Table 7: Parameters for Advanced Binding Model

Diffusion Coefficient	1×10^{-10} m^2/sec
Bulk Concentration	0.208 nanoM
Receptor Density	2.1 nanomoles/m^2
Ka	3×10^5 (M-s)$^{-1}$
Time Step	50 s
Total Time Steps	500
P(τ)	$$P(\tau) = \frac{1 + \tanh(\alpha_\tau(\tau - \mu_\tau))}{2}$$
α_τ	0.20 s^{-1}
μ_τ	10 s
Energy Range	0 to 10
ΔE	0.20
P(E)	$$P(E) = \frac{1 + \tanh(\alpha_E(E - \mu_E))}{2}$$
α_E	0.50
μ_E	5
f(E,0)	Uniform Initial Distribution

Figure 61 is a summary plot of the initial distribution of open energy states, the final distribution of open energy states, and the distribution of covered energy states. The initial fractional distribution of energy states is prescribed to be constant at 0.20. From this initial condition, the distribution of open sites evolves to the final distribution of open energy sites, f(E,t). Note that the number of open sites decreases with increasing site energy, reflecting the fact that the high energy sites bind quicker than the lower energy sites. The fractional coverage within each energy state also reflects the same trend of quicker binding of high energy sites.

Next, using these ad-hoc fixed residence time and energetic parameters, we tried to reproduce the fitting of protein adsorption kinetics in capillary systems, in a similar manner performed earlier with the baseline model. Figure 62 is a comparison plot of the baseline and the fixed parameter, advanced binding model. Both approaches do not fit the sigmoidal shape of the data well, indicating the assumed parameters for the advanced model are incorrect. The advanced model is faster initially with a fitted adsorption coefficient of 7.44×10^5 $(M\text{-}s)^{-1}$, however at longer times the rate of binding slows since the high energy sites are filling and the slower binding low energy sites are now starting to dominate the kinetics. Figure 63 shows the same data as Figure 62, but with a logarithmic scale on the y-axis. This figure shows the baseline model is following exponential kinetics, as expected. The advanced model shows a similar trend with respect to the slowing of the kinetics as Figure 63. The fitted curve in Figure 62 does not show an improvement over the baseline model, mainly due to the *a priori* choice of energy and residence time parameters.
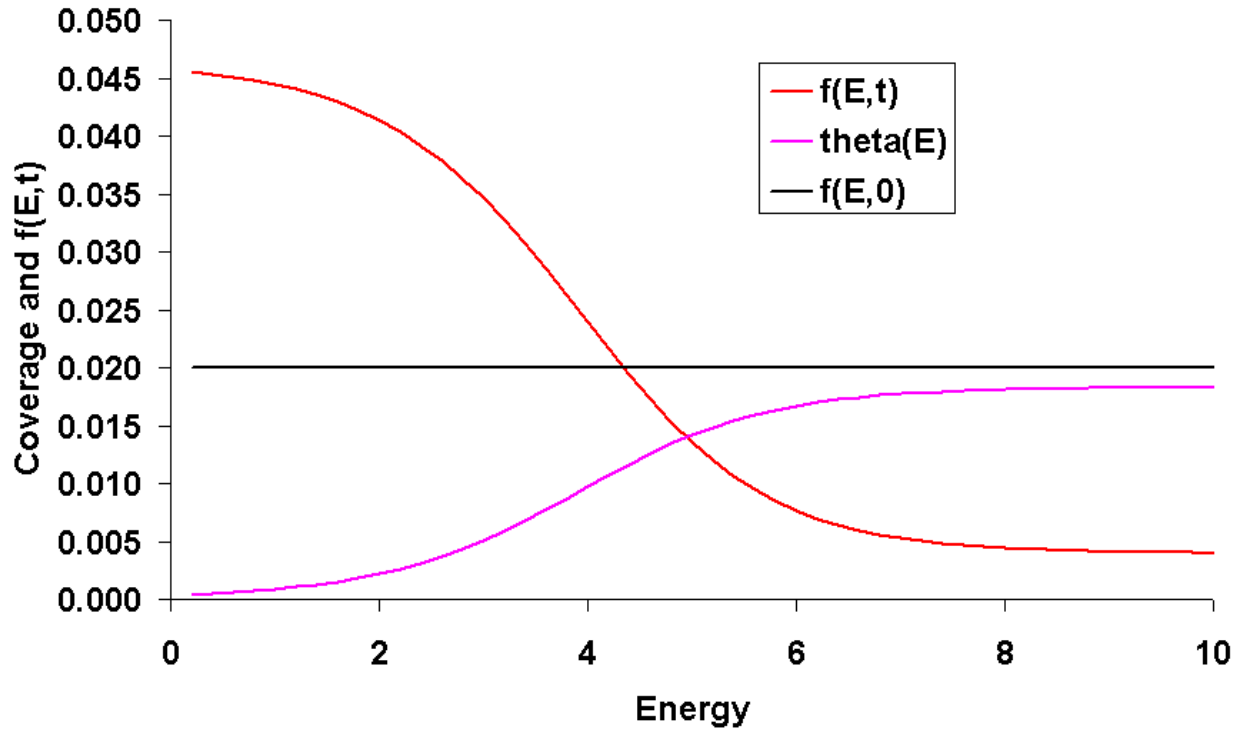
Figure 61: Plot of the initial distribution of energy sites f(E,0) [black line], the coverage as a function of energy state [purple line], and the final distribution of open energy sites f(E,t) [red line]. f(E,t) is a representation of the distribution of open sites.
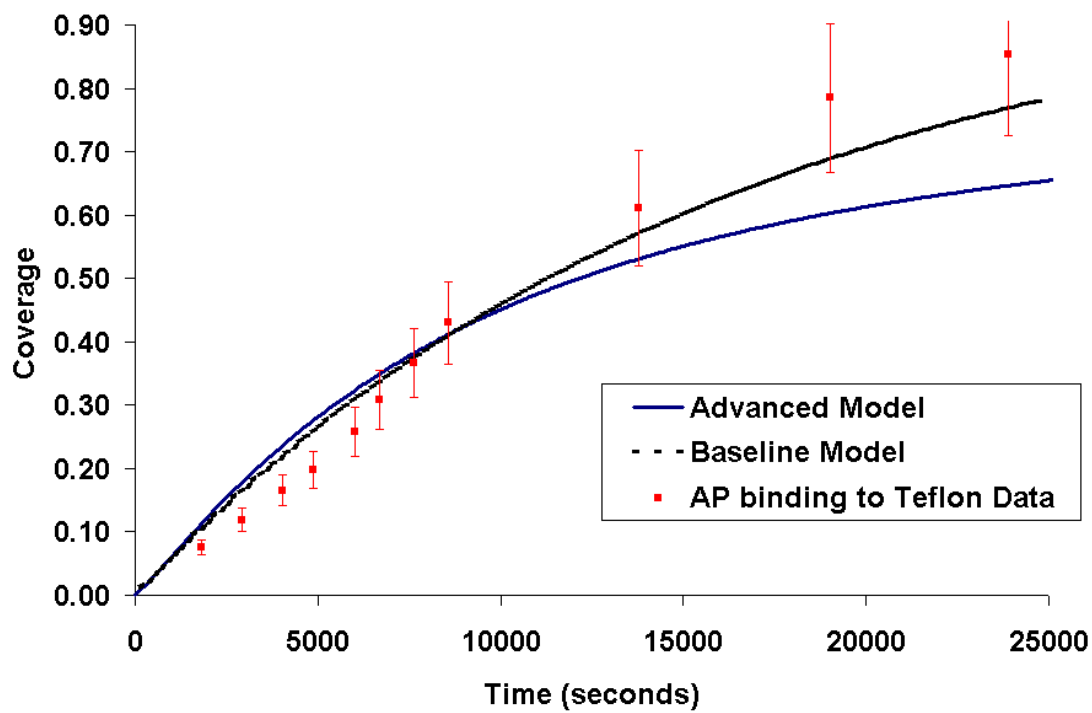
Figure 62: Comparison of the baseline and advanced models with respect to fitting the experimental data.
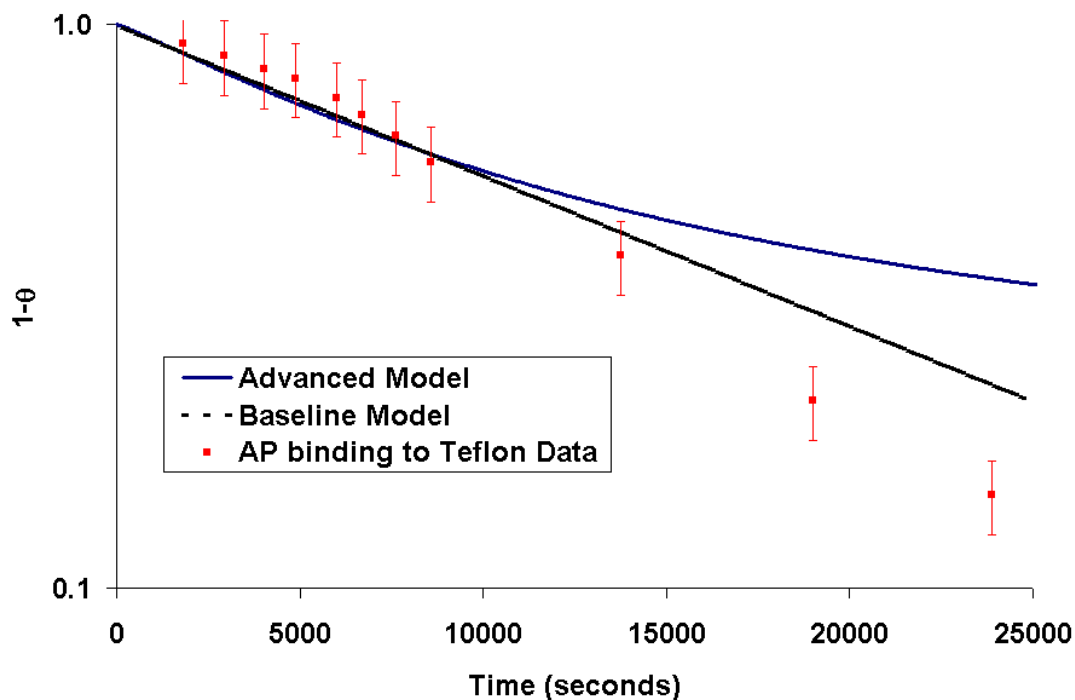
Figure 63: Log-y plot of the comparison of the baseline and advanced models with respect to fitting the experimental data.

Parametric Fitting with the Advanced Model

As discussed, in the above calculations little effect of residence time is observed due to the *a priori* parameterization of the residence time selection probability function $P(\tau)$. Figure 64 illustrates that we can obtain a much better fit to the data of alkaline phosphatase binding to Teflon by using non-linear least squares fitting to optimize the residence time and energy site selection probabilities. In Figure 64, the binding data with error bars is shown along with the baseline model fit (blue line) and the advanced model fit with initial parameterization (dashed black line).

92

The purple curve in Figure 64 is the result of performing least squares fitting on both μ_τ and k_a. By using least squares fitting varying μ_τ (see Table 7), a better fit is obtained for the short time, but the fit for longer times is suboptimal. The value of μ_τ started at a value of 2 for the blue curve and after fitting the optimal value was found to be 200 as shown in the purple curve. The energy parameters were then added as a variable to the least squares fitting. The green curve in Figure 66 is the result of fitting of the data allowing μ_τ, μ_E, and k_a to vary. Adding in the effect of changing the energy state selection probability by varying μ_E gives a much improved fit to the entire range of experimental data. The optimal values to generate the green curve in Figure 66 were found through least squares fitting, and are $K_a=3.851\times10^5$, $\mu_\tau=247$, $\mu_E=0.10$. Further improvement in the fitting could potentially be obtained by varying the functional form of $f(E,0)$, $P(E)$, or $P(\tau)$. The fitted residence time parameters are a significant improvement over the assumed values, since they reflect the actual values of the system. The fitting of the sigmoidal data was performed in a systematic manner to obtain better values of μ_τ, then μ_E, in order to give the least squares fitting program better guess values. Since the actual functional form of $P(E)$ and $P(\tau)$ are not known, parameterizing the assumed functional forms using a systematic least squares fit increases the efficiency of the fitting process.

The validity of the model can be verified by measuring the binding of alkaline phosphatase to Teflon at a range of flow rates. Lower flowrates allow a protein to be in the vicinity of a binding site longer, and are more likely to bind, resulting in a certain amount bound. Increasing the flowrate would show a gradual decrease in the amount

bound due to the decrease in the average time a protein would be around a binding site. The low value of μ_E indicates that the kinetics are predominately exponential. A low value of μ_E mathematically means that most of the binding sites bind with maximum probability in energy space. This eliminates the effect of energetics on the binding curve, producing a more exponential like shape to the curve.
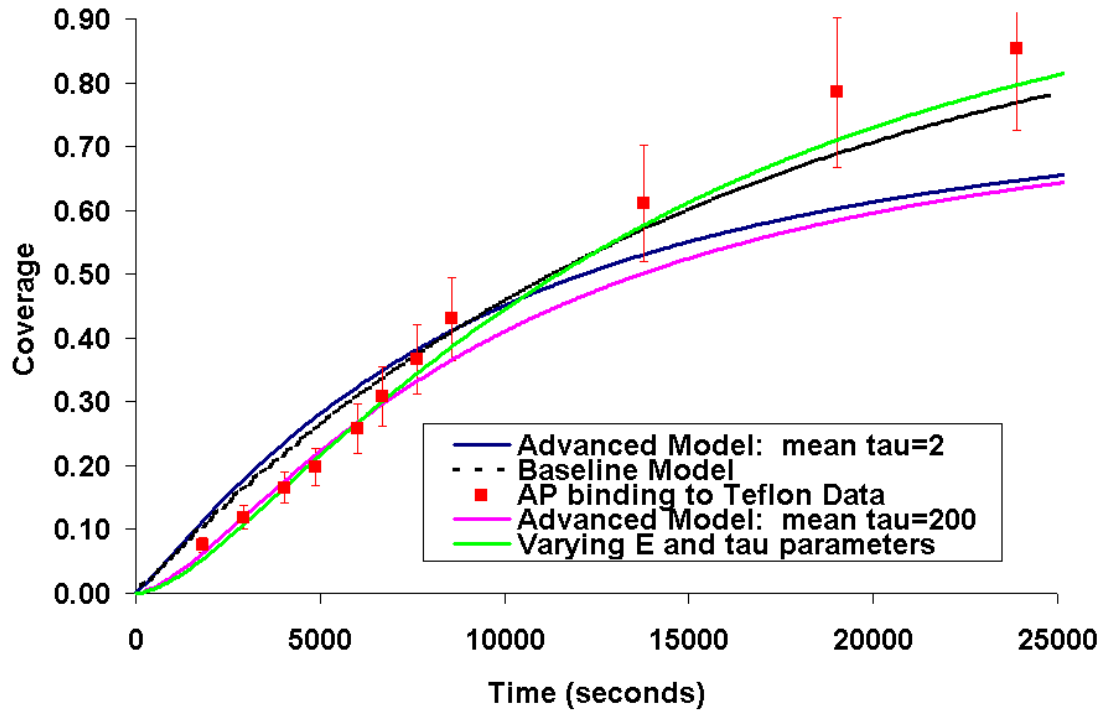
Figure 64: Binding curves showing residence time effects and energy state effects. The advanced model binding curve with a mean tau (μ_τ) of 2 shows little residence time effects, however the advanced model binding curve with mean tau (μ_τ) of 200 shows more of an effect. Adding in the effect of varying the energy state selection probability gives a much improved fit.

Final form of the Advanced Binding Model

After much thought and debate, we have arrived at the comprehensive and final form of the advanced binding model for passive binding of a protein to a polymeric surface (Equation 14)

$$\frac{dC_{Complex}(t)}{dt} = K_a^{ABM} C_{\mathbf{Pr}otein}^{NearWall}(t) C_{Sites}(t) \iint f(\tau,t) f(E,t) P_a(\tau,E) dE d\tau$$
$$- K_d^{ABM} C_{Complex}(1 - f(E,t)) P_d(E,\dot{\gamma})$$

Equation 14

The physical inputs to the equation are described below.

- K_a^{ABM} and K_d^{ABM} are the intrinsic static rate constants.

- $C_{complex}(t)$ concentration of protein on the wall.

- $C_{Protein}^{Near\ Wall}(t)$ concentration of protein very close to the wall.

- $C_{sites}(t)$ concentration of binding sites on the wall

The distribution functions describing the state of the system are given below:

- $f(\tau,t)$ distribution of local proximity times in the vicinity of a binding site. This function is calculated from a detailed balance of the computational cell in contact with the wall.

- $f(E,t)$ distribution of available binding sites of energy E. This function is tracked and updated throughout the simulation.

- $P_d(E,\dot{\gamma})$ probability that a protein will debind from an occupied site of energy E. The debinding probability is a function of the site energy and the local hydrodynamic shear rate $\dot{\gamma}$.

- $P_a(\tau,E)$ probability that a protein with proximity time τ will bind to an open site of energy E. This probability is a function of the proximity time for the proteins near a binding site and the site energy.

In order to compute the binding probability, $P_a(\tau,E)$, two methods have been identified. The first method is to directly postulate the binding site probability by using parameterized functional forms that will reproduce the specific binding behaviour. An example of a postulated binding probability is given below in Equation 15.

$$P_a(\tau,E) = \tanh\left(\sigma_\tau\left(\tau - \mu_\tau\right)\right)\tanh\left(\sigma_E\left(\tau - \mu_E\right)\right)$$

Equation 15

The second method involves postulating the probability density function and integrating it to arrive at the probability. This method allows for a more physical picture of how the binding probability depends on the site energy and proximity time. However, it is more expensive computationally due to the numerical integration to arrive at the probability. An example of this is given in Equations 16 and 17. The resulting adsorption probability is shown in Figure 65.

$$y(\tau,E) = \left(\frac{C_y}{\tau_\sigma(E)}\right)\exp\left[-\frac{1}{2}\left(\frac{\tau - \tau_\mu(E)}{\tau_\sigma(E)}\right)^2\right]$$

Equation 16

$$P(\tau, E) = \int_0^\tau \int_0^E y(\tau', E') d\tau' dE' \qquad\qquad \text{Equation 17}$$
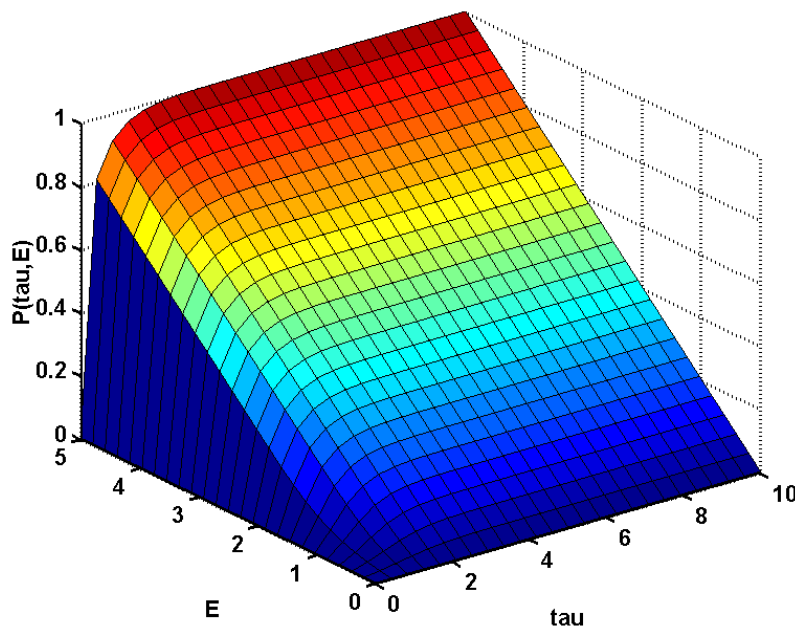
Figure 65: Typical form of the adsorption probability computed using Equations 16 and 17.

Correlation of Binding with Molecular Properties for the ABM

We sought to obtain confirmation (indirect validation) of the reported parameter values by appealing to independent, simple, molecular-based calculations, where applicable. The theoretical maximum value of P_{max} for alkaline phosphatase was computed using the structure of alkaline phosphatase obtained from the protein data bank (PDB). The structure is shown in Figure 66. The particular structure is assigned the identifier of 1AJA in the PDB. The structure has the overall dimensions of 80.2 Å x 83.7 Å x 69.7 Å. From this information, a maximum of 29.7 nmol/m^2 and a minimum of 24.7 nmol/m^2 can be computed. The experimental value of 26 nmol/m^2 falls within this range.
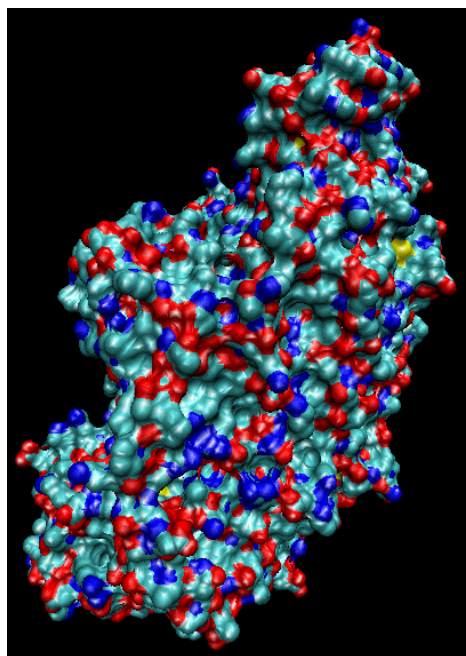
Figure 66:   Structure of Alkaline Phosphatase obtained from the protein data bank (PDB). This is the 1AJA structure. The structure is colored using light green as carbon, red is oxygen, blue is nitrogen, and yellow is sulfur.

The objective of this work was to correlate a molecular property of the protein with the kinetic parameters. The database of Dan Nicolau was inspected to see what type of data was contained within the database [Nicolau et al.]. There are 342 total entries in the database. Each entry lists the buffer conditions, the bulk concentration, the surface concentration, and the experimental method used to measure the surface concentration. It was determined that there were no systems in the database that use PEEK as a surface. However, there were several (approximately 12) systems that use Teflon as a surface. Of the 12 systems (with Teflon surfaces), there were only 7 that had molecular structure information available in the protein data bank (PDB). However, the appropriate structure to use for two of the systems (IgG and IgM) could not be determined. Another system,

fibronectin, posed a problem in that there was only one data point listed for it in the database, and so it was not used. This narrowed the field down to 4 proteins.

The Langmuir isotherm for each of the four remaining systems was reconstructed using the database entries (C_{bulk} versus $C_{surface}$ plot) and fit using the same nonlinear fitting applied to the static data previously described. The four proteins were cutinase, alpha-2-macroglobulin, alpha-chymotrypsin, and HSA. The fits provided a value for (k_a/k_d) and P_{max} for each of the four proteins binding to Teflon. The goal was then to correlate the fitted values with a molecular level property of the protein. The PDB structures for each of the existing proteins (glucose oxidase, alkaline phosphatase, acid phosphatase, and horseradish peroxidase), and the four proteins from the Nicolau database were obtained. A software program called the Protein Surface Property Calculator (PSPC) was used to compute the surface properties. This program is available on Dan Nicolau's website (http:/www.bioanoeng.com/downloads.html – as of April 11, 2003). PSPC will compute information on properties of the solvent accessible area of the protein such as the area occupied by positive or negative charge. All nine of the proteins were analyzed using the PSPC program (using the recommended solvent radius of 1.4 angstroms) and the output was analyzed to determine any correlation between the kinetic coefficients and a protein surface property. A strong and well defined trend was identified that correlates the number of binding sites with the total protein area with positive charge (Figure 67). The correlation indicates that as the protein area with positive charge increases, the effective number of binding sites decreases.
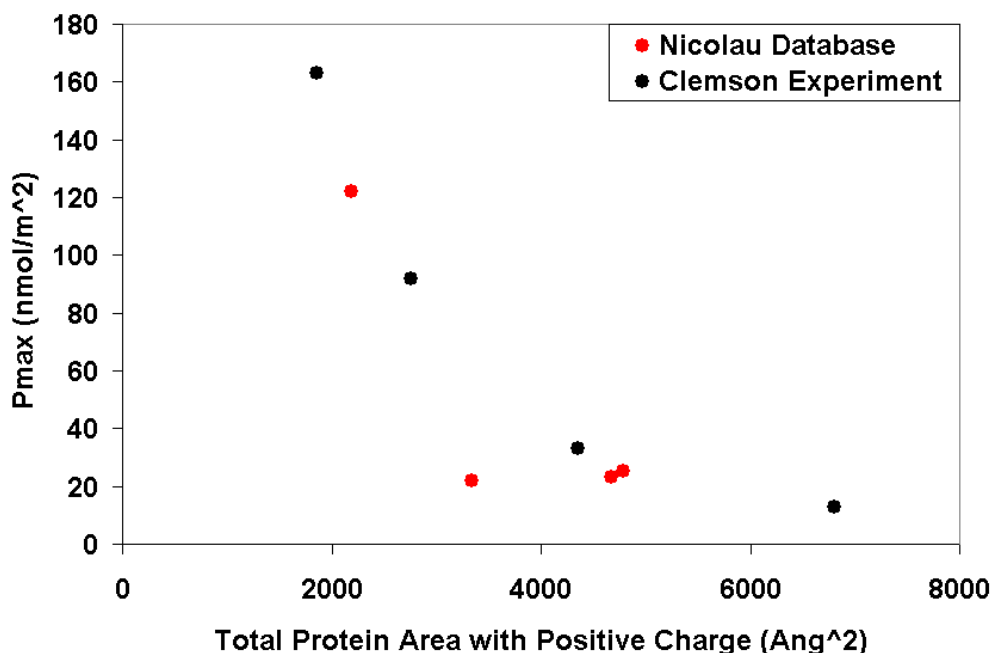
Figure 67: Correlation of the number of binding sites with the total protein area containing positive charge. The number of binding sites decreases as the positive charge increases.

Simulation of Protein Binding in Electro-osmotic Flow (EOF)

This section reports on the efforts to perform simulations of coupled EOF/protein binding. The objective of this study was to understand how the bound protein alters the surface charge, thereby altering the double layer body force on the fluid and subsequently the induced EOF flow. This effect in turn changes the transport of protein to the surface and alters the binding. The coupling of the two effects will be discussed along with the models used. Also in this section we will present some preliminary calculations of passive protein binding in the UC Berkeley microcantilever based biosensor in order to quantify the amount of protein lost to passive binding during an experiment.

Experiment

As shown in Figure 68, the high conductivity buffer is injected into 5 cm capillary of inner diameter 76 μm by electroosmotic flow (EOF). The time required for high conductivity buffer to reach the outlet of the channel is measured so that EOF mobility, or zeta potential of the channel wall, can be extracted. Horseradish peroxidase (HRP: 42 kD) is added to high conductivity buffer as the injection starts. The isoelectric point of HRP is at pH 7.2 so that the net charge of the protein is almost zero under these conditions. The protein binds to the channel surface, changing the surface potential. This leads to an altered EOF mobility and hence variation in the total time required for the protein to reach the channel outlet. The experiments record the total time required for high conductivity buffer to reach the low conductivity buffer reservoir for both unexposed and exposed capillaries. The difference of sloshing time indicates the effect of protein binding and its implication to EOF. Figure 68 illustrates the experiment setup and operation conditions.
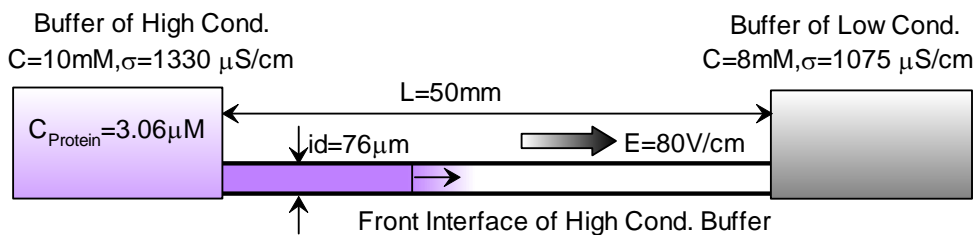
Figure 68: Schematic of the system used in coupled EOF/protein binding experiments and simulations

Theory

The mechanism of binding protein to the channel surface is assumed to be 2nd order reversible (baseline model) shown in Equation 18. This model allows calculation of surface protein concentration f by using Equations 18 and 19.

$$\frac{\partial f}{\partial t} = \chi(f, c_i^w) = k_a c_b^w (f_m - f) - k_d f \qquad \text{Equation 18}$$

$$D_b \frac{\partial c_b}{\partial n} + \frac{\partial f}{\partial t} = 0 \qquad \text{Equation 19}$$

The subscript b denotes binding species and superscript w means the value at the wall.

The dependency of zeta potential on surface protein concentration may exhibit complex behaviour and varies with the buffer and operation conditions. Measurement from current experiment shows that the EOF mobility is 3.45×10^{-8} m^2/V.s for unexposed capillary and 2.10×10^{-8} m^2/V.s for fully exposed capillary. The simplest model is the linear model relating surface protein concentration to the modified mobility as shown in Equation 20.

$$\varsigma = \varsigma(f, c_i, pH, \cdots) = \varsigma_0 \left[1 - \gamma \frac{f}{f_m} \right] \qquad \text{Equation 20}$$

Here f_m is the total surface concentration and γ is the coverage ratio of adsorbed protein determined from experiments.
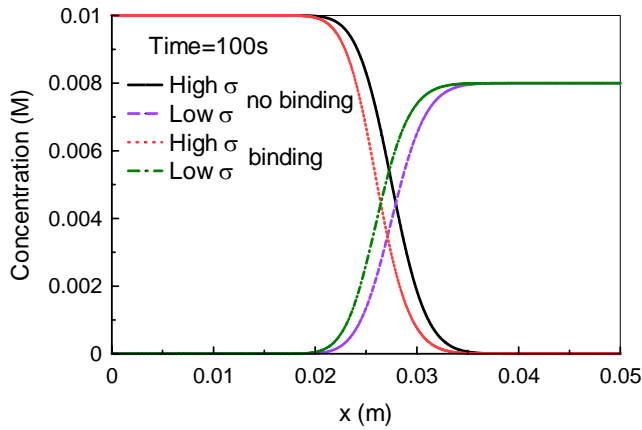
Figure 69: Comparison of buffer concentration at time t=100s for the cases of binding and no binding.

The kinetic constants for binding were obtained from passive binding experiments previously performed. Typical values of the binding constants of HRP are $k_a = 10^5/\text{Ms}$, $k_d = 10^{-6}/\text{s}$. The averaged concentration of high conductivity buffer across the channel cross-section is used as a criterion to estimate the time taken for the high-low buffer concentration interface to migrate to other end of the channel. If the averaged concentration of high conductivity at the outlet exceeds 95% of the initial value, the simulation time is recorded as sloshing time. Simulations are performed for both unexposed and exposed capillaries. The ratio of mobilities of exposed to unexposed capillary (data supplied by NIST; μ_{eof} (unexposed) = 3.45x10^{-8} m^2/(V.s), μ_{eof} (exposed) = 2.10x10^{-8} m^2/(V.s)) is used as the value for μ in the model. Figure 69 compares spatial distribution of buffer concentration at T=100s. It is observed that the front interface of high conductivity buffer in protein exposed capillary falls behind due to the reduced EOF mobility as protein binding occurs, leading to increased sloshing time. The sloshing times are approximately 210 and 240 seconds for unexposed and exposed capillaries, respectively.

The concentration profiles for buffer, and free and bound protein, are shown in Figure 70 at time t=58s. Following observations are made:

- The interface between high and low conductivity buffers becomes diffused due to the migration of ions

- The development of near-wall concentration in the capillary falls behind high conductivity buffer interface because of the adsorption of protein from the bulk.

The EOF velocity distribution across the capillary is shown in Figure 71. We observed that:

- The velocity distribution is non-uniform because of inhomogeneous surface concentration. The reduction of EOF as protein flows in the capillary is the result of reduced EOF mobility and local electric field.

- An internal pressure gradient is generated as a result of flow continuity, leading to non-uniform axial velocity in the capillary.

Figure 71 shows axial velocity at the outer edge of double layer and the velocity profile in the radial direction at x=1, 2.5 and 4 cm, corresponding to locations behind, close and ahead of the high conductivity buffer interface.

The binding curve for protein along the length of the channel is shown in Figure 72. The time required for full coverage of protein at the capillary surface is about 580s, longer than sloshing time for high conductivity buffer. This is because of rapid binding in the radial direction coupled with relatively small diffusion ($D=1x10^{-11}$ m^2/s) coefficient of the HRP to diffuse to the near wall region. The ratio of diffusion and convection time estimated from simulation is about $O(10^{-2})$, leading to rapid depletion of protein in the bulk solution.
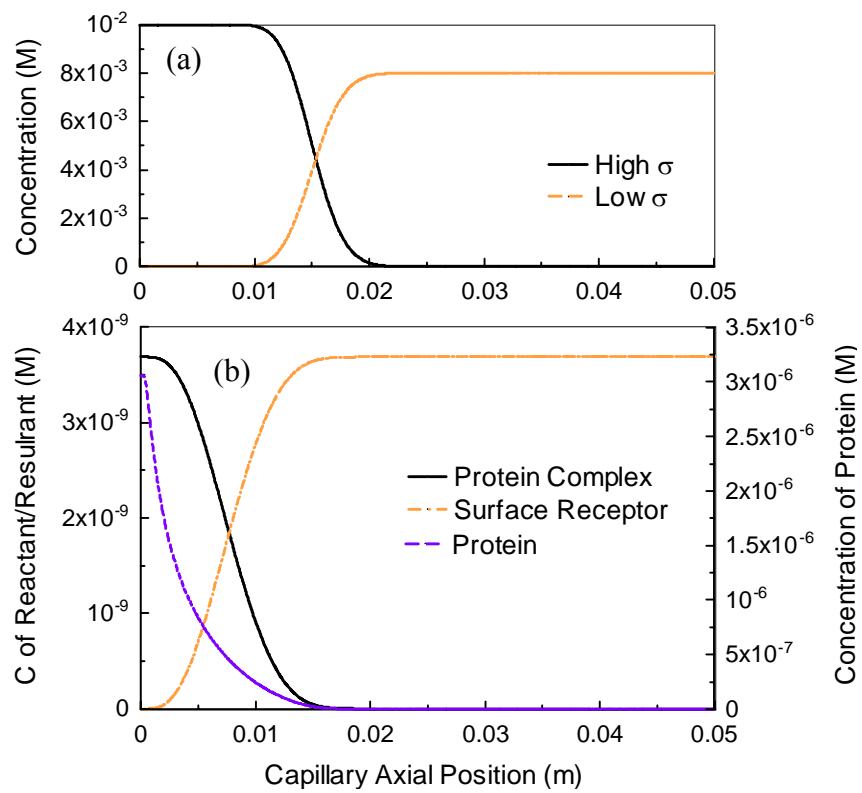
Figure 70: (a) Concentration of buffer and (b) surface concentration, near wall protein concentration.
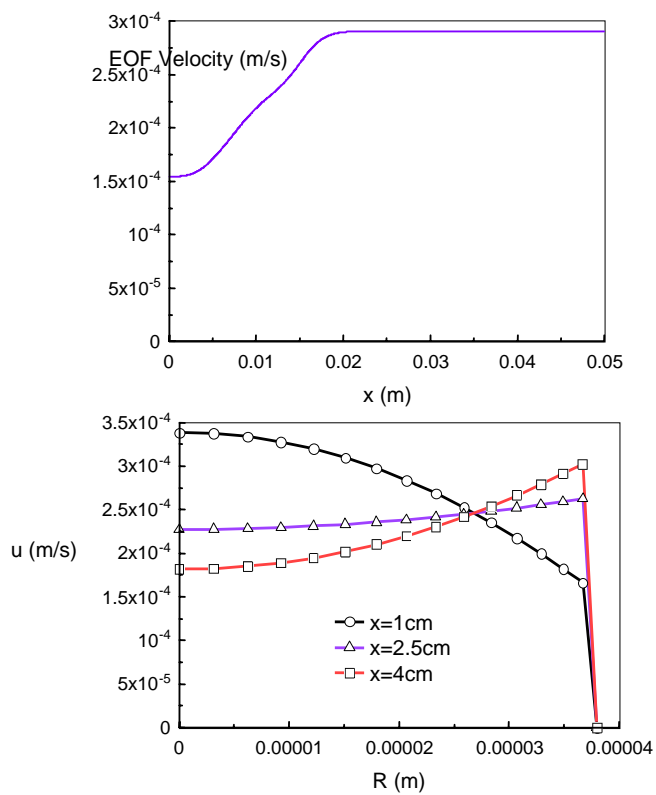
Figure 71: (a) Axial distribution of EOF velocity at the outer edge of double layer and (b) velocity profile across the capillary at three locations.
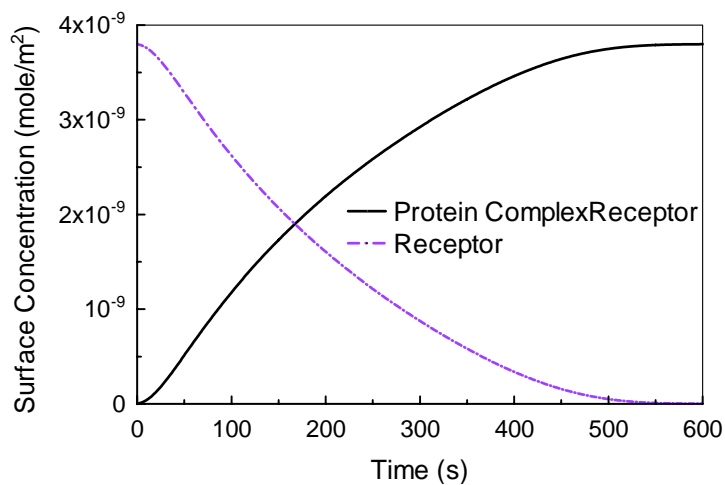
Figure 72: Progress of Averaged Surface Protein-complex Concentration.

Application of Advanced Binding Model to Berkeley Sensor Geometry

A potential problem was identified for the case of the UC Berkeley microcantilever flowcell developed in the DARPA SIMBIOSYS program. The problem deals with identifying potential problems with the amount of protein (or possibly DNA) that is lost due to passive binding. The clinical samples can potentially be quite dilute, so the amount of loss can become important as shown in Figure 1.

The flow cell geometry is shown schematically in Figure 73. The flowcell is approximately 2 mm long, 1.5 mm wide and 1.5 mm high. The microfluidic device consists of an inlet and an outlet as well as a thin microcantilever sensor that deflects whenever binding occurs on the upper surface. This deflection can be quantified by using an optical technique.
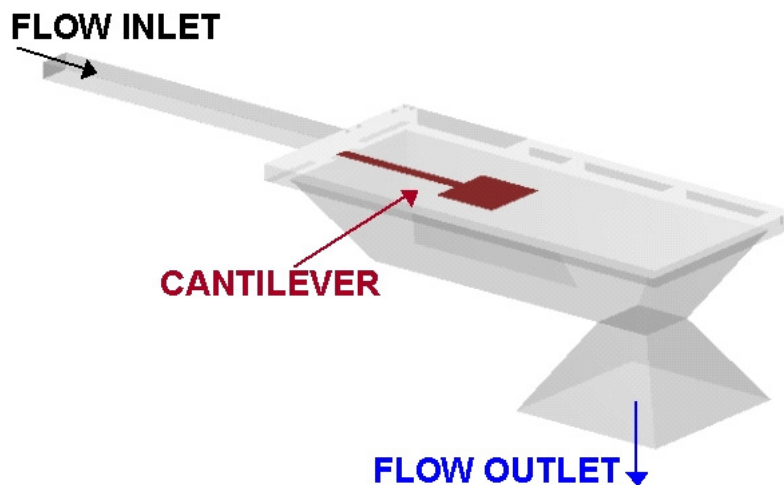
Figure 73: UC Berkeley flow cell used for the analysis showing the inlet, outlet and the microcantilever.

The simulations consisted of a buffer solution (density 1000 kg/m^3 and viscosity of 1.0E-6 kg/m-s) containing alkaline phosphatase (AP) at a concentration of 10nM. The inlet flowrate was set at 1.65 µL/min (velocity of 0.0055 m/s). AP was assumed to bind to all interior surfaces of the flowcell. Kinetic coefficients for this binding reaction have been determined at CFDRC based on data from experiments performed at Clemson University. Based on the data fitting shown (Figure 74), the kinetic constants have been identified as K_a = 5.9x10^5 (M-s)$^{-1}$; K_d= 5.0x10^{-6} s^{-1}; and the maximum number of available binding sites determined to be 4.27x10^{-9} mol/m^2. The diffusion coefficient for AP was assumed to be 2.0x10^{-11} m^2/s. Initially, it is assumed that the flowcell does not contain any AP in the volume or on the surface. The results of the simulations are given in the next section. The simulations were performed for a total of 20 seconds with a time step of 0.10 seconds.
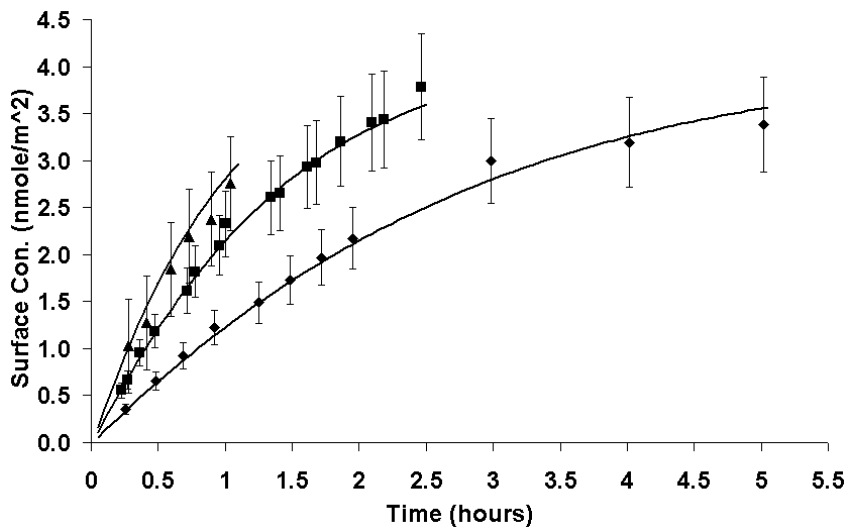
Figure 74: Graph of the data for alkaline phosphatase binding to PEEK with the least squares fits.

Because of the very low flow rate, the flow is close to the creeping flow regime. There are no discernable recirculation zones, even though the flow has to navigate around the cantilever to reach the outlet. Figure 75 is a plot of the streamlines colored by the AP concentration at T=20s. There are considerable dead zones in the flowcell where the flow is nearly stagnant. As expected, these are the corner regions of the geometry. A lack of any appreciable convective transfer limits the rate of transfer, since the protein must now diffuse to these regions.
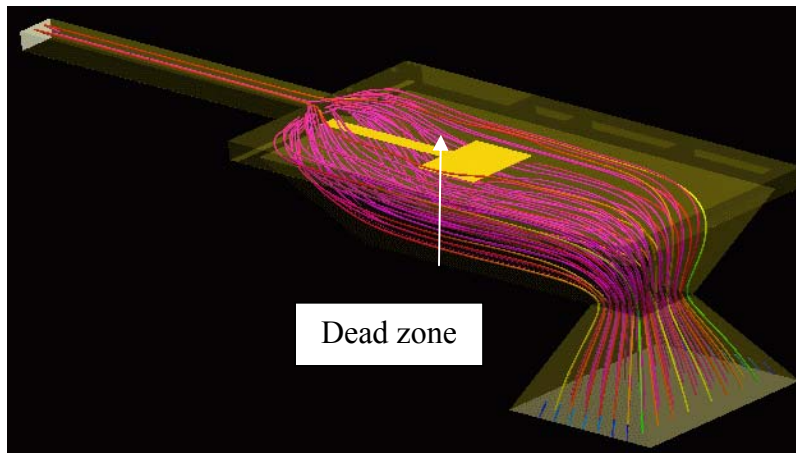
Figure 75: Streamlines showing flow pattern in the flow cell at T=20s.

A series of snapshots (8, 12, 16, and 20s) of the temporal variation in the protein binding is shown in Figure 76. As the protein flows in, it starts to passively bind with all surfaces it comes in contact with, including the cantilever. The binding pattern and surface density of the bound protein follows a pattern similar to the path of the streamlines. The extent of binding increases over time as more and more protein comes into contact with the walls of the microfluidic flow cell. The stagnation zones have very little binding because little

protein is getting into the dead regions due to convection. The little protein that does

reach the stagnant zones must do so by diffusion.
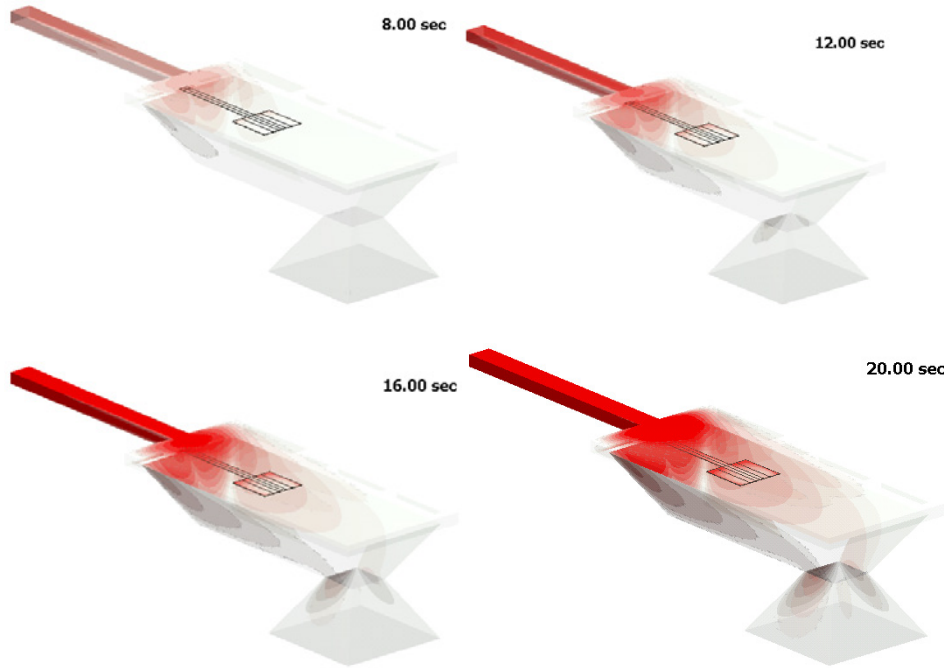
Figure 76: A Series of Snapshots of the Protein Binding at 8, 12, 16, and 20 seconds.

Figure 77 shows a series of snapshots of protein binding on the cantilever surface as a

function of time. At any instant, the binding rate on the paddle is relatively slow. This can

be explained by the fact that the cantilever paddle, offers a higher resistance to flow along

the main arm. As a result, there is more flow going around the main cantilever, as

compared to the paddle leading to reduced mass transfer rates at the paddle surface, and

hence a slower binding rate on the paddle.
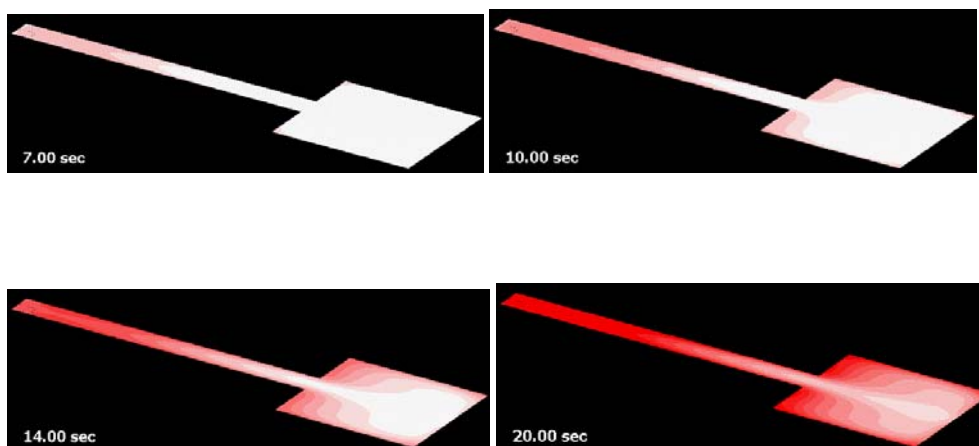
Figure 77: A series of snapshots at 7, 10, 14, and 20 seconds showing the binding of protein onto the cantilever surface.

Figure 78 shows three graphs that sum up the loss calculation for the binding chamber. Figure 78a shows the ratio of the total amount bound on all surfaces to the amount bound on the cantilever. At times less than 5 seconds, the ratio is essentially constant at 10. After 5 seconds the ratio begins to increase. This indicates that there is at any point the amount of protein bound to all surfaces of the flowcell is 10X that on the cantilever. The amount of sample that is lost to passive binding is shown in Figure 78b. This figure indicates that over our time range only about 2.5% of the sample is lost to passive binding. However, Figure 78c indicates that only about 0.15% of the sample actually binds to the cantilever over the simulated time period. A reduction in the sample loss could be achieved by coating the interior of the flowcell with a lower passive binding coating such as polyethyleneglycol (PEG).
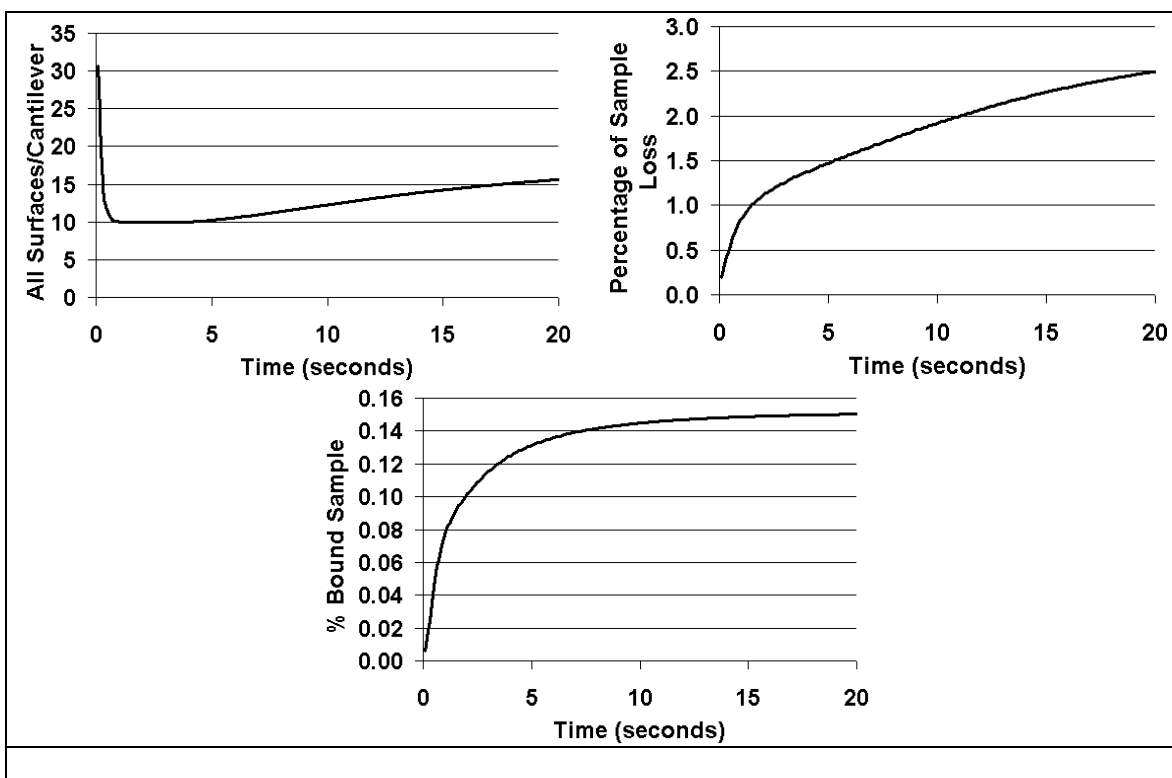
Figure 78: (a) Plot of the ratio of passive binding on all surfaces to passive binding on the cantilever. (b) Percentage of the incoming sample that is lost to passive binding. (c) Percentage of the incoming sample that binds to the cantilever.

CONCLUSIONS

We have shown here that flow can be a key variable in the adsorption behaviour of proteins. This has important consequences for the measurement of adsorption phenomena in liquids and the design of microfluidic systems, since measurements made under static conditions are not necessarily able to be extrapolated to flow conditions. These results also show that even under static conditions, the rate of protein adsorption may not be well described by a single number; the limiting case, the rate of adsorption at zero time and zero concentration, only reflects the adsorption behaviour of a protein in

112

that particular orientation at that particular site. Only the most fastidiously prepared surfaces will possess a single type of adsorption environment, and even then protein orientation remains unaddressed. On real surfaces there are a range of sites with varying affinities, high affinity sites are preferentially occupied, and the sticking coefficient will be a function of coverage. Assessing protein adsorption over a range of concentrations allows an estimate to be made of the range of site affinities, and the fraction of the total surface they represent, and appears to be the best way of determining protein/surface interactions which will reflect their behaviour in real systems.

Owing to the increasing use of microfluidic devices with high surface/volume ratios in combination with biological systems there is a need for a model of protein adsorption which can incorporate surface and flow effects. Controlling adsorption will be a key aspect of the design of these devices; adsorption may be highly undesirable in some areas, since it could partially or fully deplete the flow stream of key components, but in other applications adsorption is required in order for detection to occur (e.g. surface plasmon resonance). Careful understanding of the interaction of flow, surface availability and adsorption is required.

The effect of protein adsorption on electroosmotic flow was measured using dynamic current monitoring. It was always observed that the adsorption of protein to a surface slowed the electro-osmotic flowrate. Detailed studies on the adsorption of BSA to a fused silica capillary at pH 5 (the iselectric point) found adsorption that was exceedingly rapid, and essentially irreversible, with a large drop in the electroosmotic mobility

following exposure of the silica capillary to a protein bearing buffer. At pH 7.4, adsorption was partially reversible, and slower than at pH 5, with a substantial amount of the initial electroosmotic mobility being recovered upon replacement of the protein buffer solution in the capillary with buffer alone. The reduced rate of adsorption at pH 7.4 compared with pH 5 was concluded to be due to electrostatic repulsion between the negatively charged protein and the negatively charged silica surface. The increased rate of desorption was concluded to be due to electrophoresis, with the negatively charged protein being pulled off the wall at pH 7.4, a mechanism not available at pH 5. This was supported by experiments carried out at a lower field strength at pH 7.4, where a reduced field strength resulted in less desorption.

In systems which rely on electroosmotic flow to move solution around, such as in MEMS devices, the change in EOF with protein adsorption could substantially alter the performance of such devices, with reduced flow rate leading to longer retention times. Also in these devices, there is the potential for cross contamination as adsorbed material slowly desorbs, with a possible false positive result, or the depletion of material from an analytical stream resulting in a false negative. This problem would be particularly acute in circumstances, such as pH gradient focusing, where proteins are deliberately moved to zones at their iselectric point.

The change in electroosmotic mobility after protein adsorption was concluded to be due to the adsorbed molecules making it difficult for flow to occur, imposing drag on fluid movement within the crucial electrical double layer, rather than due to the presentation of a new surface to the bulk fluid with different EOF characteristics. This view predicts that

the μ_{eof} should increase as the concentration of salts in the system is decreased, and this behaviour was observed with BSA on silica at pH 5.

Different surface modification methodologies were also investigated, including plasma modification under different atmospheres, and laser ablation where the surface functionalities are established simultaneously with the formation of the microchannel.

Our extensive studies on protein adsorption, protein detection and quantitation, and different flow regimes allows us to start to incorporate surface effects into a new, advanced model of protein adsorption. As we have shown here, the model should be able to account for dynamic environment features, and the effect of the time the protein spends in proximity to the surface. Flow vs. static conditions can be expected to change throughout even a simple device, as small flow channels (high flow velocities) give way to larger volumes (small velocities and possibly locally stagnant areas). The model should also incorporate surface chemistry, describing the adsorbing surface. The system we have described in the methods section is a cheap, simple bench top means for obtaining this crucial information, but still needs further development to be fully implemented.

REFERENCES

Butler, J. E., Navarro, P. & Sun, J.. *Immun. Invest.* **26**, 39 - 54 (1997).

Butler, J. E. in *Methods in Enzymology* 482 - 523 (Academic Press, New York, 1981).

Coburn, S. P., Mahuren, J. D., Jain, M., Zubovic, Y. & Wortsman, J. *J Clin Endocrinol Metab* 83, 3951-7. (1998).

Edwards, D. A., Goldstein, B., Cohen, D. S.Evju *J. Mathematical Biology* **39**, 533-561 (1999).

Evju, J., Feng, J., Krishnamoorthy, S., Sundaram, S., Locascio, L.E., Henry, A.C., Ross, D., Tarlov, M.J. and Hickman, J.J., Manuscript in preparation for submission to *Anal. Chem.*

Fernley, H. N. in *The Enzymes* (ed. Boyer, P. D.) 424 (Academic Press, New York, 1971).

Fosset, M., Chappelet-Tordo, D., Lazdunski, M. *Biochemistry* **13**, 1783 - 1787 (1974).

Gregg, S. J.., Sing, K.S.W, *Adsorption, surface area and porosity* (Academic Press, London, 1967).

Howell P., Wagner M., Montgomery C., Locascio L. E., Tarlov M. J. Hickman J. J., Applied Physics Letters, 84(10), 1668-1670 (2004)

Jenkins, J.; Prabhakarpandian, B.; Lenghaus, K.; Hickman, J.; Sundaram, S. *Analytical Biochemistry*, **331**(2), 207-215 (2004)

Jin F., Hickman J. J., Lenghaus K., Marcus R. K., *Analytical and Bioanalytical Chemistry*, **380**(2), 204-211 (2004)

Jin F., Hickman, J. J., Lenghaus K., Marcus R. K, *J. Anal. At. Spectrom.*, **19**(9), 1199-1205 (2004)

Jin F, Lenghaus K, Hickman J. J. Marcus R. K., *Analytical Chemistry*, **75**, 4801 (2003).

Kovacs G. T. A., *Micromachined Transducers Sourcebook* (McGraw-Hill, 1998)

Lenghaus K., J. Dale, C. Henderson, D. Henry, E. Loghin, and J. J. Hickman, *Langmuir*, **19** 5971 (2003).

Locascio L. E., Perso C. E., Lee C. S., *J Chromatogr A* **857**, 275-84 (Oct 1, 1999)

Nicolau, D. V. Jr., Fulga, F., Nicolau, D. V., Biomedical Microdevices **5** (3), 227-233, 2003.

Norde, W. & Zoungrana, T. *Prog. Biotechnol.* **15**, 495-504 (1998)

Norde, W. & Giacomelli, C. E. *Macromol. Symp.* **145**, 125-136 (1999)

Root D.D., Wang K., *Anal. Biochem.* 209 (1993) 354

Schomburg, D., Salzmann, M. (ed.) *Enzyme Handbook* (Springer-Verlag, New York, 1995)

Stenger D. A., Georger J. H., Dulcey C. S., Hickman J. J., Rudolph A. S., Nielsen T. B., McCort S. M.,. Calvert J. M; *J. Am. Chem. Soc*.;**114**(22); 8435-8442, 1992.

Thormann W., Zhang, C-X., Caslavska, J., Gebauer, P., Mosher, R.A., *Anal Chem* **70**, 549 - 562 (1998).

Publications and Presentations
Review

Lenghaus, K., Solomon, D.H. "Adsorption on Carbon" in Encyclopedia of Colloid and Surface Science, ed A. Hubbard, Dekker, 2002

Journal Articles

Fuxia Jin, James J. Hickman, Keith Lenghaus, and R. Kenneth Marcus, "Total Protein Determinations by Particle Beam/ Hollow Cathode Optical Emission Spectroscopy (PB/HC-OES) System III: Improved Sensitivity Through Use of Non-volatile Salts for Enhanced Particle Transport", *Analytical and Bioanalytical Chemistry* (2004), 380(2), 204-211.

Fuxia Jin, James J. Hickman, Keith Lenghaus, and R. Kenneth Marcus, "Total Protein Determinations by Particle Beam/ Hollow Cathode Optical Emission Spectroscopy (PB/HC-OES) System II: Improved Sensitivity Through Use of Silica Micro-particles as Carrier Agents for Enhanced Particle Transport", *Journal of Analytical Atomic Spectrometry* (2004), 19(9), 1199-1205.

Beata Sweryda-Krawiec, Halagowder Devaraj, George Jacob, and James J. Hickman, "A New Interpretation of Serum Albumin Surface Passivation.*" Langmuir* (2004), 20(6), 2054-2056.

Jon K. Evju, Peter Howell, Matt Wagner, Christopher Montgomery, Laurie E. Locascio, Michael J. Tarlov and James J. Hickman, "Atmospheric Pressure Microplasmas for Modifying Sealed Microfluidic Devices." *Applied Physics Letters* (2004), 84(10), 1668-1670.

Jenkins, J., Prabhakarpandian, B., Lenghaus, K, Hickman J., Sundaram, S., "Fluidics Resolved Analysis of Protein Adsorption In A Biomicrofluidic System", *Analytical Biochemistry* (2004), 331(2), 207-215.

Lenghaus, K., Dale, J., Henderson, C., Henry, D., Loghin, E., Hickman, J.J. "Enzymes as Ultra-sensitive probes for adsorption" *Langmuir,* **19**:5971 (2003)

Jin, F., Lenghaus, K., Hickman, J.J., Marcus, R.K. "A Novel Method for Total Protein Determinations by Particle Beam/ Hollow Cathode Optical Emission Spectroscopy (PB/HC-OES) System" *Analytical Chemistry*, **75**/4801 (2003)

K. Lenghaus, J. Dale, D. Henry, S. Sundaram, J. Jenkins, M. Tarlov, L. Locascio, J. Evju, and J.J. Hickman, "Towards Understanding the Effects of Surface Modification on the Biointerface in Biosensors," *Polymer Preprints* (American Chemical Society, Division of Polymer Chemistry) (2003), 44(1), 208-209.

B. Sweryda-Krawiec, G. Jacob, H. Devaraj, J.J. Hickman, "Langmuir Adsorption Isotherms for BSA on Glass Based on XPS Analysis," *Proc. Soc. Biomat.*, (2002).

Hickman, James J.; Sweryda-Krawiec, Beata; Devaraj, Halagowder; Jacob, George. Characterization of surface adsorbed proteins by XPS and the standard colorimetric assays. Abstracts of Papers, 223rd ACS National Meeting, Orlando, FL, United States, April 7-11, 2002

Jenkins, J. W., Sundaram, S., Makhijani, V.B., "Coupling between Nanoscale and Microscale Modeling for Microfluidic Device," paper accepted for publication in *Proceedings of 2002 International Conference in Computational Nanoscience (ICCN 2002)* San Juan, Puerto Rico, April 22-25, 2002.

Presentations

J.J. Hickman, K. Lenghaus, D. Henry, J. Dale, K. Wilson, A. Bhattacharyva, S. Sundaram, and J. Jemkins, "Experimental and Theoretical Examination of Protein Adsorption on Static and Flow Conditions." 204th Meeting of the Electrochemical Society, October 14, 2003 Orlando, FL.

Arpita Bhattacharyya, Keith Lenghaus, Devaraj Halagowder, James J. Hickman "Adsorption Behaviour of Proteins in Microcapillaries." Oral presentation, 50th American Vacuum Society meeting, October, 2003.

DARPA Site Visit September 29th, 2003; Presentations to Clare Thiem and Anantha Krishnan

Presenter	Topic
J. Hickman	Introduction and Overview
Keith Lenghaus	Static vs. Flow Overview
Kerry Wilson	Effect of Pressure Driven Flow on Adsorption of Alkaline Phosphatase onto PEEK Surfaces
Arpita Bhattacharyya	Desorption vs. Denaturation of Adsorbed Enzymes

Ken Marcus	Total Protein Determinations by Particle Beam Hollow Cathode Optical Emission Spectroscopy
David Henry	Development and Use of a Microfluidics Testbed for Protein Adsorption Experiments
Aggie Simionescu	Gel Electrophoresis - A Detection Method for Nanogram Levels of Adsorbed Proteins
ChangJu Chun	Protein Adsorption on the PEG-Modified Silica Surface
Mike Tarlov	Nist Overview (presented by Keith Lenghaus)
Keith Lenghaus	EO Flow with Protein Adsorption
Shankar Sundaram/ Jerry Jenkins	Computational Analysis of Protein-Surface Interactions in BIOMEMS & Biomicrofluidic Devices
Feng Wang	Recent Developments in CFD Modeling of Protein Adsorption in Microfluidics
Bob Latour	Future Considerations: Incorporation of Molecular-Level Protein Adsorption Effects into CFD Model
J. Hickman	Wrap Up

J.J. Hickman, "Development of Hybrid Cellular Systems via Surface Microengineering." Georgia Institute of Technology, September 25, 2003 Atlanta, GA.

J.J. Hickman, "Development and Experimental Verification of Surface Effects in a Fluids Model." Joint DARPA BioFlips / Simbiosys meeting, September 10-12, 2003, Monterey, CA.

J.J. Hickman, "Building Minimalistic Hybrid Neuroelectric Devices." University of Southern California, September 8, 2003, Los Angeles, CA.

J.J. Hickman, "Integration of Neuronal Systems with Silicon Microstructures for New Hybrid Diagnostic Devices." Neuroscience Grand Rounds, Medical University of South Carolina, August 14, 2003, Charleston, SC.

J.J. Hickman, "Integration of Cells and Silicon Devices via Surface Microengineering." North Carolina State University / University of North Carolina Joint Seminar Series. June 4-6, 2003, Raleigh, NC.

J.J. Hickman, "Integration of Cells and Silicon Devices via Surface Microengineering." "Workshop on Nonlinear Dynamics, Control & Guidance of Unmanned Autonomous Vehicles". May 29-30, 2003, Gainesville, FL.

Arpita Bhattacharyya, Keith Lenghaus, Devaraj Halagowder, James J. Hickman, Jerry Jenkins, and Shankar Sundaram, "Adsorption behaviour of a protein under flow and static conditions." Poster presentation at the 29th Society for Biomaterials meeting, Reno, Nevada, May 2003.

Keith Lenghaus, Jeff Dale, David Henry, Shankar Sundaram, Jerry Jenkin, and James J. Hickman, "Design and Experimental Validation of a MEMS device testbed to create biocompatible systems." Oral presentation at the 29th Society for Biomaterials meeting, Reno, Nevada, May 2003.

J.J. Hickman, "Toward Understanding the Effects of Surface Modification on the Biointerface in Biosensors." 225th ACS National Meeting, March 23-27, 2003, New Orleans, LA

J.J. Hickman, "The Role of Chemistry in Biomedical Sciences." Chemistry Department, North Carolina State University, March 20, 2003, Raleigh, NC.

Keith Lenghaus, Jeff Dale, David Henry, Shankar Sundaram, Jerry Jenkin, Mike Tarlov, Laurie Locascio, Jon Evju, and James J. Hickman, "Towards Understanding The Effects Of Surface Modification On The Biointerface In Biosensors." Invited talk at the 225th ACS meeting, New Orleans, Louisiana, March 2003.

J.J. Hickman, "Development and Experimental Verification of Surface Effects in a Fluids Model." Joint DARPA BioFlips / Simbiosys meeting, February 5-7, 2003, Santa Barbara, CA.

J.J. Hickman, "Integration of Cells and Silicon Devices via Surface Microengineering." Bioengineering Dept., University of Florida, November 26, 2002, Gainesville, FL.

Keith Lenghaus, Jeff Dale, David Henry, and James J. Hickman, "Characterization of Protein Interactions with MEMS Devices under Non-Static Conditions." Oral presentation at the 49th AVS, November 4-8, 2002.

Feng Wang, James J. Hickman, and R.A. Latour, "Experimental and Modeling Results for Protein Interactions with MEMS Devices." Poster at the 49th AVS, November 4-8, 2002.

David Henry, Keith Lenghaus, U. Jalgaonkar, Jeff Dale, J.C. Henderson, and James J. Hickman, "Protein Adsorption in Engineered MEMS Test-beds." Poster at the 49th AVS, November 4-8, 2002.

J.J. Hickman, "Integration of Cells and Silicon Devices via Surface Microengineering." AVS International Symposium, November 4-8, 2002, Denver, CO.

J.J. Hickman, "Integration of Cells and Silicon Devices via Surface Microengineering." University of South Carolina, October 21, 2002, Columbia, SC.

J.J. Hickman, "Integration of Cells and Proteins with Silicon Devices via Surface Microengineering." BioDevice Interface Science and Technology Workshop, September 9, 2002, Scottsdale, AZ.

Presentations given June 4th 2002 to Clare Thiem at project review:

David Henry, "Development of a Microfluids Test Bed." Project review meeting at Clemson, South Carolina, June 4, 2002.

Beata Sweryda-Krawiec, "Characterization of the Surface Adsorbed Proteins by XPS and a Standard Colorimetric Assay." Project review meeting at Clemson, South Carolina, June 4, 2002.

Keith Lenghaus, "Enzymes as Ultra-Sensitive Probes for Protein Adsorption in a Microfluidics System." Project review meeting at Clemson, South Carolina June 4, 2002.

Jeff Dale, "Enzyme Immobilization and Function on PEEK Capillaries." Project review meeting at Clemson, South Carolina June 4, 2002.

Caroline Henderson, "Preliminary Investigations of Serum and Serum Components in a Microfluidics System." Project review meeting at Clemson, South Carolina, June 4, 2002.

Halagowder Devaraj, "Concentration Determination of Adsorbed Proteins on Surfaces by Kinetic Silver Method." Project review meeting at Clemson, South Carolina, June 4, 2002.

Ken Marcus, "New Microanalytical Methods in Amino Acid and Protein Determinations." Project review meeting at Clemson, South Carolina, June 4, 2002.

Feng Wang, "Extracting Optimized Kinetic Parameters from Base-Line Model." Project review meeting at Clemson, South Carolina, June 4, 2002.

Aman Behal, "Modeling Residence Time for Protein Adsorption Under Flow." Project review meeting at Clemson, South Carolina, June 4, 2002.

Shankar Sundaram, "Computational Analysis of Protein-Surface Interactions in BioMEMS/Biomicrofluidic devices." Project review meeting at Clemson, South Carolina, June 4, 2002.

Society for Biomaterials annual meeting April 24 – 27, 2002 Posters:

B. Sweryda-Krawiec, G. Jacob, H. Deveraj, and J.J. Hickman,
"Langmuir adsorption isotherms for BSA on glass on XPS analysis."

K. Lenghaus, K. , J. Dale, E. Loghin, and J.J. Hickman, *Enzymes as Ultra-sensitive*
"Enzymes as ultra-sensitive probes for protein micro-adsorption."

Beata Sweryda-Krawiec, A presentation was made at the American Chemical Society meeting April 7 – 11, 2002.

Locascio, L. E., Perso, C. E., Lee, C. S., Chromatogr, *A* **857**, 275-84 (Oct 1, 1999). James J. Hickamn, Bioflips/Symbiosis meeting, February 20 – 22, 2002. Joint poster presentation by Clemson University and CFDRC.

Manuscripts in Preparation

K. Lenghaus, A. Behal, J. Jenkins, A. Bhattacharyya, D. Henry, K. Wilson, J. Dale, S. Sundaram, and J. J. Hickman, "Understanding the effect of flow on protein adsorption and apparent surface energetics." Manuscript in preparation for submission to *Science*.

K. Lenghaus, K. Wilson, J. Dale, D. Henry, A. Bhattacharyya, F. Wang, J. Jenkins, S. Sundaram, and J. J. Hickman, "Protein adsorption to polymers under static and flow conditions; early evidence for significant differences in the strength of protein/surface interactions in these two regime." Manuscript in preparation for submission to *Langmuir*.

J. Jenkins, B. Prabhakarpandian, K. Lenghaus, J. J. Hickman, and S. Sundaram, "Extraction of intrinsic kinetic constants from flow biosensors." Manuscript in preparation for *Biophys J*.

J. Evju, J. Feng, S. Krishnamoorthy, S. Sundaram, L.E. Locascio, A.C. Henry, D. Ross, M.J. Tarlov and J.J. Hickman, "Characterization of Electroosmotic Flow in Surface Modified Microchannels," Manuscript in preparation for submission to *Anal. Chem*.

J. Dale, K. Lenghaus, and J. J. Hickman, "Enzyme Immobilization and Function on PEEK Capillaries." Manuscript in preparation for submission to *Langmuir*.

D. Henry, K. Lenghaus, B. Sweryda-Krawiec, C. Henderson, and J. J. Hickman, "Development of a Microfluids Test Bed." Manuscript in preparation for submission to *Journal of Biosensors and Biotechnology*.

H. Devaraj, J. Dale, and J. J. Hickman, "Concentration Determination of Adsorbed Proteins on Surfaces by Kinetic Silver Method." Manuscript in preparation for submission to Analytical *Chemistry*.

C. Henderson, C.Chun, K. Lenghaus, M. Yacopucci, and J. J. Hickman, "Investigations of the Behaviour of Serum in a Microfluidics System", in preparation for submission to *J. Vac. Sci. Technol*.

Dissertations

Bhattacharyya, Arpita, "Use of Enzymes as Probes to Study Protein Adsorption in Static and Flow Conditions" Clemson University, August 2003.